2021

Development of Quantitative Intensity-Based Single-Molecule Assays

Benjamin Croop
University of Central Florida

DEVELOPMENT OF QUANTITATIVE INTENSITY-BASED SINGLE-MOLECULE ASSAYS

by

BENJAMIN CROOP
B.S. Materials Science & Engineering, University of Michigan, 2015
M.S. Materials Science Engineering, University of Washington, 2016
M.S. Optics and Photonics, University of Central Florida, 2018

A dissertation submitted in partial fulfillment of the requirements
for the degree of Doctor and Philosophy
in the College of Optics and Photonics
at the University of Central Florida
Orlando, Florida

Summer Term
2021

Major Professor: Kyu Young Han

ABSTRACT

Fluorescence microscopy has emerged as a popular and powerful tool within biology research, owing to its exceptional signal contrast, specificity, and the versatility of the various microscope designs. Fluorescence microscopy has been used to study samples across orders of magnitude in physical scale ranging from tissues to cells, down to single-molecules, and as such has led to breakthroughs and new knowledge in a wide variety of research areas. In particular, single-molecule techniques are somewhat unique in their ability to study biomolecules in their native state, which enables the visualization of short-lived interactions and rare events which can be highly relevant in clinical applications. For example, single-molecule real-time DNA sequencing has become a workhorse in genomics and personalized medicine. However, there have been few other analytical tools based on single-molecule fluorescence microscopy that have become popular in biomedical applications.

This dissertation describes work performed in an effort to transition single-molecule techniques from a research setting to a clinical setting. There were two main goals throughout: to develop quantitative single-molecule assays for data-rich analysis, and to make those assays more user-friendly to facilitate their adoption as standardized techniques. An initial study demonstrated the practicality of single-molecule analysis as a diagnostic tool by measuring differences in protein content between healthy patients and patients with Parkinson's disease.

From there, the assay was improved through various methods of beam shaping, which enabled more quantitative analysis of the detected biomolecules. A passivation scheme and sample preparation protocol were developed that reduce the time to perform a single-molecule assay by more than half while improving the assay sensitivity. Additionally, work performed to control the

fluorescent labeling of the target protein is described, with a goal of determining the stoichiometry of protein complexes, which is highly relevant to the pathology of Parkinson's disease and other neurodegenerative diseases. The report concludes with prospective projects that could extend the work completed thus far. An alternative labeling approach is outlined that may achieve one-to-one labeling between the proteins and fluorophores, as well as a project that shifts away from fluorescence microscopy and moves to a label-free scattering-based microscope design.

ACKNOWLEDGEMENTS

I would like to acknowledge my advisor Dr. Kyu Young Han for his invaluable insight and expertise in the area of fluorescence microscopy. Dr. Han's guidance and support were constant throughout my doctoral studies and particularly appreciated. I would also like to acknowledge the members of my committee, Dr. Dogariu, Dr. Kik, Dr. Kang, and former member Dr. Gelfand. Having such a knowledgeable committee to learn from has been an outstanding resource throughout my studies. Additionally, the help and support from all our group members was irreplaceable while conducting and troubleshooting experiments.

I would also like to acknowledge my girlfriend Haley Kerrigan, who has been exceptional throughout my time at CREOL. Haley was invaluable when I changed fields and first joined the department, and she helped flesh out many ideas during our conversations. Additionally, I would like to acknowledge my family for their unwavering love and support: my father Rob Croop, my mother Virginia Kreitler, and my sister Sarah Croop.

Finally, I would like to acknowledge the various funding agencies who have financially supported my work. This includes UCF through the ORC Doctoral Fellowship and the UCF Multidisciplinary Doctoral Fellowship. Additionally, I would also like to acknowledge the grant funding from the National Institute of Health, National Science Foundation, and Defense Advanced Research Projects Agency.

TABLE OF CONTENTS

LIST OF FIGURES

LIST OF ACRONYMS

α-SYN	Alpha-synuclein
A647	AlexaFluor 647
bPBS	Phosphate buffered saline with 0.1 mg/mL bovine serum albumin
BFP	Back focal plane
BME	Beta-mercaptoethanol
BSA	Bovine serum albumin
CD	Circular dichroism spectroscopy
COBRI	Coherent brightfield microscopy
DDS	Dichlorodimethylsilane
DoL	Degree of labeling
DSG	Disuccinimidyl glutarate
DT20	Dichlorodimethylsilane and Tween-20
dSTORM	Direct stochastic optical reconstruction microscopy
EGFP	Enhanced green fluorescent protein
ELISA	Enzyme-linked immunosorbent assay
EMCCD	Electron multiplying charge coupled device
FFI	Flat-field illumination
FOV	Field-of-view
HILO	Highly inclined and laminated optical sheet
HPLC	High performance liquid chromatography
iSCAMS	Interferometric scattering mass spectrometry

iSCAT	Interferometric scattering microscopy
LED	Light emitting diode
LCP	Left-handed circularly polarized light
MFD	Mode field diameter
MMF	Multi-mode fiber
NA	Numerical aperture
NB-A647	Nanobodies labeled with AlexaFluor 647
NHS	N-hydroxysuccinimide
PALM	Photoactivation localization microscopy
PBS	Phosphate buffered saline
PEG	Polyethylene glycol
RESOLFT	Reversible saturable optical linear fluorescence transitions
RHP	Right-handed circularly polarized light
rIgG	Reduced IgG antibodies
sCMOS	Scientific complementary metal oxide semiconductor
SDS-PAGE	Sodium dodecyl sulfate–polyacrylamide gel electrophoresis
SiMPull	Single-molecule pull-down assay
smFRET	Single-molecule Förster resonance energy transfer
STED	Stimulated emission depletion
STORM	Stochastic optical reconstruction microscopy
TIRF	Total internal reflection fluorescence
UV	Ultraviolet

CHAPTER 1: INTRODUCTION

The fields of optics and biology have been linked ever since the invention of the first optical microscopes by Antonie van Leeuwenhoek in the 17th century[1], which provided the first views of bacteria and led to significant advances in biology and medicine. The ability to visualize bacteria, cells, proteins, and other biomolecules has allowed researchers to more directly understand the complex mechanisms that define how these biological units interact with one another at the system level. Microscopy is somewhat unparalleled in its versatility as a research tool in that it allows samples to be analyzed at physical scales that span several orders of magnitude, and the insight from direct observation not only paves the way for new discoveries but can also clarify confounding results from other analytical methods. As such, advances in microscopes have directly contributed to advances in biological research, with modern cryo-electron microscopes allowing researchers to visualize biomolecules at nearly an atomic resolution. This enables researchers to visualize different structural states of biomolecules[2], and a key mantra within biology and microbiology is that structure determines function[3].

While cryo-electron microscopy offers the ultimate resolution for microbiologists, it is far from the most widely adopted technique to visualize and study biomolecules. This is due to many factors including the cost of a cryo-electron microscope, the complexity of the instrument and maintenance, and the somewhat complex sample preparation, among others. A technique must be straightforward and inexpensive to be widely adopted within the field of microbiology and used in a clinical setting outside a research lab. As such, fluorescence microscopy has emerged as one of the standards for the analysis of biological components for these same reasons. Building a

fluorescence microscope is straightforward, and the microscope can easily be modified to better suit the sample.

1.1. Common Fluorescence Microscope Configurations

The most common and simple configuration used in fluorescence microscopes is widefield or epi-fluorescence illumination[4], which will be referred to as epi illumination hereafter. Epi illumination is achieved by focusing the excitation light at the back focal plane (BFP) of the imaging objective, which results in a collimated beam that illuminates the entire sample volume at the imaging plane. This conveniently offers a large imaging area, but epi illumination can result in elevated background levels and thus lower signal contrast due to out-of-focus background fluorescence.

For thick or 3D samples such as cells and tissues it is critical to prevent out-of-focus background light from degrading the captured image. Selective excitation of a certain axial plane is often referred to as optical sectioning, and there are a wide variety of microscope configurations to achieve this. One of the most widely used methods is confocal microscopy where the excitation light is tightly focused and scanned over the sample, and the emitted fluorescence is focused through a pinhole to block the out-of-focus background[5, 6]. This idea is parallelized in spinning-disc confocal microscopy[7] where an array of focused beams, typically generated by a microlens array, is synchronously rotated with a pinhole array to achieve the same concept as traditional confocal microscopy while greatly improving the image acquisition time. Another configuration is to focus the excitation beam along one dimension, typically via a cylindrical lens, and use a slit rather than a pinhole to reject out of focus background. This is called line-scanning confocal

microscopy[8, 9], which further parallelizes and speeds up the image acquisition, but at the cost of a slight reduction in the optical sectioning capability[10].

An alternative approach to achieve optical sectioning is via inclined illumination or orthogonal excitation and detection pathways, which provide widefield illumination and thus faster imaging times and lower peak intensities. To achieve inclined illumination, the excitation beam is focused near the edge of the BFP of the microscope objective, which generates an angled, collimated beam that further refracts at the glass-water interface of a biological sample. This technique is referred to as highly inclined and laminated optical sheet (HILO) microscopy[11], but in this configuration the degree of optical sectioning is directly coupled with the beam thickness and thus field-of-view (FOV). To circumvent this limitation of HILO, highly inclined swept tile microscopy[12] was developed, which generates a thin but elongated beam via a cylindrical lens thus decoupling the FOV and beam thickness. The beam is then scanned synchronously with the rolling shutter of a scientific complementary metal oxide semiconductor (sCMOS) camera perpendicular to the thin axis of the beam. This yields optical sectioning with a full FOV where background rejection is provided by the rolling shutter of the sCMOS camera, which only records the portion of the FOV that is currently excited by the beam.

Orthogonal illumination and detection paths are typically used in light sheet microscopy, which allows the user to selectively excite the imaging plane without generating out of focus background and minimizing photobleaching[13, 14]. The most traditional method is to use a cylindrical lens to compress the beam along one dimension to form a sheet, but many variations are possible. Time-averaging a scanned beam to digitally form a light sheet is one approach[15, 16], but another is to use BFP engineering to create an array of beams which is referred to as lattice

light sheet microscopy[17]. This technique creates an array of light sheets by dithering, or rapidly scanning the beam back and forth, to create several time-averaged light sheets, which greatly reduces the peak intensity and photobleaching while maintaining a large FOV. Yet another light-sheet method is called field-synthesis[18], where a line-shaped beam formed by a cylindrical lens is scanned over a mask at the BFP or a mask conjugated to the BFP to form a time-averaged light sheet. Any light sheet can be formed by simply switching the mask, making this an especially powerful and simple technique. Light sheet microscopy has gained popularity as a research topic in recent years because its capability for widefield optical sectioning greatly improves the performance over other optical sectioning techniques such as confocal microscopy which require beam scanning; however, it has not seen wide adoption outside of specialized research applications. This is because light sheet microscopes are typically custom built to accommodate the orthogonal arrangement of the objectives and unique stages for mounting samples in this configuration. If high numerical aperture objectives are used to achieve improved optical sectioning or spatial resolution, then the short focal lengths can lead to physical constraints in the microscope design to prevent the objectives from colliding with one another. Additionally, light sheet microscopes are highly sensitive to misalignment, especially lattice- and c-light sheet configurations where only a small portion of the BFP is illuminated[19], which causes changes to the beam profile and thus optical sectioning characteristics.

For biological samples that are thin or where the user is only interested in features near the surface at the glass coverslip interface, total internal reflection fluorescent (TIRF) microscopy is a popular illumination scheme[20]. TIRF is achieved when the excitation light undergoes total internal reflection at the glass/water interface of the sample. The evanescent field from the totally internally

reflected light only penetrates roughly 50 – 250 nanometers into the sample from the coverslip surface, thus avoiding the generation of out of focus background fluorescence from deeper features in the sample. TIRF was originally achieved by placing a prism in contact with the glass slide or coverslip of the sample[21], although this required precise alignment of the prism with respect to the imaging objective. Currently, the most common method of achieving TIRF illumination is using modern high numerical aperture (NA) oil-immersion objective lenses. Objective TIRF was originally demonstrated via a mask that only transmitted light at the periphery of the BFP of the imaging objective[22], but modern approaches typically utilize objective TIRF illumination by tightly focusing the excitation light into the edge of the BFP of a high NA objective to achieve the large incidence angles requisite for total internal reflection[20]. The latter approach is often the most straightforward, but it can result in imaging artifacts that are most severe when imaging cells or tissues. Techniques for mitigating these artifacts are discussed in detail in the introduction of Chapter 4; however, single-spot objective-TIRF is well-suited to most 2D single-molecule studies. This is because any non-uniformity in the excitation is less noticeable due to the sparsity of the sample, or because the artifacts can often be avoided by slightly decreasing the angle of incidence of the excitation beam to create leaky or pseudo-TIRF if there is not a strong fluorescent background in the sample.

In summary, there exist a wide variety of fluorescence microscope configurations, each of which offer advantages for specific types of samples or studies. The most popular approaches tend to be those that involve a simplified experimental setup, so that they are easily adopted and free of tedious maintenance. Fluorescence microscopes have been widely used within microbiology due to the ease of building and adapting these microscopes combined with the exceptional signal

contrast provided by spectral filtering. Spectral filters provide excellent rejection of background light from the excitation beam, sample autofluorescence, as well as Raman or other effects. Another major benefit of fluorescence microscopy is the ease of achieving excellent specificity to a target of interest via immunolabeling with antibodies, labeling with complementary strands of DNA or RNA, or via simple click chemistry conjugation[23]. Multicolor labeling with spectrally well-separated fluorophores enables the visualization of multiple target structures by exploiting the combination of high specificity and spectral filtering via multiband filters or rotating filter wheels that are matched to the spectra of the fluorophores. This allows researchers to analyze the interactions between biological systems with outstanding clarity, which further exemplifies why fluorescence microscopy is such an invaluable tool for biological researchers.

1.2. Single-Molecule Techniques

The combination of sample specificity and exceptional signal contrast facilitated the first single-molecule studies[24, 25]. Single-molecule studies have several advantages over bulk or ensemble measurements, which begin with the sample preparation. Single-molecule studies often utilize more gentle sample treatments than ensemble studies where harsh detergents or chemicals are often used in common techniques, such as sodium dodecyl sulfate–polyacrylamide gel electrophoresis (SDS-PAGE)[26]. SDS-PAGE is a widely used technique to measure the molecular weight of a sample, but the sample preparation typically includes mixing with detergents, reducing agents, and boiling the samples to fully denature the biomolecules. Single-molecule studies that avoid such harsh treatments allow the biomolecules to be studied in their native state, and thus enable the visualization of rare binding events, conformational states, or other uncommon or short-

lived events that are averaged out by ensemble measurements[27]. Now many single-molecule techniques are available to probe the structure, kinetics or dynamics, expression levels, or other aspects of the sample. One of the most well-known aspects of fluorescent single-molecule microscopy is super-resolution microscopy, which gained widespread notoriety when the 2014 Nobel Prize in Chemistry was dedicated to the topic.

1.2.1. Super-Resolution Microscopy

Typical optical and fluorescence microscopes are diffraction-limited systems, and as such can only achieve a spatial resolution of roughly 200 nm. However, the three most well-known super-resolution techniques surpass this barrier via the principle of reversible saturable optical linear fluorescence transitions (RESOLFT)[28]. RESOLFT essentially refers to the switching of fluorophores on and off via a controlled or stochastic mechanism so that a densely labeled sample, such as 3D structures in a cellular sample, is imaged as a sparse single-molecule sample. The isolated emitters are localized to a high spatial resolution[29], switched off, and the process is repeated many times to build up the full image. These super-resolution techniques are often used to image large structures with very fine resolution but can be applied to gene expression and protein tracking as well. For example, a pioneering paper used super-resolution single particle tracking to monitor the motor protein myosin V and answered a longstanding question as to how this protein achieves its motion within along actin filaments[30].

Stimulated emission depletion microscopy (STED)[31, 32] is unique from other super-resolution techniques in that it is an all-optical technique. STED achieves the RESOLFT fluorophore switching process by co-raster scanning a typical confocal excitation beam that is

overlaid with a red-shifted donut-shaped beam. The red-shifted beam forces molecules at the periphery of the excitation beam to the ground state, so only molecules in the null at the center of the donut can fluoresce. These molecules are localized individually with high precision as the beams are scanned over the entire sample.

Photoactivation localization microscopy (PALM)[33] and stochastic optical reconstruction microscopy (STORM)[34] are two similar techniques that rely on photoactivation to achieve super-resolution. PALM involves using multiple beams to "activate" a region of the sample, where a small number of fluorophores are then excited, localized, and bleached. This process is repeated until the full image is acquired. STORM utilizes a pair of carefully chosen fluorophores that can be stochastically switched on and off via alternating beams of different wavelengths. This technique was simplified in direct STORM (dSTORM)[35], where the photophysics of a single fluorophore are carefully controlled via buffer conditions to tune the blinking rate of a single fluorophore to achieve the same concept with a single dye and laser.

1.2.2. Dynamics and Kinetics

Often it is the behavior of the biomolecule that is of more interest than its location, which is why single-molecule FRET (smFRET)[36] has become an especially popular tool. In smFRET two fluorescent labels, referred to as a donor and acceptor, are attached at two well-known labeling sites. A laser is used to excite the donor molecule, which will fluoresce if the acceptor molecule is not nearby. As the acceptor molecule moves closer to the donor molecule, the donor will more readily transfer excited electrons to the acceptor via intersystem crossing, causing the acceptor to fluoresce rather than the donor. The rate of electron transfer and acceptor fluorescence is strongly

dependent on the wavefunction overlap and thus distance between the donor and acceptor. This behavior enables smFRET to be used to monitor conformational changes of a single protein, such as the rate of folding and unfolding in response to environmental conditions[37], or to monitor intermolecular dynamics between two biomolecules, such as conformational changes in a complex[38].

The interactions or kinetics of a biomolecule can occur at sub-millisecond timescales, so it is often critical to surpass the detector-limited temporal resolution of widefield microscopy techniques. One technique is to use stroboscopic illumination, where the excitation source is modulated at a rate faster than the exposure time of the camera so short-lived interaction states are not time-averaged out by the detector[39]. Another technique is to spread temporal information across a physical dimension by splitting the detection path and inserting a galvo-mirror in one arm[40]. The unaffected detection arm is used for localizing molecules, and by stepping the galvo-mirror N times in a single frame of the detector, the temporal resolution is improved N-fold at the expense of a reduction in the observable FOV.

1.2.3. Protein Expression

In diagnostic research the protein expression level and stoichiometry can be extremely valuable information when diagnosing and understanding a disease. A traditional ensemble technique is the enzyme-linked immunosorbent assay (ELISA), but this technique can only provide the detection of and overall expression levels of proteins. The single-molecule pull-down (SiMPull)[41] assay is very similar to a sandwich ELISA assay in that it is an immunoprecipitation assay used to isolate a protein of interest from a total cell or tissue lysate and tether it to a substrate.

The main difference comes from the way the sample is then analyzed. In ELISA, the amount of protein is determined by a color change upon the addition of an enzyme and substrate molecule or a fluorescently tagged antibody, and the degree of color and thus protein level is measured by the optical density in a spectrophotometer. In SiMPull the signal is generated from a fluorescently tagged antibody, typically a secondary antibody, which is imaged in a fluorescence microscope. The concentration of the target protein can be determined from the density of the diffraction-limited single-molecule spots in the microscope images. However, the main advantage of SiMPull is that in addition to the concentration or expression level, it can also provide stoichiometric information about the protein of interest, which is typically inaccessible by an ELISA assay[42]. The stoichiometry can be determined via photobleaching steps, or by directly measuring the intensity of each fluorescent spot under controlled labeling conditions.

1.3. Motivation

While single-molecule fluorescence microscopy techniques can probe a wide variety of properties of biomolecules, there exists a gap between their use in research and clinical settings. Again, this is largely due to the complexity of a given technique or because the information a technique provides may be too qualitative enough for clinical analysis. As such, my work is centered on exactly this issue: developing techniques that are straightforward to implement that provide quantitative information about the biomolecule of interest. Specifically, my dissertation research focused on improving the SiMPull assay due to its similarities to the ELISA assay, which is already well-known and widely adopted outside of research institutions. Because the sample preparation for the SiMPull assay is similar to that of an ELISA assay it is not as daunting of a

method compared to more specialized and intensive techniques. Additionally, the SiMPull assay is extremely versatile in that it can easily be adapted to target different proteins simply by changing the primary antibodies used in the assay, which are readily available for purchase due to the extensive range of applications antibodies are used for within biomedical research. The familiarity of the technique, its flexibility, and ability to access new information about the target protein make the SiMPull assay a strong candidate for becoming a translational technique.

My research aims to bring the SiMPull assay to a point where it is used in a clinical setting for protein analysis by reducing the time required to perform these assays, while increasing the information gained from these assays. In the following chapters I will discuss my initial work validating the SiMPull assay on clinically relevant samples and showcasing that the assay can detect statistically relevant differences between patients with Parkinson's Disease and healthy controls. From there, I discuss improvements in illumination approaches, and how uniform illumination enables more quantitative intensity-based analysis. This is followed by my work on an improved glass passivation technique and fluorescent labeling method that greatly shorten the sample preparation time for SiMPull assays, making the technique more user-friendly. I then discuss work on making the fluorescent labeling more controlled, with a goal of achieving one-to-one labeling of proteins with fluorophores for intensity-based stoichiometry analysis. The final sections of this dissertation discuss potential future research can be done to further develop quantitative SiMPull assays, as well as a project to develop a label-free, quantitative single-molecule assay using scattered light.

CHAPTER 2: VALIDATING THE INTENSITY-BASED SINGLE-MOLECULE PULL-DOWN ASSAY

As mentioned previously, the SiMPull assay can probe the stoichiometry information of pulled-down protein complexes, which a traditional ELISA assay often cannot. Protein stoichiometry is often related to protein health, in that proteins and protein complexes require proper folding to assemble and function properly[43]. An example where protein misfolding and aggregation into oligomeric species is linked to disease pathogenesis is in alpha-synuclein (α-SYN) and its relation to Parkinson's Disease (PD).

A key identifier of a PD diagnosis is a buildup of α-SYN aggregates and fibrils in Lewy Body formations[44]. In PD patients, these Lewy Bodies are often selectively found on dopaminergenic neurons in the *substania nigra* region of the brain[45, 46]. However, while α-SYN aggregation is known to be linked to PD, no diagnostic test currently exists that allows the disease to be discerned from Alzheimer's Disease or other neurodegenerative diseases, which often present similar symptoms. Currently, patients must rely on a doctor's prognosis based on the patient's symptoms, which can only be confirmed via a brain biopsy *post-mortem*. Thus, if a test is developed that can distinguish aggregated α-SYN from the native configuration it may be possible to diagnose PD while patients are still living and more accurately deliver treatments among patients with neurodegenerative diseases.

The difficulties in diagnosing PD partially stem from conflicting results when studying α-SYN from recombinant protein[47-51], which may arise from differences in the protein folding and structure caused by the preparation or analysis protocols. This had led to debate over the native α-SYN stoichiometry, where the most agreed upon result is that α-SYN exists either as a monomeric

protein or a tetrameric complex. These contradictory results highlight that it is imperative to study the protein in its native state when studying protein stoichiometry, and to use endogenous protein samples whenever possible. This makes the SiMPull assay especially well-suited for the study of α-SYN. The SiMPull assay's similarity to the ELISA assay implies that it is likewise compatible with crude endogenous samples without the use of harsh chemicals or other treatments in the sample preparation; however, the ability of the SiMPull assay to provide stoichiometry information via the single-molecule intensities is a unique advantage over the bulk assay.

The most common way to use intensity information to assess stoichiometric information is by monitoring photobleaching steps. Photobleaching steps are abrupt and easily identified in a timetrace, where the intensity of a single-molecule spot is monitored for a long period of time (~60 seconds or more). Thus, in order to use this information, the target of interest must be labeled quantitatively, meaning a specified number of fluorophores per target molecule (ideally one-to-one labeling). This is straightforward with DNA or biomolecules genetically engineered to be covalently linked to fluorescent proteins[41, 52], but difficult for native proteins. Additionally, the requirement of observing a single FOV for a minute or more at a time to capture the photobleaching traces greatly limits the throughput of any method involving photobleaching.

A far more attractive approach is to directly measure the intensity of each diffraction-limited single-molecule spot. Using the fluorescence intensity rather than photobleaching steps greatly increases the imaging throughput, requiring milliseconds rather than roughly a minute per FOV. Again, to be a quantitative approach this requires one-to-one labeling; however, there are many applications where the exact stoichiometry is not required. For example, it may be possible to detect the difference between aggregated protein compared to an unaggregated protein or

complex without knowing the exact stoichiometry in either case. One would expect that the aggregated protein would be labeled with more fluorescent antibodies in a SiMPull assay and appear brighter than the healthy, unaggregated protein. This would be highly beneficial as a diagnostic tool where protein aggregation is linked with disease pathogenesis, as is the case with PD.

In this chapter I discuss initial efforts to validate the use of the SiMPull assay to detect α-SYN. I characterize the assay in terms of specificity and show that the SiMPull assay allows for intensity-based structural and stoichiometric analysis. I also show that the SiMPull assay is compatible with crude tissue lysates by comparing brain tissue samples taken from PD patients and healthy controls. This chapter outlines a proof-of-principle study on the applicability of the SiMPull assay as a clinical, diagnostic tool.

2.1. Methods

2.1.1. Preparation of SiMPull Assay Flow chambers

Slides and coverslips were passivated using methoxy PEG (mPEGSVA-5000, Laysan Bio) doped with 2.5% biotin-PEG (Biotin-PEG-SVA-5000, Laysan Bio) as described in previous SiMPull literature[53]. A passivated slide and coverslip were assembled to create five flow chambers using double-sided tape separating each chamber. First, the flow chambers were wet with 1x PBS pH 7.4, then incubated with 40 µL of 0.2 mg/mL NeutrAvidin (Thermo Fisher Scientific) diluted in PBS for 5 minutes and washed out with 100 µL of a wash buffer composed of 0.1 mg/mL bovine serum albumin (BSA; B9000S, New England BioLabs) diluted in PBS (bPBS). 5 µg/ml biotinylated anti-mouse IgG antibody (Abcam, ab97033) and 2.5 µg/ml mouse monoclonal α-SYN

antibody (BD Biosciences, 610786) were each incubated for 30 minutes, thoroughly washing with bPBS between each step. Then, 40 µL of cell lysates or protein samples incubated overnight with 1.3 µg/ml rabbit monoclonal α-SYN antibody (Epitomics, 2016-1) were diluted to the desired concentration and incubated for 30 minutes in the antibody-coated flow chambers. The flow chamber was thoroughly washed with bPBS before incubation with 0.7 µg/ml Alexa Fluor 647 (A647)-labeled anti-rabbit full IgG (Invitrogen, A31573) or F(*ab'*)$_2$ antibody fragment for 5 minutes. All antibodies were diluted using bPBS. 40 µL of bPBS was added instead of protein samples to measure the non-specific binding of A647-labeled antibodies, while all other steps were followed as described above.

2.1.2. Single-Molecule Imaging and Analysis

All imaging was performed using a custom-made objective-TIRF microscope. Prior to imaging, an imaging buffer containing 0.8% (w/v) dextrose (Sigma), 1 mg/mL glucose oxidase (Sigma), 0.04 mg/mL catalase (EMD Millipore) and 2 mg/mL Trolox (Santa Cruz) was added to the flow chamber to minimize photobleaching and blinking A647. 20 images were taken of unique FOVs, where the size of each FOV was ~4,700 µm^2. Custom MATLAB codes were used to count the number of single-molecule spots and extract their fluorescence intensity, similar to those used in previous studies[41]. To analyze the intensity of oligomeric or fibrillar α-SYN, the images were segmented using a threshold intensity value and the intensity of the segmented area was summed.

2.1.3. Preparation of Alexa 647-Labeled F(ab')$_2$ Antibodies

Donkey anti-rabbit F(*ab'*)$_2$ antibody fragment (Jackson ImmunoResearch; 711-006-152) was diluted in 100 mM sodium bicarbonate buffer (pH 8.3) and labeled with A647-NHS ester by

incubation at room temperature for 1 hour. Excess dye was removed by two rounds of filtration through NAP-5 purification columns (GE Healthcare), and the degree of labeling of the F(ab')$_2$ fragments was calculated using the absorbance measured with a NanoDrop spectrophotometer.

2.1.4. Preparation of α-SYN Recombinant Protein

α-SYN recombinant protein was generated by transforming BL21(DE3) *E. coli* strains with human α-SYN pT7-7 vector, where protein overexpression was induced with 1 mM IPTG for 24 hours. The cells were gently lysed using a lysis buffer (10 mM EDTA, 50 mM Tris pH 8.0, 150 mM NaCl). Then, the α-SYN protein was purified using a protocol published in past literature[54]. The purified monomeric α-SYN was dissolved in 1x PBS buffer supplemented with 0.05% sodium azide before aliquoting and storing at -80°C. To generate oligomeric or fibrillar α-SYN, the monomeric α-SYN was diluted to 3 mg/mL and shaken at 200 rpm at 37 °C for 5 days to induce aggregation and fibrilization.

2.1.5. Cell Culture and Generation of α-SYN Overexpressed or Knockout Cells

293T cells were grown in DMEM high glucose medium supplemented with 10% fetal bovine serum, penicillin (100 U/ml) and streptomycin (50 µg/ml) at 37°C in a humidified incubator with 5% CO_2. 293T cells were transfected with N-terminal flag-tagged full-length human α-SYN plasmid using the calcium phosphate transfection method to induce α-SYN overexpression. Cells were collected 36 hours after transfection for analysis via the α-SYN SiMPull assay and Western blotting. CRISPR/Cas9 genome editing was used to create α-SYN knockout cell lines. 293T cells were co-transfected with CRISPR/Cas9 plasmid with a cocktail of SNCA-specific single guide RNAs (sgRNAs) designed using Horizon's free CRISPR guide program (Horizon discovery Ltd.,

UK). Transfected cells were enriched by flow cytometry sorting using fluorescence from GFP produced by the backbone vector of the sgRNA. The sorted cells were genotyped and homozygous α-SYN knockout cells were cultured described as above and used for the α-SYN SiMPull assay. 293T cells transfected with N-terminal flag-tagged full-length human α-SYN plasmid were treated with 1 mM $FeCl_2$ (Sigma) for 48 hours to induce α-SYN oligomerization, and 5 μM MG132 proteasome inhibitor (Fisher Scientific) was added 6 hours prior to harvesting the cells.

2.1.6. In vivo Cross-Linking and Total Lysate Preparation From 293T Cells

To prepare total cell lysate without disuccinimidyl glutarate (DSG) treatment, cells were lysed in lysis buffer containing 25 mM Tris-Cl (pH 7.5), 150 mM NaCl, 1 mM EDTA, 1 mM EGTA, 1% NP40, 1% sodium deoxycholate, and 0.1% SDS supplemented with protease inhibitor cocktail (Sigma) on ice for 15 min. The lysate was centrifuged at 16,000 g for 15 minutes at 4°C, and the supernatant was collected for use in SiMPull assays. To perform *in vivo* cross-linking, cells were first collected in PBS and pelleted by centrifugation. The cell pellets were resuspended in PBS supplemented with 2 mM DSG (ProtemChem) and protease inhibitor cocktail (~5 volumes of the pellet) and incubated for 30 minutes at 37 °C with gentle shaking. The cross-linking reaction was quenched by the addition of 1 M Tris (pH 7.6) to a 50 mM final concentration and incubated for 15 minutes at room temperature. The cross-linked cells were lysed by three cycles of freeze-thaw to ensure that all protein populations were collected, regardless of their detergent solubility. The cell lysate was centrifuged at 1,000 x g for 10 minutes at 4°C and the supernatant was collected for analysis via the α-SYN SiMPull assay and Western blot.

2.1.7. In vivo DSG Cross-Linking and Total Lysate Preparation From Postmortem Human Brain Samples

Roughly 10 mg of *substantia nigra* tissue from freshly frozen control and PD postmortem brain samples were selectively punch biopsied, immediately transferred to 1.5 mL tubes containing 500 µL of PBS with protease inhibitor cocktail, and then centrifuged 1,500 x g for 5 minutes at room temperature. The tissue pellets were resuspended in PBS supplemented with 2 mM DSG and protease inhibitor cocktail (~5 volumes of the pellet) and incubated for 30 minutes at 37°C with shaking. The pellets were then centrifuged at 1,500 g for 5 minutes at room temperature, after which the supernatant was discarded and the pellets were again resuspended in PBS supplemented with protease inhibitor cocktail. The cross-linked tissue samples were lysed by three cycles of freeze-thaw and centrifuged at 1,000 x g for 10 minutes at 4°C. The supernatant was collected for the α-SYN SiMPull assay and Western blotting.

2.1.8. Analysis of α-SYN Oligomeric States

To generate a single-molecule sample representing a pure monomeric protein labeled with the A647-labeled F(ab')$_2$ antibody fragments, 1.3 ng/mL biotinylated rabbit monoclonal antibody (LSBio, LS-C370648) was added to a NeutrAvidin coated PEG surface in the flow chamber, washed out, 0.7 µg/mL anti-rabbit A647-F(ab')$_2$ was incubated, washed out, and imaging buffer was added. Here it was assumed that each fluorescent spot attributed to a single F(ab')$_2$ was the same as that of monomeric protein in the SiMPull assay, so its intensity profile was used to extract oligomer population using Equation 1:

$$I_{oligo} = I_S - (\alpha_S / \alpha_F) \times I_F \quad (1)$$

where I_S, I_F, I_{oligo} are intensity profiles of the sample, F(*ab'*)$_2$, and oligomeric protein, respectively, and α_S and α_F are the population value of the sample and F(*ab'*)$_2$ at the first peak.

2.1.9. Western Blot Analysis

Equal amounts of protein (0.5 µg of recombinant proteins, 30 µg of 293T cell lysate, and 20 µg of human postmortem brain samples) were electrophoresed on 10% SDS-polyacrylamide gels. The separated proteins were transferred onto a polyvinylidene fluoride membrane and blocked with 5% nonfat skim milk. Mouse monoclonal α-SYN antibody (BD Biosciences, 610786) was incubated at 4 °C overnight followed by anti-mouse horseradish peroxidase-conjugated secondary antibody (Jackson ImmunoResearch, 115-035-146) for chemiluminescent detection.

2.2. Results and Discussion

2.2.1. Initial α-SYN SiMPull Assay Characterization

To achieve specific isolation of α-SYN using the SiMPull assay, we used a four-antibody sandwich assay. The sandwich consisted of a biotinylated anti-mouse secondary antibody that was immobilized by the Neutravidin-coated passivated coverslip, a capturing primary monoclonal antibody derived from mice, a detecting primary monoclonal antibody derived from rabbits, and a A647-labeled anti-rabbit secondary antibody. A schematic of the assay as shown in Figure 1. It is critical that the capture and detecting primary antibodies target different epitopes to ensure proper immobilization and labeling of the protein of interest.

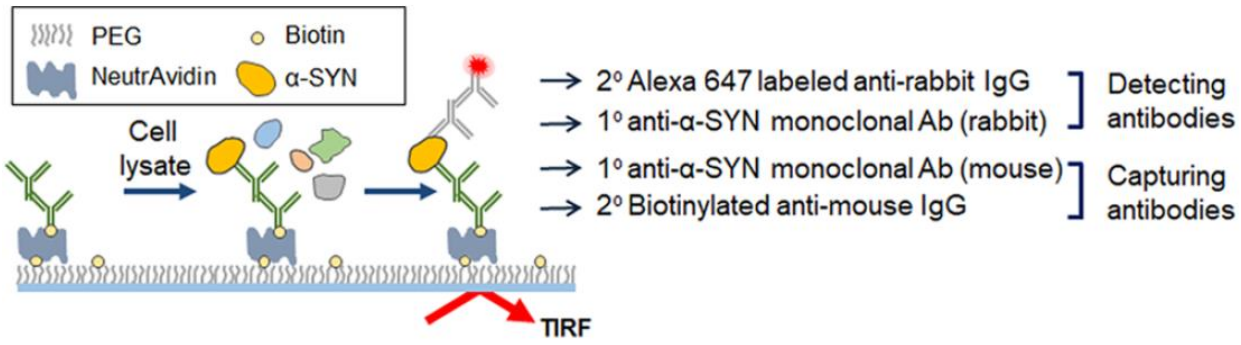

Figure 1. Experimental scheme used for the endogenous α-SYN SiMPull assay.

We were able to visualize human recombinant α-SYN protein when single-molecule imaging was performed using this antibody system, indicating that the binding affinity was sufficient for the SiMPull assay (Figure 2a). Next, we tested the specificity of the antibodies using total cell lysates, to see if the α-SYN protein could be isolated in a crude sample. For this experiment, we established α-SYN knockout 293T cell lines using the CRISPR/Cas9-based genome editing technique. Then, total lysates prepared from cells where no α-SYN was produced and cells that overexpressed α-SYN were each tested. The assay successfully detected high levels of α-SYN from the overexpressed α-SYN cell lysates with high specificity, while minimal fluorescent signal was observed using the cell lysates from the α-SYN knockout cell lines (Figure 2b,d). We also used the α-SYN SiMPull assay to measure endogenous α-SYN levels in crude lysates of wild-type 293T cells, where we observed that the number of single-molecule spots increased with the lysate concentration (Figure 2c,d). This collection of experiments demonstrated that the SiMPull assay selectively captured α-SYN from purified and crude samples from a variety of sources, while maintaining minimal background binding levels. These experiments also validated that the protein concentration could be calculated via the single-molecule spot density, essentially demonstrating all of the capabilities of an ELISA assay.

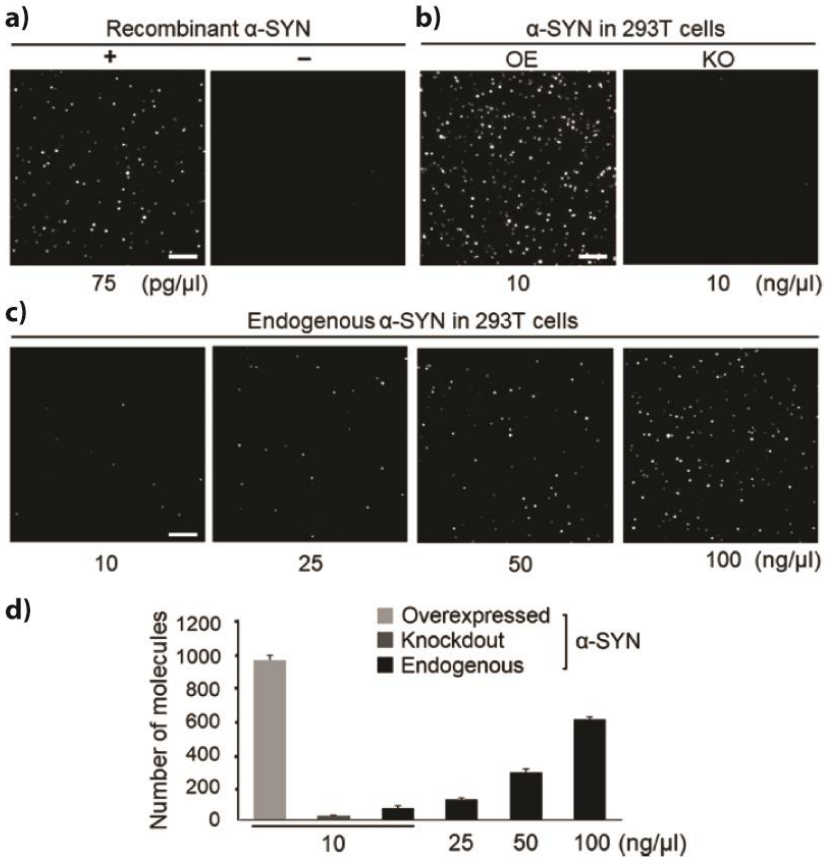

Figure 2. Establishing the α-SYN SiMPull assay. (a) Representative images of assays using recombinant human α-SYN protein (left) and nonspecific binding of Alexa 647-labeled anti-rabbit IgG (right). (b) Single-molecule images of α-SYN using crude 293T cell lysates from cell lines that overexpressed (OE) or knocked-out (KO) α-SYN. (c) Images of assays detecting endogenous α-SYN from 293T cells at various lysate concentrations. (d) Average number of α-SYN molecules detected per imaging area from >20 images, where error bars denote standard deviation (s.d.). Scale bar, 5 μm. All data are representative of three independent experiments.

2.2.2. SiMPull Assay Analysis of Oligomeric Recombinant α-SYN Protein

α-SYN oligomerization is strongly linked to neuronal toxicity[55, 56]. As such, accurate analysis of α-SYN oligomerization states is highly beneficial for diagnosing and monitoring the progression of PD. To reduce potential steric hinderance effects while labeling α-SYN oligomers, we utilized A647-labeled F(ab')$_2$ antibody fragments instead of full IgG antibodies. Additionally, we labeled the F(ab')$_2$ at a degree of labeling of ~2.9 to achieve a relatively narrow fluorescence intensity distribution while minimizing the amount of unlabeled fragments. Then, the SiMPull

assay was used to measure oligomeric human α-SYN that was prepared by incubating recombinant monomeric α-SYN at 37°C for 5 days to induce fibrilization[54] (Figure 3a−e). The number of α-SYN molecules in the pulled-down complexes was analyzed via the fluorescence intensity of the immobilized protein complexes, which is proportional to the number of proteins labeled by the detection antibodies in the assay. As expected, a number of large, bright spots were observed in the oligomeric/fibrillar α-SYN sample, which resulted in an intensity distribution that extended to higher intensity values. Meanwhile, the monomeric α-SYN sample yielded a more narrow distribution composed of lower intensity molecules (Figure 3d,e). Of note, we observed elongated fluorescent features in the oligomeric/fibrillar α-SYN sample that were substantially larger than the diffraction limited spots detected in single-molecule experiments (Figure 3b,c). This indicates that by imaging individual protein complexes, the α-SYN SiMPull assay can provide structural or morphometric information about the sample. This is a unique capability compared to the bulk ELISA assay, which is only suited for detection and concentration analysis due to its reliance on a color change for signal detection. Monomeric and oligomeric α-SYN species in the respective samples were confirmed using conventional Western blot with a significantly larger sample volume than what was used in the SiMPull assay.

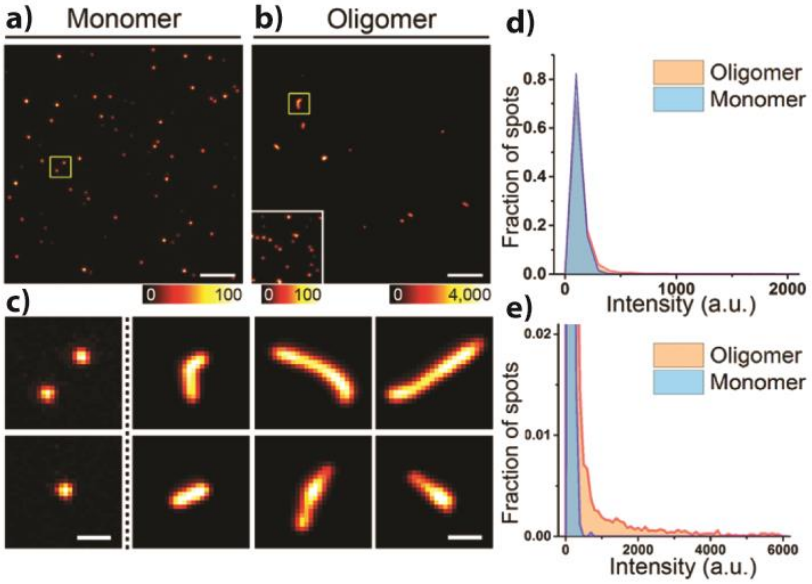

Figure 3. Oligomeric α-SYN analysis using the SiMPull assay. Images from SiMPull assays performed using monomeric (a) and oligomeric (b) recombinant α-SYN. Monomers in the oligomeric α-SYN sample are displayed in the inset of (b) after intensity adjustment. (c) A comparison between monomeric (left-most column) and oligomeric/fibrillar α-SYN (rightmost three columns). (d,e) Fluorescence intensity profiles from monomeric (blue) and oligomeric (red) recombinant α-SYN samples. Scale bar, 5 μm (a,b) and 1 μm (c). All data are representative of three independent experiments.

2.2.3. Analysis of α-SYN in Cultured Cells via the α-SYN SiMPull Assay

After confirming that the assay can immobilize oligomeric protein complexes, we assessed if the relative amounts of monomeric and oligomeric protein could be extracted from the assay results. SiMPull assays were performed using total cell lysates from 293T cells overexpressing α-SYN with or without exposure to $FeCl_2$ and a proteasome inhibitor, MG132, which are known to cause aggregation of α-SYN[57-59]. Before lysing the cells, *in vivo* protein crosslinking was performed using DSG to maintain the native state and stoichiometry of the protein complexes[60]. α-SYN SiMPull assays performed on lysates from the $FeCl_2$ and MG132 treated cells resulted in intensity distributions with a larger fraction of single-molecule spots that fluoresced at higher intensities in compared to the nontreated control lysates (Figure 4a). To extract the relative

populations of monomeric and oligomeric α-SYN, A647-labeled F(*ab'*)$_2$ molecules were immobilized in a flow chamber and imaged to generate an intensity distribution. It was assumed that monomeric proteins detected in the SiMPull assay would have the same fluorescence intensity as the individual F(*ab'*)$_2$ molecules, so the F(*ab'*)$_2$ intensity distribution as used to decompose the intensity distributions from the treated and untreated cell lysates into monomeric and oligomeric populations. The results in Figure 4b and 4c show that oligomeric α-SYN was more prevalent in the $FeCl_2$ and MG132 treated cell lysates (37%) than the nontreated cells (15%), which was confirmed with Western blot analysis. However, all of the α-SYN detected from the $FeCl_2$ and MG132 treated cells appeared as diffraction-limited spots, rather than the elongated shapes observed in the fibrillar recombinant α-SYN samples.

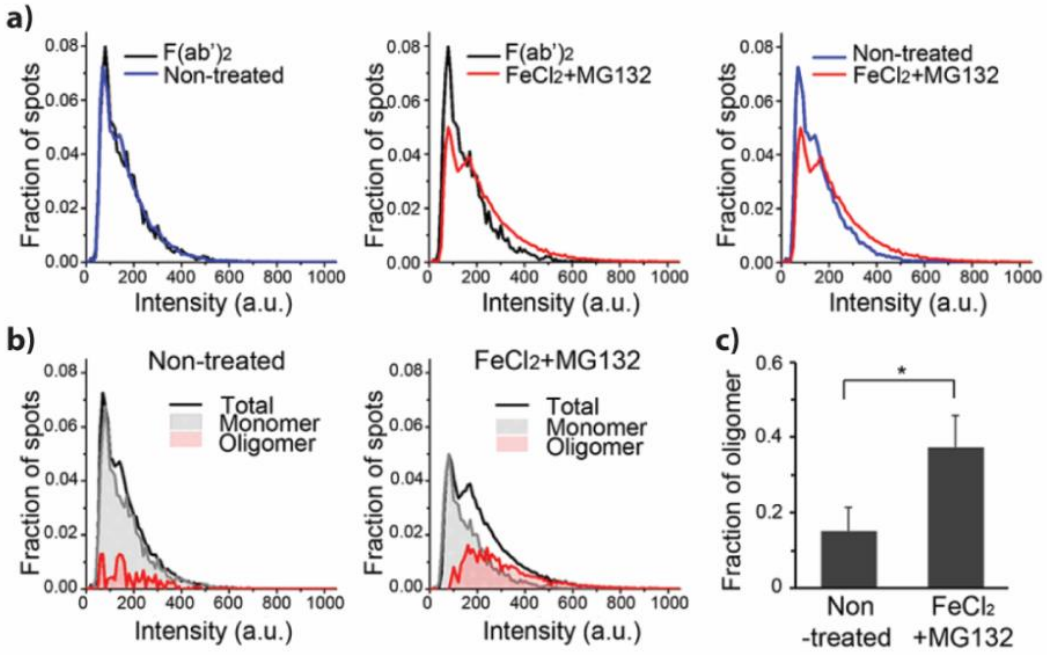

Figure 4. SiMPull analysis of oligomeric states of α-SYN from *in vivo* DSG crosslinked total cell lysates. (a) Intensity distributions from cells overexpressing α-SYN with (red) or without (blue) $FeCl_2$ and MG132 treatment. (b) Decomposition of the oligomeric fractions in each sample, where monomeric and oligomeric proteins were plotted in grey and red, respectively. (c) Measured fraction of oligomeric protein from the data plotted in b). Error bars denote standard error of the mean (n = 3). *P < 0.05, by unpaired two-tailed test. 10 ng/μL of total lysates from *in vivo* DSG-crosslinked 293T cells were used in each assay. All data are representative of three independent experiments.

2.2.4. Analysis of α-SYN in Human Brain Tissue by α-SYN SiMPull Assay.

Lastly, we used the α-SYN SiMPull assay in a clinical diagnostic application to test if we could detect differences in the α-SYN content from *postmortem* human brain samples. The *substantia nigra* was punch-biopsied (~10 mg) to target dopaminergic neurons from frozen control or PD postmortem brain samples and minimize contributions from other non-desired cells. The biopsied tissue was treated with DSG for *in vivo* crosslinking before the soluble protein was collected (Figure 5a). The PD sample yielded a 3.3-fold increase in the overall amount of detected α-SYN compared to the control samples (Figure 5b), but more significantly also had an elevated amount of oligomeric α-SYN. We measured that 56% of the detected α-SYN from the PD brain tissue was oligomeric, whereas the control brain tissue contained only 23% oligomeric α-SYN (Figure 5c−e). Again, fibrillar α-SYN was not detected in any of the brain samples, and Western blot analysis confirmed significant amounts of oligomeric α-SYN in the PD samples (data not shown).

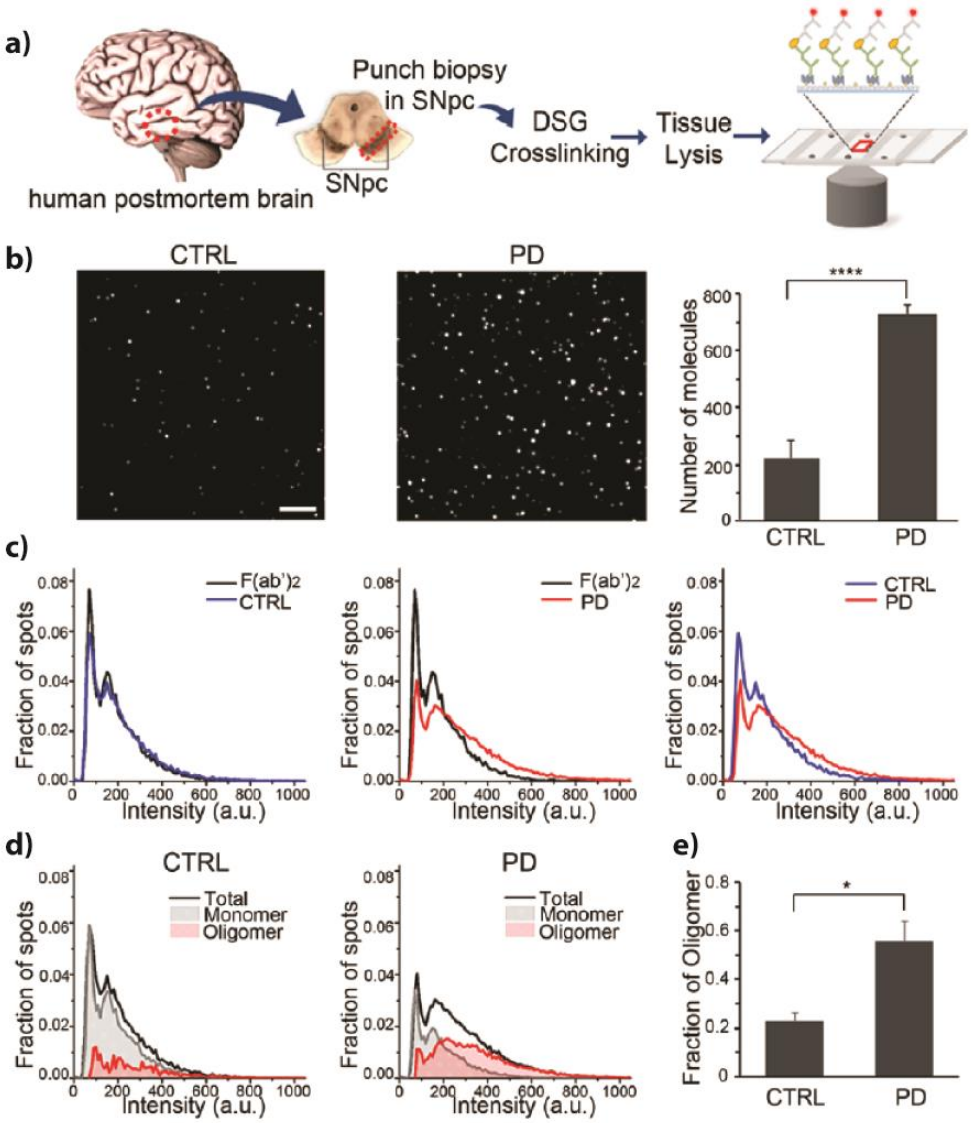

Figure 5. SiMPull analysis of α-SYN oligomeric states in postmortem human brain samples. (a) Schematic diagram of the experimental procedure. (b) SiMPull images of α-SYN from control (CTRL, left) or PD brain samples (middle), and the average number of molecules per FOV (right) taken from 20 images. Scale bar, 5 μm. (c) Intensity distributions from CTRL (blue) and PD (red) brain samples plotted with the F(ab')$_2$ intensity distribution as a monomeric reference (black). (d) Decomposition of the relative amounts of monomeric (gray) and oligomeric (red) α-SYN in the CNTRL and PD brain tissue. (e) Comparison of the oligomeric populations extracted from the data presented in d). Error bars denote standard deviation in b) and standard error of the mean (n = 3) in e). *P < 0.05, ****P <0.0001 by unpaired two-tailed t test. All data are representative of three independent experiments.

2.3. Conclusion

This chapter has shown that the SiMPull assay is well-suited to studying purified or endogenous proteins in their native state. Additionally, the fact that a SiMPull assay requires a much smaller amount of sample than traditional ensemble measurements allows for the sample to be taken from a targeted region of interest from the human brain, which is fairly unique to single-molecule techniques. The smaller amount of required sample and gentle treatment of the extracted sample provided clear results, which separates this method from ensemble measurements that have yielded conflicting results due to the differences in sample processing methods and caused disagreement amongst researchers in the field. As such, SiMPull clearly showed elevated amounts of overall α-SYN and oligomeric α-SYN in PD patients compared to healthy controls. The oligomerization information of α-SYN was probed directly via the intensity of the single-molecule spots rather than photobleaching steps or other time-consuming methods. Structural information was obtained from the oligomeric recombinant α-SYN sample studied using the SiMPull assay, where fibrils were observed. In short, the study presented in this chapter shows that the SiMPull assay has promise to be a particularly attractive technique within diagnostic research, because the analysis is high-throughput and the data is information-rich. The following chapters will discuss improvements to the assay to make the information more quantitative, and a method to make the assay more user-friendly.

CHAPTER 3: UNIFORM ILLUMINATION VIA REFRACTIVE BEAM SHAPING

The previous chapter showed that the intensity information of single-molecule spots can provide clinically relevant information regarding the oligomerization states of biomolecules. However, that initial study was only able to provide qualitative information regarding the oligomerization state, namely a comparison between monomeric and non-monomeric species. While useful, the ability to quantitatively analyze biomolecules via the fluorescence intensity is much more desirable. One limitation in the previous study was the use of an expanded and clipped Gaussian excitation beam, which yields a non-uniform beam profile. The intensity of single-molecule spots is highly dependent on the excitation beam profile, and as such a non-uniform excitation source will result in non-uniform fluorescence across the FOV. If the intensity of each single-molecule is meant to be used to extract quantitative information, it is critical that the excitation source is uniform so that the generated fluorescence is also uniform and not spatially dependent. Beyond the specific application of determining the stoichiometry of protein complexes, non-uniform excitation has been problematic in a number of areas of fluorescence microscopy.

One example where spatially dependent fluorescence is particularly problematic in super-resolution imaging[34, 61-63], where the localization accuracy and resulting resolution of the reconstructed image is determined by the number of emitted photons and thus depends on the excitation intensity[64-66]. Another example where non-uniform illumination is an issue is in high-throughput imaging where an extremely large FOV is desired that maintains high spatial resolution. To achieve this, a grid of images is captured and then aligned with one another using post-processing to assemble the full image. However, if the excitation beam is non-uniform over

the FOV the stitched image will display a "windowpane" effect, where a darkened border will surround each individual FOV used to construct the larger composite image[67]. A number of computational approaches exist that can attempt to correct inhomogeneous illumination[67, 68]; however, they can be incompatible with low-light imaging techniques such as single-molecule imaging or introduce artifacts caused by uncontrollable intensity fluctuations.

Instead, it is often more appealing to generate uniform illumination rather than attempt to correct it in post-processing. The most common approach is to greatly expand a Gaussian beam and clip it down to the centermost portion where the intensity is relatively flat[69], as was used in the previous chapter. However, this method is not ideal due to the severe loss of excitation power and slight nonuniformity at the periphery of the beam. A couple of other common approaches include using a pair of microlens arrays[65, 70] or a multimode fiber and speckle reducer[71, 72], but these approaches are not compatible with objective-TIRF illumination because they reduce the spatial coherence of the beam. The loss of spatial coherence makes it impossible to tightly focus to the periphery of the BFP of the objective without also generating unwanted epi illumination. As such, refractive beam shaping[73] is highly desirable approach because there is no loss of power or spatial coherence, making it well-suited for a variety of fluorescence microscopy techniques including TIRF illumination. However, refractive beam shaping has been difficult to implement due to the need for the lenses to have exceptionally high surface quality to maintain the uniform beam profile over the long working distance (~300 mm) required to reach the objective of a commercial microscopy body while preserving the spatial coherence of the light source[74].

In the following chapter I will present work implementing a refractive beam shaping device to achieve a uniform, "flat-top" or "flat-field" excitation beam. This technique enables the number

of fluorophores to be determined directly from the intensity of the single-molecule spot, while preserving the ability to achieve objective TIRF with a standard fluorescence microscope body.

3.1. Methods

3.1.1. Flat-Field Illumination Fluorescence Microscope Setup

Our imaging system was built around an Olympus IX73 inverted microscope body as shown in Figure 6. Two laser sources (06-MLD 638 nm and 06-DPL 561 nm, Cobolt) were used, which were split into two fiber couplers and delivered to the microscope so the flat-field illumination (FFI) could be compared with Gaussian illumination. One beam was delivered from a single-mode fiber (P5-630PM-FC-2, Thorlabs) and collimated with an achromatic lens (L1, f = 63.5 mm, #49-780, Edmund Optics). This beam was sent to the beam shaper (TopShape, asphericon GmbH) where the input size was ~10 mm ($1/e^2$), but sizes between 9.2 mm and 10.8 mm were generally acceptable[75]. We found this fiber and collimating lens resulted in the most uniform beam profile, but fibers with other mode field diameters (MFD) and lenses with other focal lengths can be used. Two mirrors (M1 and M2) were used to steer the beam to the TopShape and adjust the beam profile for maximum uniformity. The beam profile was monitored via a live feed in MicroManager[76] while adjusting the direction of the beam entering the TopShape. The flat-top beam was then aligned into the microscope body using two mirrors (M3 and M4) and was focused to the BFP of the imaging objective (UPlanSApo, 100x/1.40 oil, Olympus) by a TIR lens (L3, f = 300 mm, AC508-300-A, Thorlabs). The TIR lens was mounted on a xyz translator to adjust the incidence angle for epi or TIRF illumination, as in conventional TIRF imaging.

To create Gaussian beam profiles, the other portion of the split output from the light sources was delivered to a second excitation arm via another single-mode fiber (P5-630A-PCAPC-1, Thorlabs) which was collimated with a lens (L2, f = 80 mm or 150 mm, Thorlabs). This Gaussian beam was directed to the excitation path and sent to the microscope via a flipping mirror that was installed between the TopShape output and TIR lens. Fluorescence was collected through a multi-band filter cube (laser quad-band TRF89901v2, Chroma) and imaged onto an electron-multiplying charge-coupled device (EMCCD) camera (iXon Ultra 897, Andor).

3.1.2. Beam Profile Measurement

A thin layer of dye was made by placing 2 μL of a ~1 μM dye soltution (STAR635 or Cy3B from Abberior or GE Healthcare, respectively) onto a microscope slide, and covering it with a square 22 × 22 mm^2 coverslip. A pipette tip was used to spread the dye and ensure full coverage of the entire coverslip area before sealing with epoxy. For best results, the glass should be cleaned using a potassium hydroxide treatment, as described in the PEG passivation protocol[36].

Beam profiles were recorded by exciting the dye lyaer with a 638 nm or 561 nm laser with the Gaussian or FFI beam, and ImageJ[77] was used to measure the intensity profile along the diagonal of the FOV. The irregularity of the FFI was calculated as the standard deviation divided by the mean of the intensity within the FW90M of the profile. The illumination efficiency (η) of the FFI was determined by inserting a 0.5x demagnification system before the camera, which prevented clipping of the beam at the sensor chip. The intensity of FFI and the Gaussian beams detected by the camera without the 0.5x demagnifier was divided by the total intensity of the beam to calculate the efficiency. The efficiency for Gaussian beams was calculated using similar

principles, but Gaussian beams were simulated using parameters taken from experimental data instead of using the demagnification system to ensure the full intensity in the dim periphery of the beams was included.

3.1.3. Optical Simulation

The experimental setup was modelled in CodeV (Synopsys). The source was fiber-coupled, so the divergence of the beam emanating from the fiber depends on the MFD of the fiber. The MFD decreases with the wavelength of the coupled light, thus changing the beam divergence and diameter. As such, the MFD and the divergence angle were calculated for each wavelength used in the simulations. The fiber output was simulated as a point source with the calculated divergence and was collimated by a lens. The focal length of the collimation lens was determined by the divergence of the beam and was adjusted to achieve a collimated beam with a diameter of approximately 10 mm at $1/e^2$, as required for the beam shaping device. The collimated beam was delivered through the beam shaping system and the resulting flat-top beam profile was calculated at various distances after the beam shaping system, which was considered to be the working distance. For some simulations, an additional beam expander was inserted after the beam shaping device to magnify the output beam by a factor of 1.5, which increased the maximum working distance over which the flat-top profile is maintained by nearly a factor of two. The intensity profiles were calculated using the illumination analysis tool (LUM) in CodeV. LUM was used to compute the simulated FFI illuminance (or irradiance) distribution across a receiver surface, and Monte Carlo ray tracing was used to model the transfer of radiation from extended sources to the receiver surface, to simulate the beam profile at large working distances.

3.1.4. Dye-Labeled DNA Samples

For single-molecule experiments using single-stranded DNA, an 18-nucleotide sequence conjugated with biotin and A647 at either end was used and will be referred to as oligo 1. For dual-probe experiments, two short sequences of DNA (called probes) labeled with A647 and complementary capture oligomers conjugated with biotin were diluted in hybridization buffer (200 mM NaCl and 10 mM Tris, pH 8) to a concentration of 2 μM of each probe and 1 μM of capture oligo, heated at 95°C for two minutes, then slowly cooled down to room temperature to hybridize or bind the probe DNA to the capture oligomers. For single probe experiments, the same procedure was followed but only one probe was hybridized with the capture oligo. For multi-color experiments, we used probe 1 labeled with either Cy3B or A647. The labeled DNA was stored in T50 buffer (10 mM Tris pH 8 and 50 mM NaCl). All chemicals and oligonucleotides were purchased from Sigma-Aldrich and IDT unless specified otherwise.

3.1.5. Single-Molecule Fluorescence Imaging and Analysis

We used biotin-labeled BSA or PEG (Laysan Bio) to passivate the flow chambers as described previously[40]. Flow chambers were first wet with T50 buffer, then 20 μg/mL Neutravidin diluted in T50 was added and incubated for 5 minutes before washing out with T50. Roughly 10 pM of biotinylated DNA labeled with A647 was incubated for 5 minutes in the flow chamber and washed out. An imaging buffer composed of 2 mM Trolox (Santa Cruz) and an oxygen scavenger (20 mM Tris pH 8.0, 250 mM NaCl, 1% w/v dextrose, 1 mg/mL glucose oxidase, 0.04 mg/mL catalase) was added before imaging the samples to minimize photobleaching and blinking. For all single-molecule experiments an excitation power of 4 mW was used for both Gaussian

illumination and FFI, except in the case of the photobleaching experiment where the laser power was increased to expedite photobleaching. We obtained images from 20 different areas for single-molecule analysis.

Custom MATLAB codes were used to localize each fluorescent spot and extract the intensity data[40]. The x-coordinates and intensities of molecules in the centermost 50% of the FOV were stored to generate 1D single-molecule intensity profiles using FFI and Gaussian illumination, and the intensity of each molecule was plotted as a function of the x-coordinate of the molecule with 160 nm precision limited by the pixel size of the detector. When multiple molecules were localized to the same x-coordinate, the intensity of all the molecules at that pixel were averaged and plotted as a single data point.

An additional MATLAB script was used to generate thresholding curves in addition to the code for the above intensity distributions. The thresholding parameter was normalized to the highest intensity single molecule in each FOV, such that the threshold was a fractional value multiplied by the intensity of that molecule. The number of molecules were plotted at each threshold value, where x-axis was the fractional value used to normalize the threshold parameter. The error bars represent the standard deviation from the average number of molecules at each thresholding value. When the threshold is set too low, the spot-finding code incorrectly counts noise as spots, and when it is set too high the code does not count the true single molecule spots and only counts extremely bright spots which are typically impurities or multiple emitters.

For photobleaching analysis, the oligo 1 DNA sequence was imaged using an excitation power of 9 mW using both Gaussian illumination and FFI. 120 second movies were recorded in 10 FOVs, where the first 10 frames of the movies were used to localize all the single-molecules,

and the photobleaching time for all molecules in the movie was measured. The photobleaching data was combined from all the movies, where the illuminated area was divided into six concentric rings, each with a width of 50 pixels, and the average photobleaching time of each ring was calculated. The resulting average photobleaching time was plotted as a colormap.

3.1.6. Background Reduction by Flat-Field TIRF Illumination

To test if it was possible to generate TIRF illumination with FFI we imaged oligo 1 in the presence of 5 nM antibodies labeled with A647 in PEG-passivated flow chambers. For comparison, we used a bare multimode fiber (MMF, Ø = 105 μm, NA 0.15, Draka Prysmian fiber) attached to a shaking motor (JRF370-18260, ASLONG) that homogenized the MMF output beam. We calculated signal-to-background ratio as:

$$SBR = (I_S - I_B)/I_B \quad (2)$$

where I_S and I_B are the mean of signal and background intensity. 50 single-molecules in the centermost portion of the FOV were used for the signal-to-background analysis.

3.1.7. Preparation of Cell Samples

A549 cells (ATCC) were grown on coverslips in a Petri dish with F-12K medium supplemented with 10% fetal bovine serum (F2442, Sigma) and 1% Penicillin/Streptomycin (15140122, Thermo Fisher), incubated in 5% CO_2 at 37°C for 48 to 72 hours. U2OS cells (ATCC) were cultured in McCoy's 5A medium and plated on an 8-well Lab-Tek chamber to demonstrate TIRF cellular imaging. The mitochondria was stained by removing the cell medium and adding pre-warmed staining solution containing 50-100 nM MitoTracker Red CMXRos (M7512, Thermo Fisher). The stain was incubated in the CO_2 incubator for 30 min, and was then washed three times with the

culture medium before fixing the cells using 3.7% paraformaldehyde (15710, Electron Microscope Sciences) at room temperature for 15 min. The cells were washed with 1x PBS three times and permeabilized with 0.1% (v/v) Triton X-100 for 5 min. To minimize nonspecific binding of the actin stain, the cells were washed with PBS and preincubated with PBS containing 1% BSA for 30 min. Then, actin was stained with A647 phalloidin (A22287, Thermo Fisher) for 20 min. The A549 sample was mounted in Prolong Diamond antifade mountant (P36961, Thermo Fisher) and sealed with epoxy, and the U2OS sample was mounted in imaging buffer so the refractive index was appropriate for achieving TIRF illumination.

3.1.8. High-Throughput Imaging

A motorized 2D stage (SCAN IM 120 x 80, Marzhauser) controlled by MicroManager was used to acquire a 3 × 3 grid of images using 638 nm and 561 nm excitation lasers. The FFI beam was magnified 1.5x by a beam expander (asphericon GmbH) mounted on the end of TopShape to ensure the entire FOV was illuminated for stitched imaging. We imaged the same area with a Gaussian beam collimated by the 150 mm focal length lens as a comparison. The grid of images were aligned and stitched into the full reconstructed image separately for the red and green color channels using the stitching plugin of Fiji software[78]. A small amount of the mitochondria signal leaked into the actin image, which was corrected after image stitching.

3.2. Results

3.2.1. Flat-Field Illumination

We characterized the uniformity of the FFI by imaging a thin dye layer excited with epi-illumination. FFI was generated by sending a roughly 10 mm diameter Gaussian beam (λ = 638 nm) to the TopShape beam shaping component (Figure 6b), which yielded an output beam diameter of 81.5 μm (taken as the full-width at 90% of maximum) at the imaging plane, which was well-matched to the size of our observable FOV (82 × 82 μm^2). The recorded beam profiles are presented in Figures 6c and 6d. For comparison, we recorded beam profiles from Gaussian illumination generated by an 80 mm or 150 mm focal length collimating lens, and their full-width at 90% of maximum was 15.0 μm or 28.6 μm, respectively. FFI exhibited 2.9% intensity variation which was determined by calculating the root-mean-square of the intensity within the full-width at 90% of maximum region. This level of non-uniformity has been demonstrated to not affect single-molecule imaging or the spatial resolution in super-resolution fluorescence microscopy[65]. The illumination efficiency of Gaussian beams was 92.9% and 51.4% for 80 mm and 150 mm focal length lenses, whereas FFI had an efficiency of 85%. Thus, FFI achieved a comparable efficiency to that of the f = 80 mm Gaussian beam but with greatly improved beam uniformity. The TopShape component was compatible with multicolor imaging and produced FFI at wavelengths of 561 nm and 638 nm without changing the fiber or collimating lens (Figure 6e), where both wavelengths achieved a uniform beam profile for working distances up to 300 mm (Figs. 6f and 6g). We observed that the temporal coherence length of light sources did not affect the illumination profile based on comparisons between HeNe and diode lasers (data not shown here).

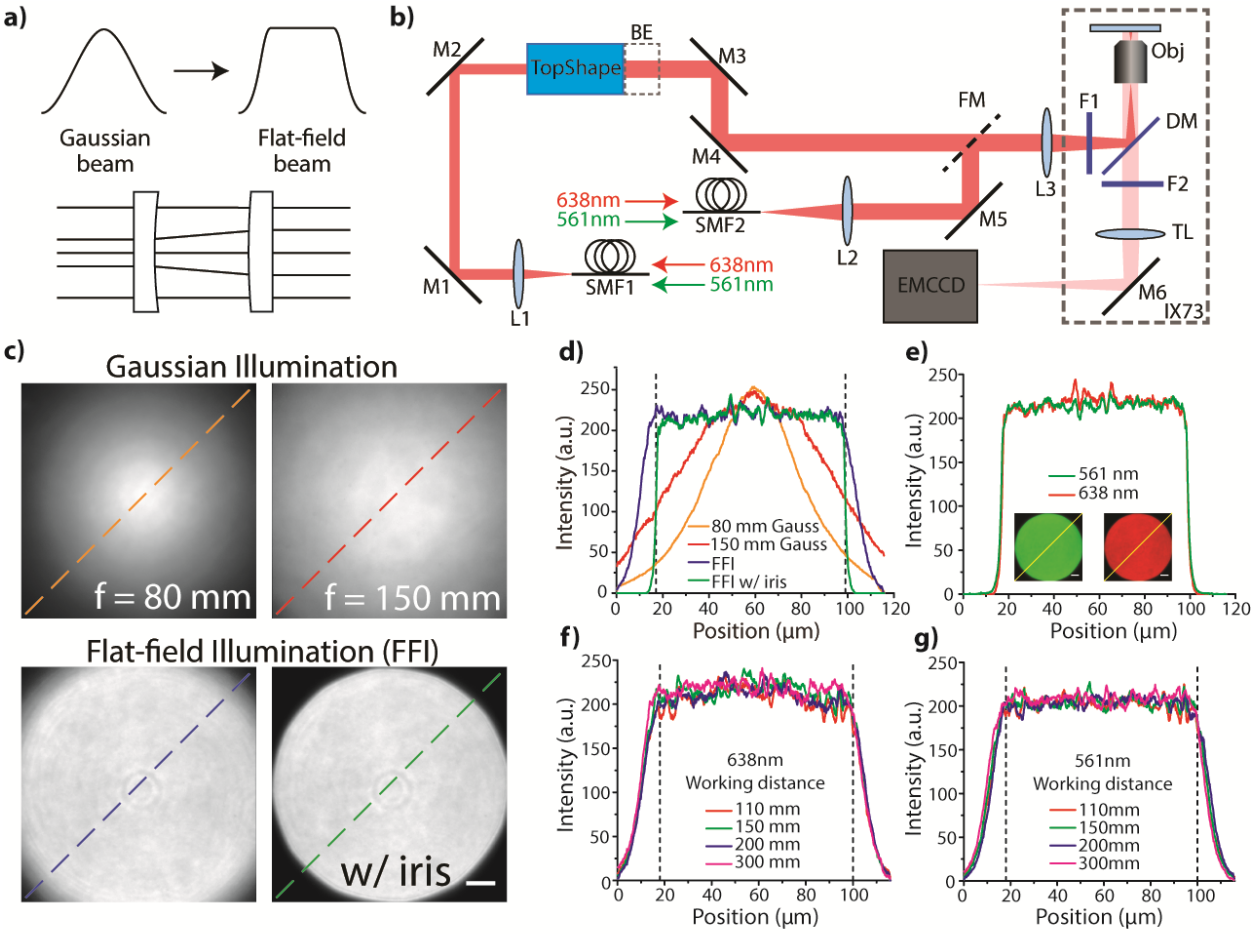

Figure 6. Characterizing FFI. (a) Schematic of aspheric beam shaping. (b) Experimental setup. BE, 1.5x beam expander; DM, dichroic mirror; F1-2, excitation/emission filters; FM, flip mirror; L1-3, lenses; M1-6, mirrors; Obj, objective; SMF1-2, single mode fibers; TL, tube lens. (c) Beam profiles of Gaussian beams collimated by an 80 mm or 150 mm focal length lens (top) and FFI beams without and with an iris (bottom). (d) Lineouts taken from the beam profiles in c) along dashed lines. Vertical dashed lines in d) indicate the 82 μm camera FOV. (e) Lineouts taken from multicolor FFI beam profile images (inserts) with an iris. Working distance dependence of FFI using 638 nm (f) and 561 nm illumination (g). Scalebars, 10 μm.

3.2.2. Simulated Beam Intensity Distribution

The FFI beam profile simulations were able to be performed using geometric optics methods because the TopShape component uses refractive beam shaping, which causes a smooth redistribution of the beam intensity[75]. The beam profile was simulated at a specified working distance after the TopShape, and Figure 7a shows the normalized intensity distributions using 640

nm illumination at various working distances. A mostly uniform flat-top beam profile was observed; however, the intensity distribution becomes slightly inhomogeneous at a working distance of 600 mm because the beam-shaping system used was designed for shorter distances.

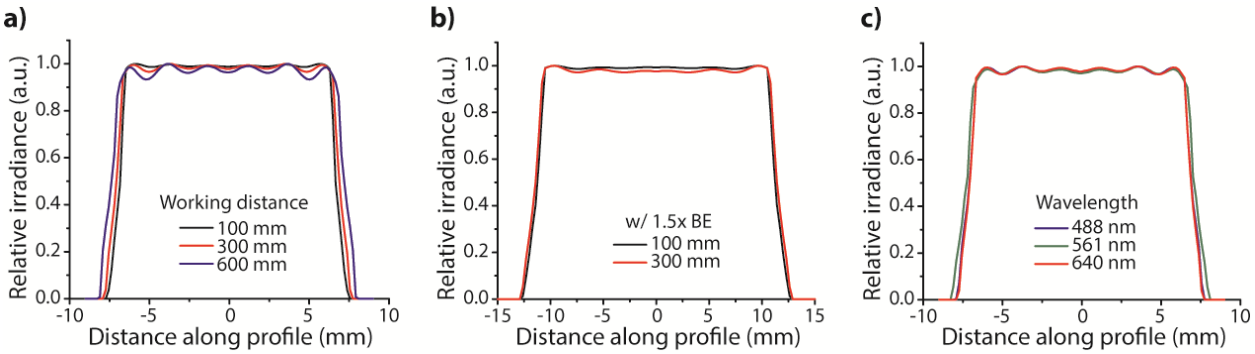

Figure 7. Simulated flat-top beam profiles. Working distance dependence for an illumination wavelength of 640 nm without (a) and with (b) an additional beam expander (BE). (c) Beam profile dependence on the excitation wavelength at a working distance of 300 mm.

Beam shaping is performed by manipulating the phase front of the incident laser beam to achieve the desired output intensity distribution over a certain range. However, larger differences in the relative phase develop beyond the designed working distance, which results in increased nonuniformity in the beam profiles. The length of the uniform region is determined by the design of the beam shaping device, and the current beam shaping system is limited to working distances of roughly 300 mm to maintain a plateau homogeneity of more than 95%. The use of a beam expander after the beam shaping component extends the working distance range over which a uniform flat-top beam profile can be maintained, as shown in Figure 7b where the beam profiles are more homogenous than in Figure 7a. Another simulation was carried out to assess the wavelength dependence of the beam shaping system at a fixed working distance (300 mm), but as shown in Figure 7c, there was nearly no difference in performance between three different laser wavelengths spanning the visible spectrum (488, 561, and 640 nm).

3.2.3. Single-Molecule Imaging and Intensity-Based Analysis

Single-molecule imaging using objective TIRF illumination was conducted to evaluate the impact of uniform excitation in a low-light fluorescence microscopy application. When DNA labeled with A647 was excited using Gaussian illumination, the molecules closest to the center of the beam exhibited more intense fluorescence than those near the periphery, while under FFI the molecules fluoresced much more uniformly across the full FOV (Figure 8a). The 1D single-molecule intensity trace in Figure 8b clearly visualizes this effect.

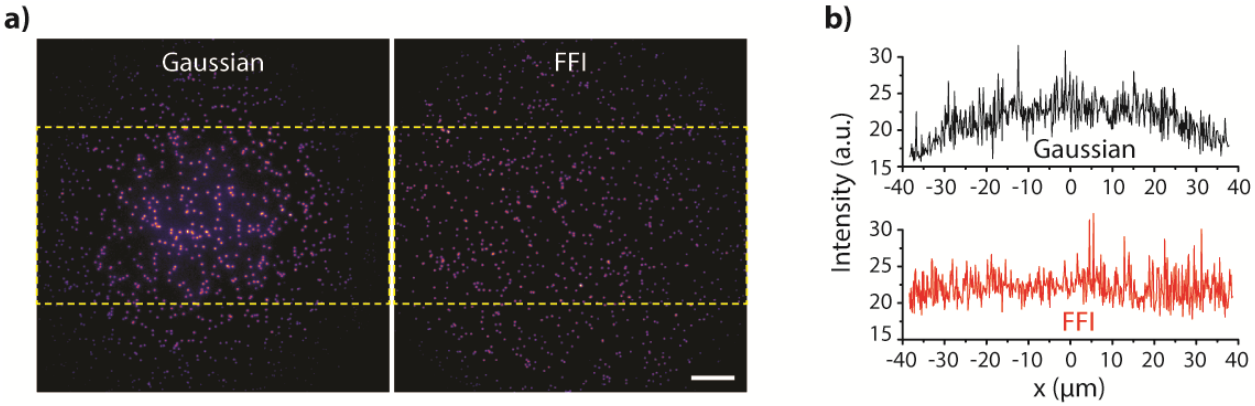

Figure 8. Single-molecule imaging using FFI. (a) Representative images taken using Gaussian illumination (left) and FFI (right). Scale bar, 10 μm. (b) 1D intensity distribution generated from molecules in the yellow boxed region of a).

This uniform fluorescence signal is highly beneficial and provides multiple improvements to single-molecule intensity analysis. Firstly, it makes single-molecule spot-finding algorithms less sensitive to the thresholding value, which is used to determine if the signal-to-background ratio of a spot is suitable to be included for analysis, and generally a global threshold is used[41]. To demonstrate this effect, the number of single-molecule spots was determined and plotted as a function of the normalized threshold value for both Gaussian illumination and FFI. Figure 9a shows that as the threshold parameter is increased the number of detected spots continuously decreases when imaged under Gaussian illumination, whereas the FFI curve exhibited a well-

defined plateau where the number of detected molecules is insensitive to the thresholding parameter and an accurate spot count be determined.

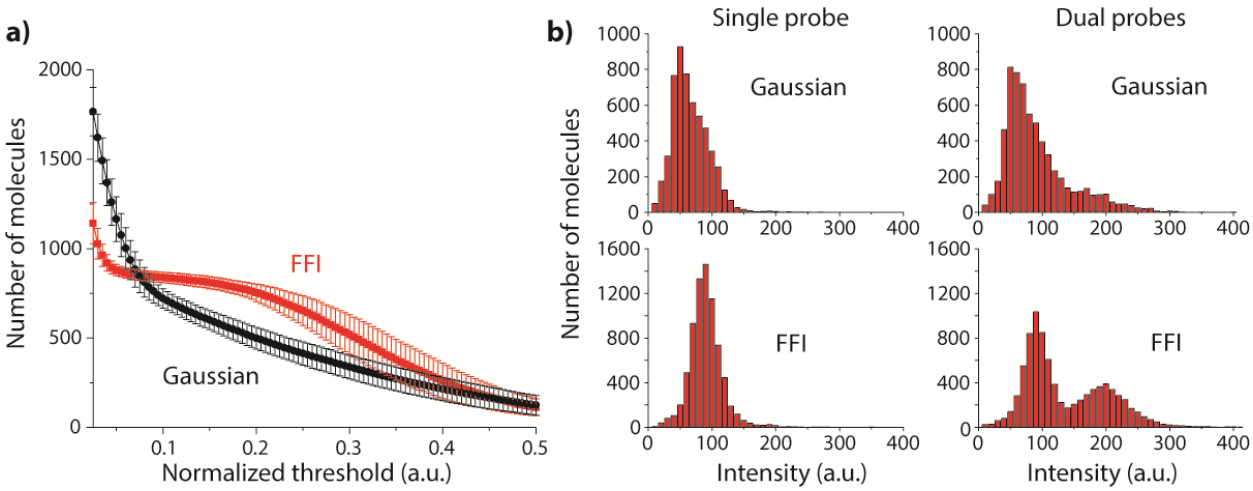

Figure 9. Improved single-molecule analysis with FFI. (a) Threshold curve plotting the dependence on the number of detected molecules to the thresholding parameter used for spot-finding. Error bars represent the standard deviation from the mean. (b) Intensity distributions from DNA samples with one or two complementary fluorescent probes imaged using Gaussian illumination and FFI. Images taken from 20 different regions were used for each analysis.

Secondly, FFI improves single-molecule intensity-based analysis due to the dependence of fluorescence intensity on the excitation intensity. To test if FFI allowed us to distinguish the fluorescence intensity of individual fluorophores, we prepared single-probe and dual-probe DNA samples. The single probe DNA sample had exactly one fluorophore per DNA stand, whereas the hybridization process for the dual probe sample yielded a mixture where the capture oligo bound either one or two fluorescent probes. The intensity distributions of the single and dual probe samples imaged under FFI and Gaussian illumination are presented in Figure 9b. Gaussian illumination resulted in intensity distributions that were a nonuniform shape, where the distribution from the dual probe sample exhibited a large shoulder compared to the single probe distribution. By contrast, the FFI intensity distribution from the single probe sample is a single, narrow peak that is readily fit to a Gaussian curve, and the intensity distribution from the dual probe sample

clearly demonstrates the applicability of FFI for quantitative intensity-based analysis. The FFI dual probe distribution exhibits two well-resolved peaks, where the central intensity of the second population is twice that of the single probe distribution, indicating that the use of FFI enables intensity differences from single fluorophore molecules to be discerned. By fitting the FFI dual probe distribution with Gaussian peaks, it was possible to determine the amount of oligomers labeled with one or two probes, which were 73% and 27% respectively. It was straightforward to achieve similar multi-color single-molecule imaging results (Figure 10).

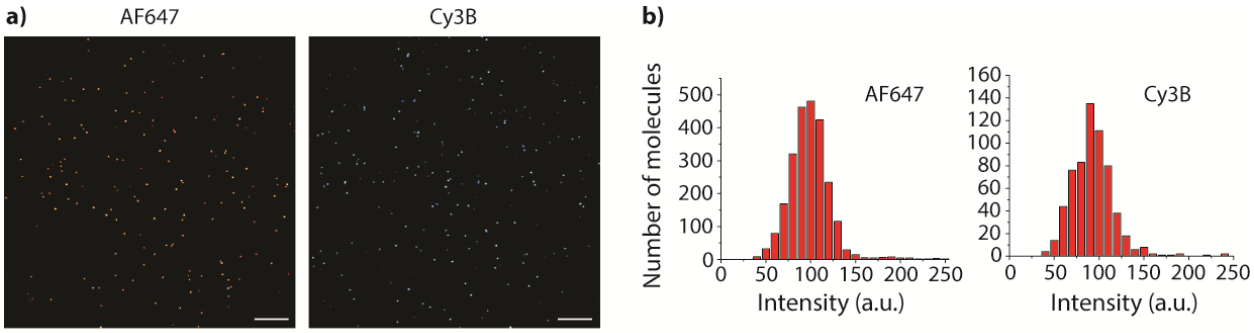

Figure 10. Dual color imaging using FFI. Single-molecule image (a) and intensity distributions (b) of single probe DNA samples labeled with A647 or Cy3B dye. A647 was imaged under 4 mW of 638 nm laser excitation, while Cy3B was imaged using 3 mW of 561 nm excitation. Scale bar, 10 μm.

Thirdly, we measured the spatial dependence of the photobleaching time under Gaussian illumination and FFI (Figure 11). It was observed that the average photobleaching time closely followed the characteristics of the beam profile, where FFI exhibited uniform photobleaching across the full FOV and Gaussian illumination caused single-molecules near the center of the FOV to photobleach at a rate more than twice that of those than near the periphery.

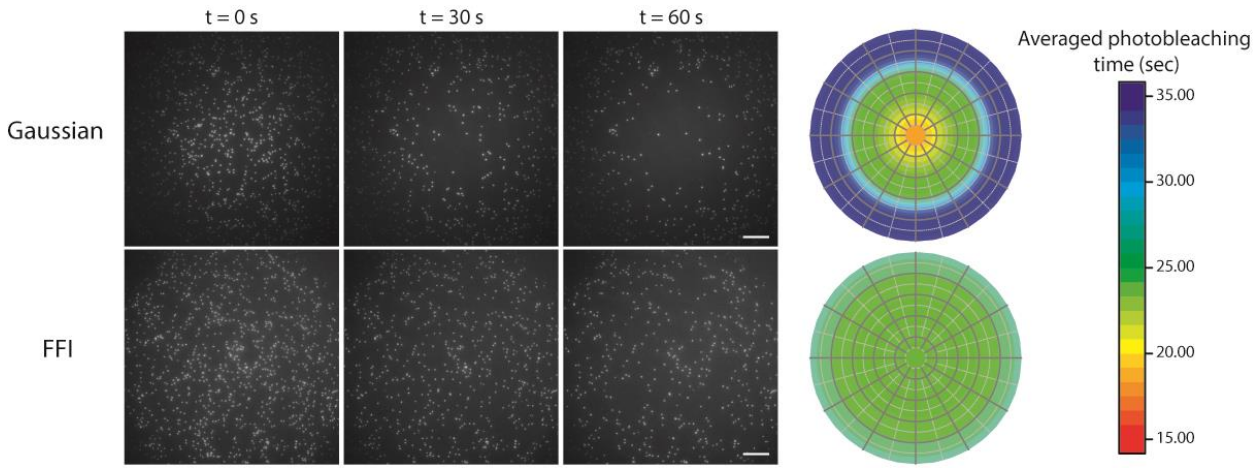

Figure 11. Photobleaching analysis. Representative single-molecule images taken during photobleaching experiments using Gaussian illumination and FFI. Colormap showing the azimuthally-averaged photobleaching time analyzed with images taken from 10 different FOVs. Scale bars, 10 μm.

3.2.4. Background Suppression via TIRF Illumination

Next, we performed single-molecule imaging of DNA in the presence of 5 nM fluorescently labeled molecules as fluorescent background to assess if FFI was compatible with TIRF illumination and able to achieve adequate background rejection. As a comparison, we used a MMF combined with a speckle scrambler to generate a uniform, incoherent beam profile. The FFI from the TopShape component fully suppressed the background fluorescence, as seen in Figure 12; however, the illumination from the MMF only partially suppressed the background. For our TIRF microscope, the incident beam needed to be focused within the outermost 120 BFP μm of the BFP of the objective for all the incident light to contribute to the generation of an evanescent field, however the limited spatial coherence of the MMF prevented tight focusing and resulted in an elevated background level from the leaky TIRF illumination. The measured signal-to-background ratio was 12.5 ± 7.8 and 5.1 ± 4.1 (mean ± S.D.; n = 50) for FFI and the MMF, respectively.

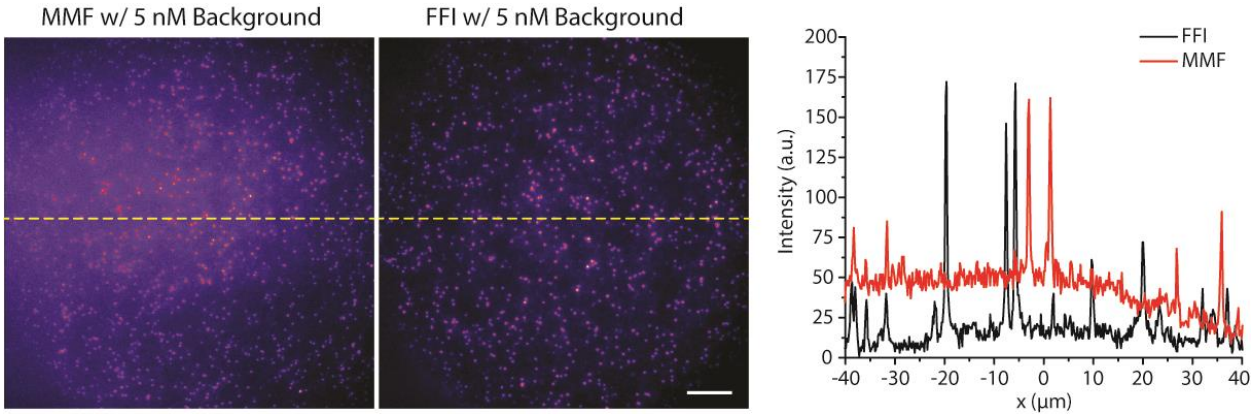

Figure 12. Background suppression via TIRF illumination. Representative images acquired using illumination from an MMF combined with a speckle scrambler and under FFI in the presence of 5 nM background. Lineouts taken as indicated by the dashed yellow lines. Scale bar, 10 μm.

3.2.5. High-Throughput Stitched Imaging

Finally, we explored the utility of FFI in high-throughput imaging by acquiring a grid of images from a fluorescently labeled cell sample. We installed a 1.5x beam expander that mounted directly onto the output of the TopShape (Figure 6b) to fully cover our camera, which we observed to cause no degradation to the uniformity the illumination profile. We imaged the cells in TIRF and epi illumination using excitation wavelengths of 561 and 638 nm.

Figure 13a shows a comparison between stitched 3×3 images of the cells imaged in epi using Gaussian illumination (left) and FFI (right). It is clear that the uniformity of FFI enabled clean stitching of the images even with a small image overlap of 5%, whereas the stitched image acquired using Gaussian illumination shows distinct dark borders around each individual FOV where the excitation beam is dim. A small image overlap greatly increases the size of the imaged area, especially when larger grids of images are acquired, thus increasing the imaging speed and minimizing photobleaching in high-throughput imaging. We also demonstrated the compatibility

of FFI with a low magnification (20x) objective (Figure 13b), which is highly beneficial for monitoring large regions of cell colonies. Figure 13c shows a 5×4 stitched image comparison between TIRF and epi excitation using FFI and Gaussian illumination. For both TIRF and epi, FFI enabled uniform imaging while Gaussian illumination resulted in windowpane artifacts due to the non-uniform excitation profile. TIRF illumination suppressed fluorescence from the cytoplasm and resulted in exceptional contrast of surface features, such as actin focal adhesions, which are especially visible in the FFI image due to the overall image uniformity.

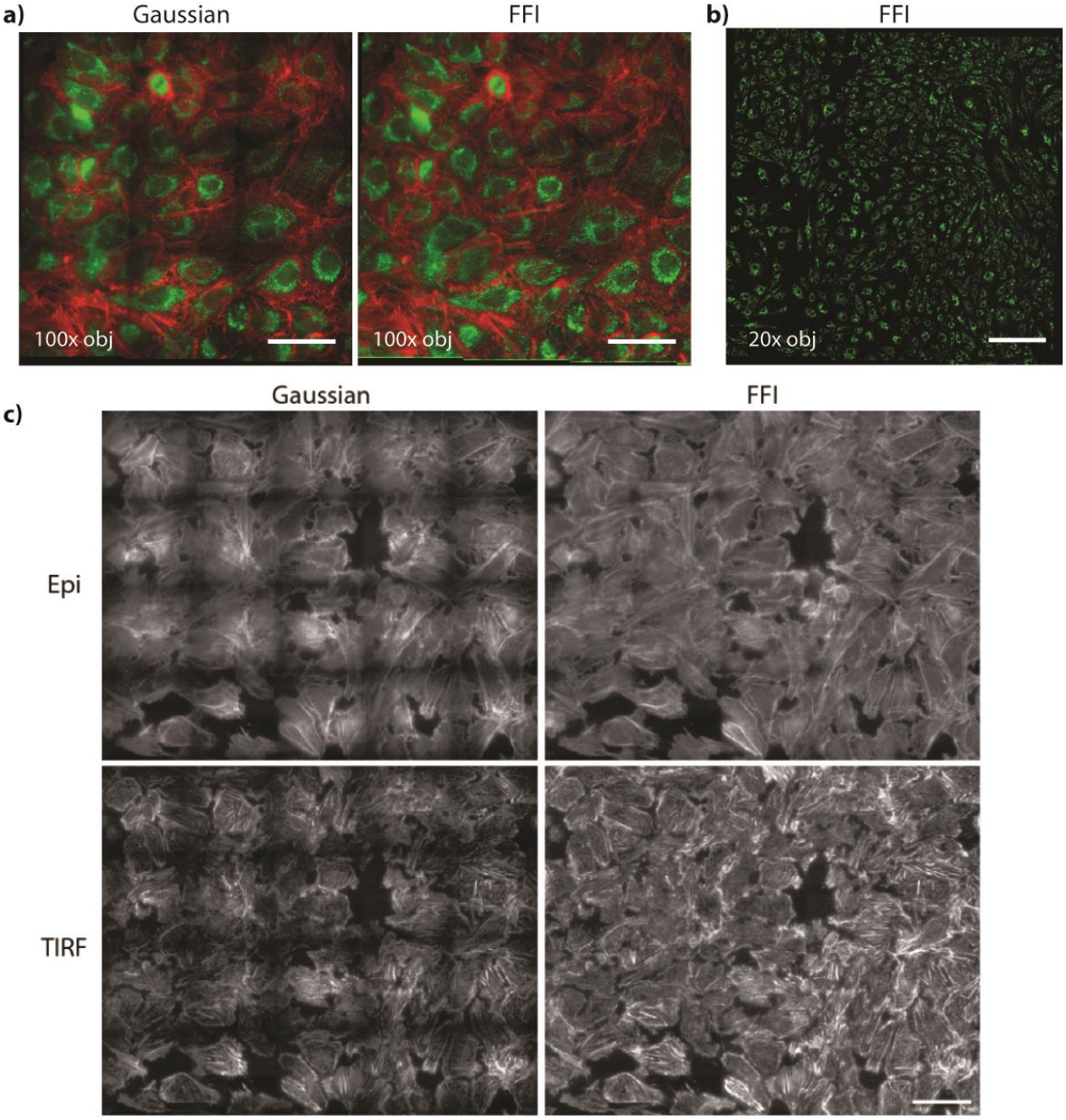

Figure 13. Seamless image stitching using FFI. (a) 3×3 multicolor imaging of A549 cells with stained mitochondria (green) and actin (red) imaged using Gaussian illumination with 150 mm focal length lens (left) and FFI with a 1.5x beam expander (right). (b) 3x3 stitched image of mitochondria aquired using FFI and a 20x objective. (c) Stitched epi and TIRF images of actin stained U2OS cells acquired under Gaussian illumination with an 80 mm focal length lens and FFI without the 1.5x beam expander. Image overlap, 5% (a), 10% (b,c). Scale bars, 50 μm (a,c), 200 μm (b).

3.3. Conclusion

In summation, this chapter has shown that refractive beam shaping is an effective method of generating uniform excitation which we referred to as FFI. FFI yielded many benefits relating to thresholding and counting, photobleaching, and stitched imaging of large FOVs with high spatial resolution. Uniform stitched imaging can be very beneficial for monitoring large areas of cultured cell growth, which is useful in monitoring drug response[79], tissue engineering, and gene expression[80], among others. However, the most important takeaway from this chapter in regard to the context of this thesis is that the use of FFI within single-molecule imaging allowed us to discern the difference in intensity from a individual fluorophores and extract the relative size of each population in a mixed sample. This is a key result in our goal of using quantitative intensity analysis in single-molecule imaging for accessing stoichiometry information about proteins or other biomolecules. This shows that so long as the sample is labeled in a quantitative manner, it is possible to discern the stoichiometry of single-molecule complexes based on the fluorescent intensity alone.

CHAPTER 4: UNIFORM ILLUMINATION VIA ANNULAR FIBER BUNDLE

The previous chapter demonstrated the numerous benefits of uniform illumination in fluorescence microscopy applications, and that uniform excitation generates uniform fluorescence signal from the sample. However, one aspect that was ignored is that conventional, objective-based TIRF illumination can cause artifacts in the captured images. The two most common artifacts are shadows which are caused by the unidirectional light scattering off an object in the sample, and interferences fringes caused by the coherence of the laser light sources required for tight focusing at the BFP of the objective[81]. Both of these artifacts are more prevalent while imaging cell or tissue samples because the shadowing artifacts are typically caused by large scattering objects, and the interference fringes are less visible in single-molecule imaging due to the sparsity of the sample. These artifacts can be mitigated to an extent by adjusting the incidence angle of the TIRF beam, but this will typically result in leaky or pseudo TIRF illumination, which is unsuitable for imaging samples with a high fluorescence background, as demonstrated in Section 3.2.4.

There exist a variety of methods to suppress imaging artifacts while maintaining clean TIRF illumination; however, each technique has drawbacks. Likely the most common method is to rapidly rotate the focused excitation spot to multiple positions around the periphery of the BFP that contributes to TIRF generation within a single camera exposure. From here on, the region of the BFP that generates TIRF illumination will be referred to as the TIRF annulus. This approach to achieving uniform TIRF has been demonstrated via a variety of methods including refractive optics[82], piezo or galvo mirrors[83-85], a digital micromirror device[86], or acousto-optic deflectors[87]. The result in each case is a time-averaged incoherent superimposition of the excitation intensity

from each azimuthal angle. These methods are effective but require complex moving parts, which limits their use in non-specialized research settings.

Less complex approaches include conjugating an annular mask to the BFP of the imaging objective, so that the entirety of the TIRF annulus is instantly and selectively illuminated[22, 88, 89]. This method is attractive in that the experimental setup only utilizes static components, and the technique enables TIRF illumination with incoherent sources. Without a mask, incoherent sources are typically unsuitable for TIRF illumination due to issues relating to the emitter size being too large when re-imaged at the BFP, or due to insufficient excitation power in the case of microLEDs. However, the annular mask causes power losses on the order of 99%, which greatly limits the potential applications of the technique[89]. Another method of TIRF generation is to use axicon optics to create an excitation ring at the objective BFP[90, 91]; however, this approach tends to have a limited FOV, cause a strong zero-order intensity spike at the center of the FOV that prevents quantitative intensity analysis, or be challenging to implement in a commercial microscope body due to considerations of beam size and working distance.

In this chapter, I describe a custom fiber bundle we designed that reshapes the coupled excitation beam into an annular beam that generates uniform, artifact-free TIRF illumination. The bundle is compatible with coherent or incoherent sources, and greatly improves the power throughput compared to the approach of using annular mask, which is similarly compatible with incoherent sources. I will detail the design of the fiber bundle, characterize the beam uniformity, and demonstrate the applicability of the technique towards artifact-free, intensity-based analysis with single-molecule and cellular imaging. A comparison of the methods of generating TIRF

described above are illustrated at the BFP and imaging plane in Figure 14, along with a schematic of the fiber bundle input and output faces.

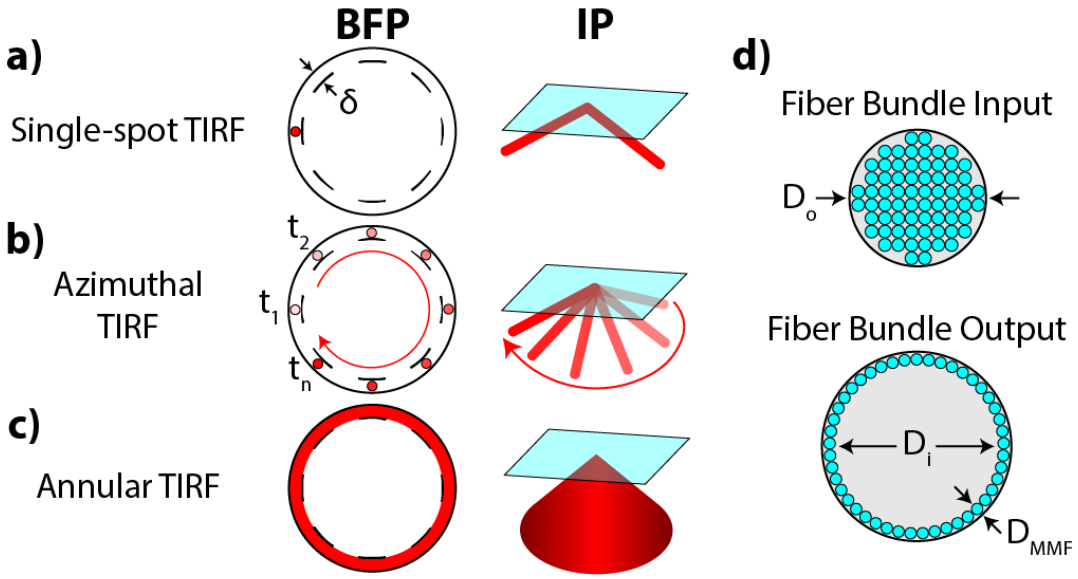

Figure 14. Comparison between (a) single-spot TIRF, (b) azimuthal TIRF, and (c) annular TIRF described at the back focal plane (BFP) and imaging plane (IP). (d) An illustration of the input (top) and output (bottom) faces of the annular fiber bundle. δ denotes the TIRF annulus of the BFP, D_o the outer diameter of the bundle face, D_i the inner space diameter, and D_{MMF} the diameter of an individual multi-mode fiber.

4.1. Methods

4.1.1. Experimental Setup

We used a 470 nm light emitting diode (LED; M470F3, Thorlabs) that directly coupled to the fiber bundle via SMA connectors. For coherent sources, we used 488 nm and 638 nm diode lasers (06-MLD, Cobolt), which were first coupled into a 400 μm MMF (M28L01, Thorlabs) that was attached to a shaker motor (JRF370-18260) which degraded the spatial coherence of the beam before butt-coupling into the fiber bundle. To compare our fiber bundle TIRF with conventional single-spot TIRF we used a 491 nm or 640 nm laser (04-01 Calypso, 05-01 Bolero, Cobolt), which were coupled into a single-mode fiber (P5-488PM-FC-1, Thorlabs), collimated by a 300 mm focal

length lens, and delivered to the microscope via a flip mirror. We measured a power efficiency of roughly 30% when using the fiber bundle with the 638 nm diode, where approximately 76% of the power loss occurred at the coupling between the MMF and fiber bundle input. This was anticipated, because roughly 50% of the fiber bundle input face was void space and the butt-coupling introduced further losses. An improved fiber bundle design will greatly reduce these power losses, such as a photonic lantern design where the entire input face contributes to light coupling.

The annular fiber bundle output was collimated by a 100 mm focal length lens and focused to the BFP of the objective by a 300 mm focal length lens, which was mounted on a manual *xy* and motorized *z* translation stage. This pair of lenses provided the proper magnification of the fiber bundle output at the BFP, which is discussed in greater detail in the following section. Additionally, by adjusting the axial position of the focusing lens by one inch, the excitation beam spot size could be adjusted at the BFP to switch between TIRF and loosely focused epi illumination. The microscope was built around an Olympus IX73 body and a 60x NA 1.45 imaging objective (PLAPON60XOTIRFM, Olympus) was used. The excitation beam and collected fluorescence were passed through and separated by a filter cube (TRF89901v2, Chroma). For most experiments an EMCCD (iXon Ultra 897, Andor) was used with an additional 1.66× relay magnification to bring the total image magnification to 100× to achieve a suitable pixel size for single-molecule imaging; however, a scientific complementary metal oxide semiconductor sCMOS, Zyla 4.2 PLUS; Andor) was used for beam characterization and to demonstrate large FOV TIRF (222 × 222 μm^2). An illustration of the experimental setup is shown in Figure 15.

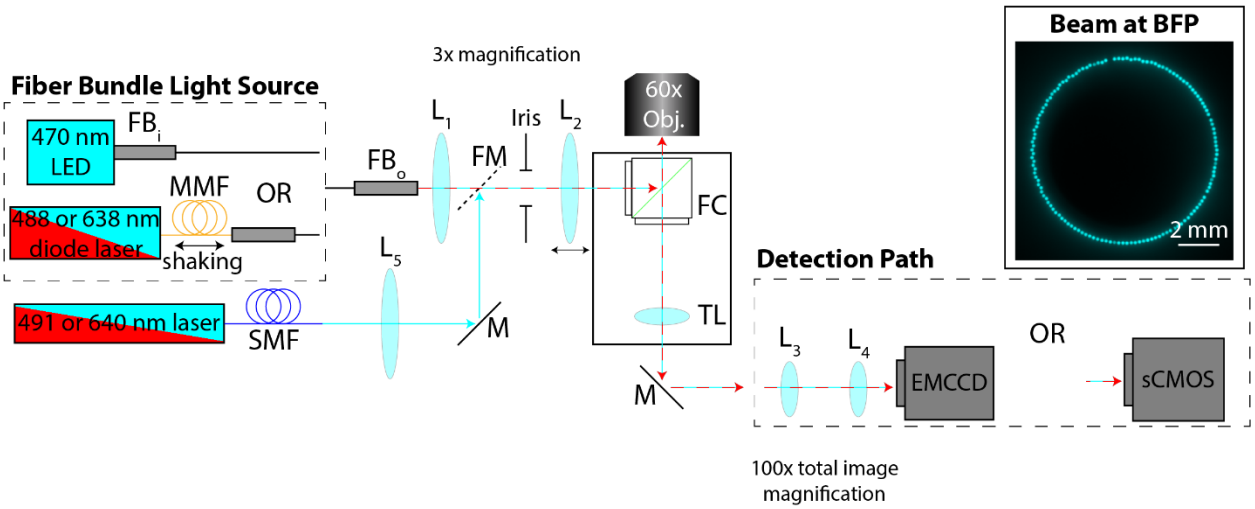

Figure 15. Overview of the experimental setup. Top right insert shows an image of the fiber bundle output at the BFP of the imaging objective. $FB_{i/o}$: Fiber bundle input/output, SMF: Single-mode fiber, MMF: Multi-mode fiber, L: Lens, TL: Tube lens, M: Mirror, FM: Flip mirror, FC: Filter cube.

4.1.2. Annular Fiber Bundle Design

The annular fiber bundle was designed so that when the output facet was magnified 3x, it selectively illuminated the TIRF annulus of our 1.45 NA 60x objective. The first step in the design was to estimate the diameter of the BFP using the geometric optics relationship described by Equation 3:

$$D_{BFP} = 2 * f_{obj} * NA \quad (3)$$

where D_{BFP} is the diameter of the BFP, f_{obj} and NA are the focal length and numerical aperture of the objective, respectively. From this, we calculated that the BFP of our objective was roughly 8.7 mm in diameter. Next, we estimated the width of the TIRF annulus in the BFP using Equation 4:

$$\delta = f_{obj}(NA - n_{sample}) \quad (4)$$

where δ is the width of the TIRF annulus and n_{sample} is the refractive index of the sample, which we estimated to be 1.335. From Equation 4 we estimated the TIRF annulus to be 345 μm wide, which indicates that the centermost 8.01 mm diameter region of the BFP generate epi illumination.

Based on the 3-fold magnification of our collimating and focusing lens and calculated diameter of the BFP, the outer diameter of the fiber bundle output should be 2.9 mm. From the calculated TIRF annulus, we determined that the outermost 115 μm annulus of the fiber bundle would generate TIRF illumination. We contacted LEONI Fiber Optics Inc. to manufacture the fiber bundle and chose to use their 0.22 NA 50/55/65 μm MMFs where the diameters refer to the core/cladding/protective layers, respectively. We had the fiber bundle arranged such that at the input facet the fibers were in a close-packed arrangement to maximize the light coupling efficiency but were rearranged into a single ring around a spacer at the output face. We chose to use a 2.77 mm diameter spacer, leaving a 65 μm annulus that was well-matched to the size of the MMFs, which helped prevent light leakage into epi illumination. The fibers were packaged in an SMA connector at the input end for direct connection to compatible light sources.

4.1.3. 3D Bead Hydrogel Imaging

200 nm crimson beads (F8806, ThermoFisher) were mixed with the precursors for a ~12% acrylamide gel, where the acrylamide was added as the last step. This consisted of roughly 72 μL 0.5x Tris-acetate-EDTA buffer (ThermoFisher), 0.5 μL tetramethylethylenediamine (Sigma), 2 μL ammonium persulfate (Sigma), 5 μL of beads diluted to a target density, and 42 μL of 12% acrylamide mixture. After quickly and thoroughly mixing, the hydrogel mixture was injected into a flow chamber before the gel set. A piezo z-stage (Z-INSERT.100, PiezoConcept) was installed on the microscope stage to accurately control the imaging depth. 20 images were taken over a 2 μm imaging depth in 100 nm steps.

4.1.4. Penetration Depth Measurement

A flow chamber was assembled using a slide and coverslip that had been cleaned by a potassium hydroxide treatment. The flow chamber was wet with 1x PBS before incubating poly-D-lysine (ThermoFisher) for 5 minutes. The flow chamber was washed out with 1x PBS before incubating with 1 μm crimson beads (F8816, ThermoFisher) diluted to a desired, sparse spot density for 10 minutes. The flow chamber was thoroughly washed out with 1x PBS before adding an imaging buffer composed of 2 mM Trolox (Santa Cruz) and an oxygen scavenger (1% w/v dextrose, 1 mg/mL glucose oxidase, 0.04 mg/mL catalase) in 20 mM Tris pH 8.0 and 50 mM NaCl. The sample was excited using the 638 nm diode laser coupled into the fiber bundle.

4.1.5. Beam Uniformity Characterization

Thin dye layer samples were created as described in Section 3.1.2 using Atto 488 (Sigma) and STAR635 (Abberior) dyes on potassium hydroxide cleaned coverslips. The dye layers were excited using the 470 nm LED and 638 nm diode laser, respectively. The beam profiles were imaged using the sCMOS camera to capture the full extent of the illuminated area.

4.1.6. Single-Molecule Imaging

Flow chambers were assembled using dichlorodimethylsilane (DDS) passivated coverslips, which are described in detail in Section 5.1.1. The flow chambers were wet with 1x PBS and 40 pM IgG antibodies labeled with A647 at a degree of labeling of ~1.1 were incubated for 10 minutes to directly immobilize the antibodies onto the coverslip surface. The flow chamber was thoroughly washed out with 1x PBS and imaging buffer was added. The sample was excited by the 638 nm diode laser coupled into the annular fiber bundle with the shaker motor running.

For comparison with single-spot objective TIRF, the 640 nm laser was used to excite the sample with a clipped and expanded Gaussian beam. Images were taken in 20 different regions of the sample to generate intensity distributions. Then, 10 nM of STAR635 was added to the flow chamber as fluorescent background, and the sample was imaged using the annular fiber bundle in TIRF and epi illumination modes.

4.1.7. Cellular Imaging

U2OS cells were grown and treated with a phalloidin actin stain as described in Section 3.1.7. The cells were imaged using the 470 nm LED and 488 nm diode laser coupled into the annular fiber bundle. The coherence of the diode laser was degraded via the shaker motor prior to coupling into the fiber bundle. The same region was imaged using the 491 nm laser for a comparison with single-spot TIRF. Additionally, a 7 × 7 grid of images was acquired using the 470 nm LED coupled into the annular fiber bundle in TIRF and epi illumination to demonstrate high-throughput imaging over a 550 × 550 μm^2 area. A 15% image overlap was used to achieve proper image stitching.

4.2. Results

4.2.1. Confirming TIRF Illumination

The first experiment was performed to verify that the annular fiber bundle generated clean TIRF illumination. For this, a 3D hydrogel sample with embedded fluorescent beads was imaged in TIRF and epi configurations by translating the focusing lens. Images of the hydrogel at various imaging depths are shown in Figure 16.

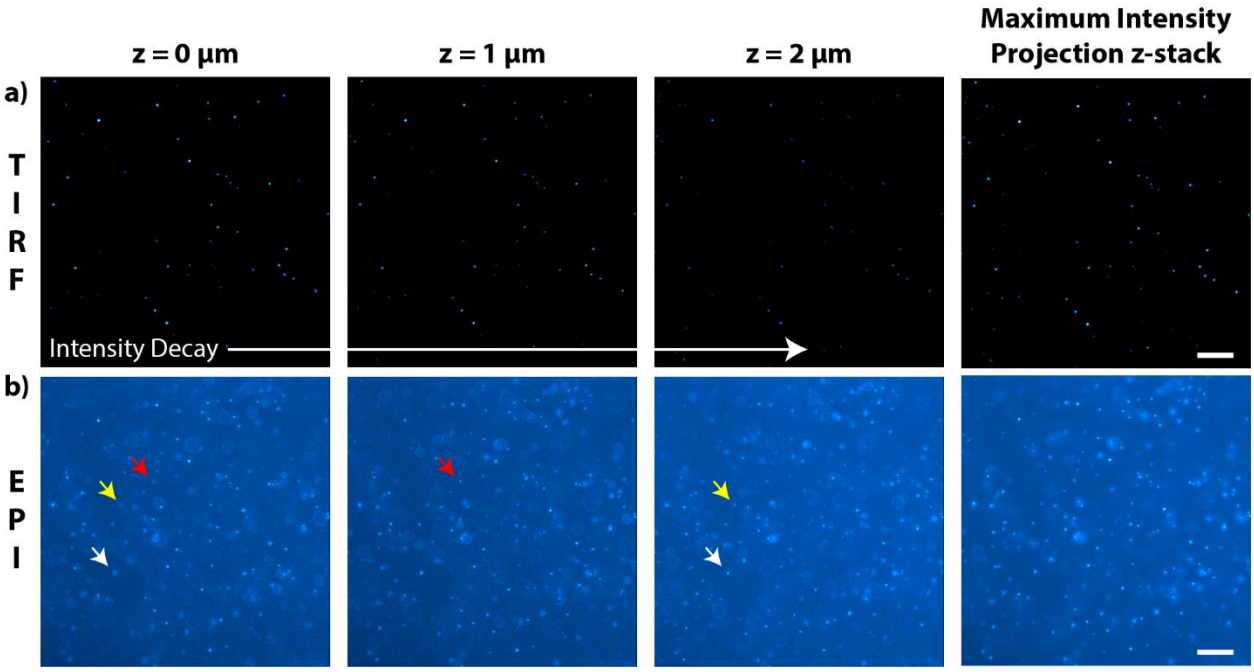

Figure 16. Hydrogel bead imaging. Images taken in (a) TIRF and (b) epi illumination using the annular fiber bundle are shown at imaging depths of 0, 1, and 2 µm. A maximum intensity projection of the entire imaging volume is also shown for comparison. Colored arrows highlight beads displaced from the coverslip surface. Scalebars 10 µm.

Figure 16a shows that when the hydrogel bead sample was imaged using TIRF illumination there was a gradual decrease in the intensity of the beads that were visible at the surface. By contrast, Figure 16b shows that the images taken in epi illumination show an elevated background level due to the fluorescence from out of focus beads, and several beads come into focus at imaging depths away from the coverslip surface. To highlight this effect, a few beads in a dark region of the TIRF images are highlighted with colored arrows in the epi images. A maximum intensity projection of all the images in the stack is also presented, which shows that only the beads are the surface are observed in TIRF illumination, whereas many more beads are visible in the epi images, as expected.

4.2.2. Estimating Annular TIRF Penetration Depth

After confirming that our annular fiber bundle produced clean TIRF illumination without generating any epi illumination contribution, it was imperative to determine the penetration depth of the evanescent field. For this, we imaged 1 μm fluorescent beads that were immobilized on the coverslip surface. The idea is that the shallow TIRF illumination should only excite a bottom portion of the large beads, and thus the beads should have a smaller observed diameter than when imaged using epi illumination[92], which is presented in Figure 17a.

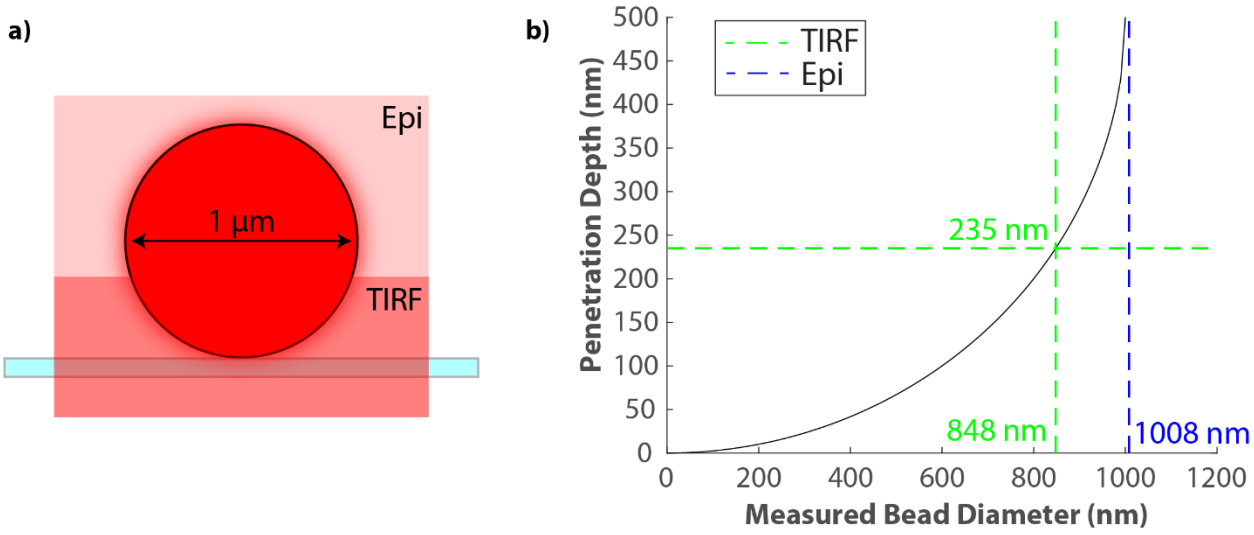

Figure 17. Penetration depth estimation. (a) Schematic of experiment. (b) Plot of the measured bead diameter in the microscope and relation to the penetration depth of the TIRF evanescent field. The observed diameter of the beads under TIRF illumination is plotted in green and epi illumination is plotted in blue.

Figure 17b presents the measured diameters taken from >10 beads imaged under TIRF and epi illumination. We observed an average bead diameter of 1008 nm when using epi illumination, which is in excellent agreement with the expected size. Under TIRF illumination we observed a smaller bead diameter of 848 nm, which corresponded to a penetration depth of 235 nm. This was a reasonable result, because we were imaging with a long wavelength within the visible spectrum where TIRF illumination is expected to have a penetration depth of roughly 50 – 250 nm.

4.2.3. Characterizing the Annular TIRF Beam Uniformity

After confirming the shallow penetration depth of the annular TIRF excitation, we analyzed the uniformity of the beam to assess its applicability for intensity-based analysis. For this we imaged roughly 5 μm thick dye layers using the sCMOS detector to achieve a 222 × 222 μm^2 FOV. The 470 nm LED and 638 nm diode laser were coupled into the fiber bundle to compare incoherent and coherent sources, and the diode laser was used to image the dye layer with and without shaking of the MMF to assess the impact of spatial coherence on the generated excitation. Figure 18 presents images of the dye profiles and the measured intensity lineouts.

Figure 18b shows that without degrading the spatial coherence of the diode laser, imaging artifacts arise because the beams emanating from each individual MMF along the bundle output interfere with one another. By degrading the spatial coherence, the diode laser and LED both yield uniform beam profiles. Intensity lineouts were taken along the diagonal, which were plotted as raw data and after smoothing by adjacent averaging with a 5-datapoint window. The beam uniformity was characterized by calculating the root-mean-square of the lineout intensity. Across the entire sCMOS FOV, the RMS values were 0.79 for both the diode laser and LED, which were slightly degraded due to detector noise. After smoothing, the RMS values increased to 0.84 and 0.86 for the diode laser and LED, respectively. In the centermost 82 × 82 μm^2 region detected by the

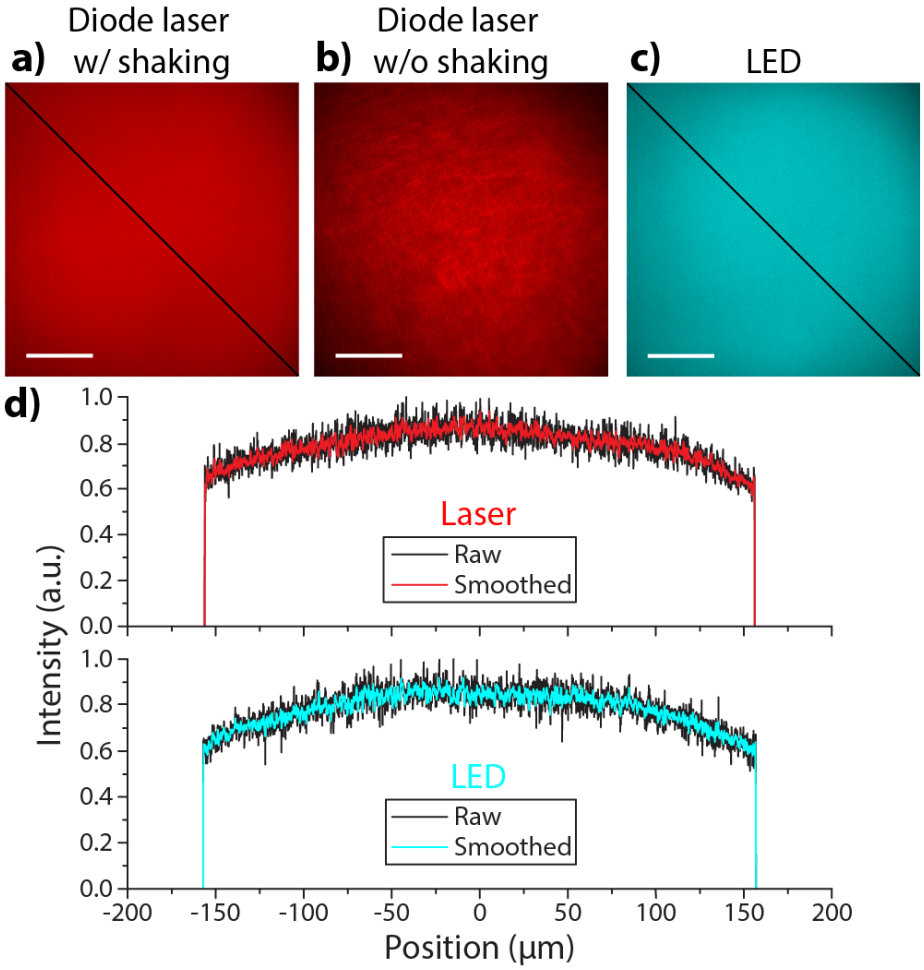

Figure 18. Dye profile measurements. Images taken using (a) the diode laser while shaking the MMF, (b) diode laser without MMF shaking, and (c) the LED. (d) Line profile plots taken as indicated by the black diagonal lines in (a) and (c). Scalebars 50 μm.

EMCCD, the respective smoothed RMS values increased to 0.91 and 0.92, which are comparable to the value of 0.97 achieved by the TopShape refractive beam shaping device used in the previous chapter. However, it is worth noting that the TopShape component required a coherent, Gaussian input beam of a certain size, whereas the annular fiber bundle is insensitive to the characteristics of the input beam so long as the spatial coherence is degraded. Without shaking the MMF, the diode laser yielded an RMS value of 0.77 due to the interference artifacts that arise from the coherent source.

4.2.4. Quantitative Intensity-Based Single-Molecule Imaging

After determining the uniformity of the annular fiber bundle output, we tested if it was possible to perform quantitative intensity-based single-molecule analysis. We imaged IgG labeled with A647 that was immobilized on a coverslip, and generated intensity distributions using images from 20 FOVs. As seen in Figure 19a, the single molecules are well resolved when using the 638 nm diode laser and annular fiber bundle to generate TIRF illumination.

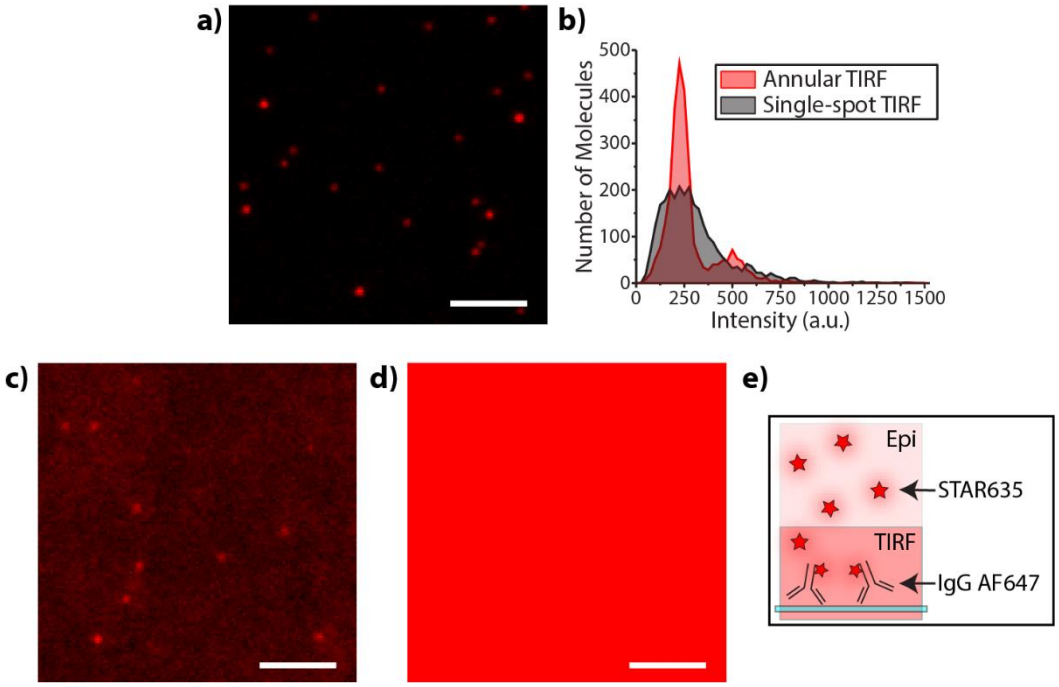

Figure 19. Annular TIRF single-molecule imaging. (a) Immobilized IgG-A647 excited via annular TIRF. (b) Intensity distributions comparing annular TIRF and single-spot TIRF. Images of the IgG-A647 sample after the addition of 10 nM fluorescent background taken using (c) annular TIRF and (d) epi illumination. (e) Schematic of the experiment from c) and d). Scalebars 5 μm.

The sample was also imaged using conventional, single-spot objective TIRF illumination, and intensity distributions for annular TIRF and objective TIRF are shown in Figure 19b. The annular TIRF distribution shows two well-defined peaks, where the position of the smaller second peak is at roughly twice the intensity of the first. The secondary peak represents the small

population of antibodies that were labeled with two fluorophore molecules. By comparison, the single-spot TIRF distribution is broadened due to the nonuniformity of the clipped Gaussian excitation profile, which obscures the secondary population. This demonstrates that the annular TIRF illumination enables quantitative intensity analysis, similar to the TopShape component in the previous chapter. Additionally, it is worth noting that the power efficiency of the fiber bundle is what enabled single-molecule imaging with incoherent excitation, whereas the use of an annular mask cuts the power efficiency to a point where single-molecule imaging is not possible unless a high-power (~1 W) excitation source is used.

Then, 10 nM of fluorescent background was added to the sample to demonstrate the background suppression of the annular TIRF excitation. Figure 19c shows that the single-molecule spots are still resolvable with a signal-to-background ratio of 2.3 (N=20), but Figure 19d demonstrates that when the sample is excited by epi illumination the background saturates the single-molecule signal. This demonstrates that the TIRF excitation produced by the fiber bundle is free of leakage into epi illumination, and a schematic clarifying the concept of the experiment is presented in Figure 19e.

4.2.5. Artifact-Free Cellular Imaging

After characterizing the annular TIRF excitation and showcasing its capability for quantitative intensity analysis, we demonstrated that the incoherent annular excitation enables artifact-free TIRF imaging with cellular samples. U2OS cells were stained to label filamentous actin, which were imaged using the annular fiber bundle with the LED and 488 nm laser diode

light sources. Additionally, we captured images using the 491 nm laser and single-spot TIRF illumination, and a comparison of the three approaches is shown in Figure 20.

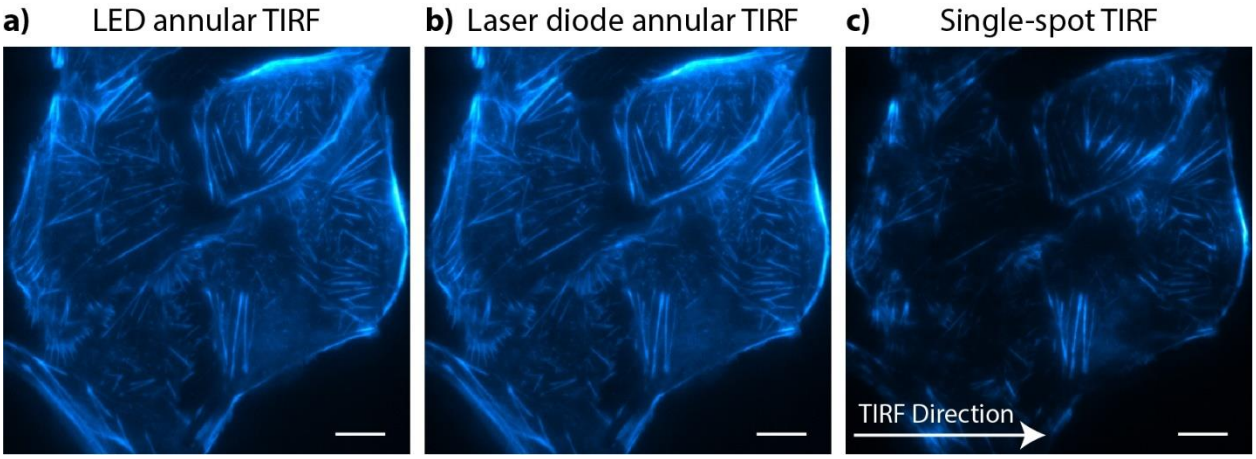

Figure 20. Artefact-free TIRF cellular imaging. U2OS cells with filamentous actin stained by AlexaFluor 488 are imaged using the annular fiber bundle with an (a) LED and (b) laser diode source. (c) An image of the same FOV using conventional single-spot TIRF excitation. Scalebars 10 μm.

It is evident that conventional single-spot TIRF illumination results in a degraded image due to the presence of shadowing artifacts from that roughly follow the direction of the TIRF excitation, and from interference bands that are less visible but arise from the coherent excitation. By contrast, both the LED and laser diode provide a uniform, artifact-free image of the cell sample.

Next, to demonstrate the ease of switching between TIRF and epi illumination and the benefits of uniform excitation, we performed high-throughput stitched imaging of a large 550 × 550 μm^2 FOV. As seen in Figure 21, both illumination modes yielded seamless stitching without a windowpane artifact between individual FOVs. Additionally, TIRF illumination resulted in clear visualization of surface features such as focal adhesions, whereas these features were less pronounced under epi illumination where the cell walls were visible. The boxed region and inset in upper right corners highlight this comparison. It is worth noting that a slightly increased image

overlap was used compared to the stitched imaging in the previous chapter, but this was attributed to the less dense sample rather than issues with illumination nonuniformity.

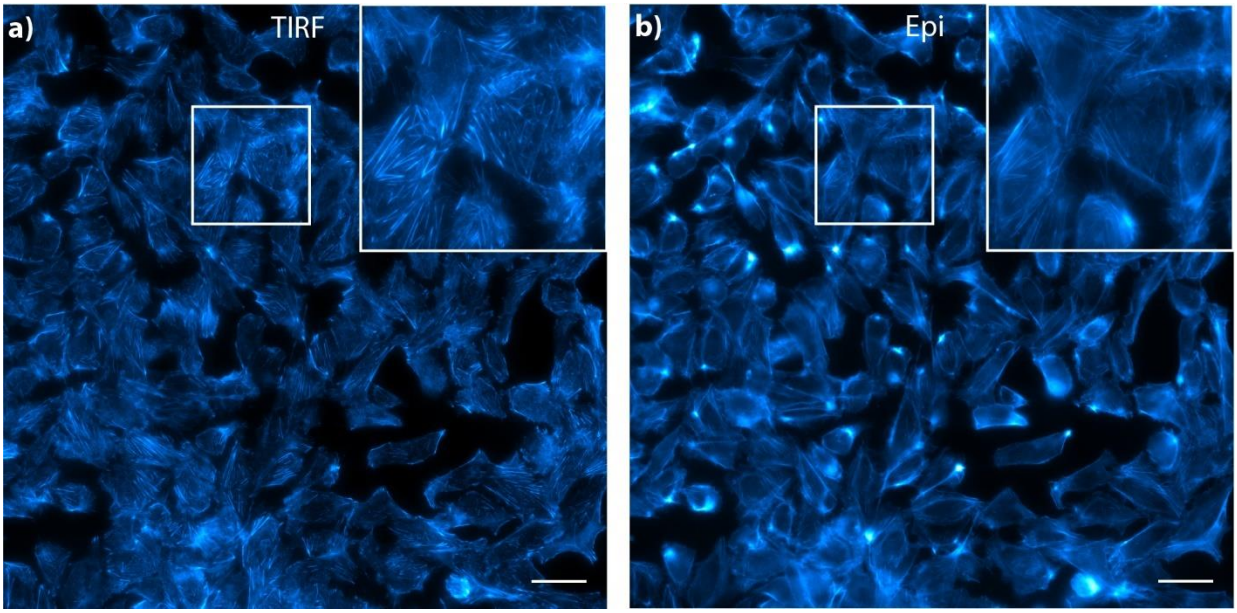

Figure 21. Stitched imaging of U2OS cells with a fluorescent actin stain taken using the annular fiber bundle under (a) TIRF and (b) epi illumination. Scalebars 50 μm.

4.3. Conclusion

This chapter demonstrated that the annular fiber bundle enabled uniform TIRF excitation using incoherent or coherent light sources, provided the spatial coherence was degraded prior to coupling into the fiber bundle. The beam uniformity was sufficient to detect the difference in intensity from antibodies labeled with one or two fluorophores, similar to the single-molecule DNA samples studied in the previous chapter. Once again, this is a key metric in the overall goal of this thesis to determine protein stoichiometry based on the detected fluorescence intensity and demonstrates that uniform illumination is a key component in any intensity-based analysis method. Overall, the performance of the fiber bundle was comparable to that of the refractive beam shaping device in terms of beam uniformity, quantitative intensity analysis capability, and high-throughput

stitched imaging. The main differences stem from the power throughput which is effectively 100% for the refractive beam shaping device compared to ~30% for the fiber bundle when the MMF is used to degrade the coherence of a laser light source. However, the tradeoff in power throughput gives flexibility in the light source used, in that the fiber bundle does not require a beam of a certain size or intensity profile. Conversely, the refractive beam shaping method is compatible with any imaging objective, whereas the annular fiber bundle is designed specific to a certain objective and would be challenging to implement with objectives where the BFP is a different size.

CHAPTER 5: EXPEDITED SINGLE-MOLECULE ASSAY

The previous two chapters focused on making the data acquired from the SiMPull assay more quantitative by employing uniform excitation beams. While translational techniques need to provide useful data about the analyte, they also need to be user-friendly. Often the user of a method will have a different educational or research background than those who developed it, so it is critical that the procedure be straightforward to implement. The SiMPull assay benefits from its similarity to the ELISA assay which is already widely adopted; however, it is hindered by its cumbersome sample preparation protocol.

Single-molecule experiments require a well-passivated surface to maintain specificity to the target analyte and avoid non-specific binding of other biomolecules the microscope coverslip or substrate. By far, polyethylene glycol (PEG) passivation is the most widely adopted passivation method used for single-molecule studies[93, 94], but the protocol for preparing PEG-passivated glass is a time-consuming process that requires overnight incubation. This has sparked the search for alternative passivation methods that maintain non-specific binding levels suitable for single-molecule studies. The ionic detergent Tween-20 has been demonstrated as an effective passivation layer for preventing nonspecific protein adsorption[95], and the combination of dichlorodimethylsilane (DDS) and Tween-20 passivation (DT20) has proven to achieve nonspecific binding levels compatible with single-molecule studies[96]. Treating microscope slides and coverslips with DDS takes a fraction of the time of PEG passivation, requiring only a few hours rather than over 24 hours, and the Tween-20 passivation step takes five minutes and is readily incorporated various single-molecule sample preparations[97-99].

In addition to the lengthy passivation steps, the tedious sample preparation limits the appeal of SiMPull assays. Traditionally, there are four different antibodies in addition to the target protein that need to be incubated sequentially for at least 20 minutes per incubation step. Considering time for washing steps and additional linkage molecules such as biotin and NeutrAvidin, a typical sample takes more than 2 hours to prepare. The primary and secondary antibodies cannot be incubated ahead of time due to the bivalent nature of IgG antibodies. Incubation of the primary and secondary antibodies in solution results in large, aggregated complexes due to a hand-holding behavior, where secondary antibodies will bind to multiple primary antibodies. This creates large, extremely bright complexes that can overwhelm the single-molecule signal when viewed in the microscope. Alternatively, monovalent F(*ab*) antibody fragments can be used instead of traditional IgG or F(*ab'*)$_2$ secondary antibodies. The single binding site of F(*ab*) fragments prevents the aggregation effect when primary and secondary antibodies are pre-incubated together, which has been used to lower the number of incubation and washing steps in immunofluorescence labeling[100].

In this chapter I will show that the use of DT20 passivation and F(*ab*) antibody fragments as secondary antibodies are well-suited to SiMPull assays. The combination of a shortened passivation protocol and the ability to pre-incubate samples greatly facilitates SiMPull assays, making them a much more appealing tool to researchers and clinicians. Additionally, the primary capture antibodies can be adhered directly to the DDS surface via hydrophobic interactions, which further reduces the number of steps in preparing an assay. A comparison between the DDS SiMPull assay and the traditional PEG SiMPull assay is shown in Figure 22.

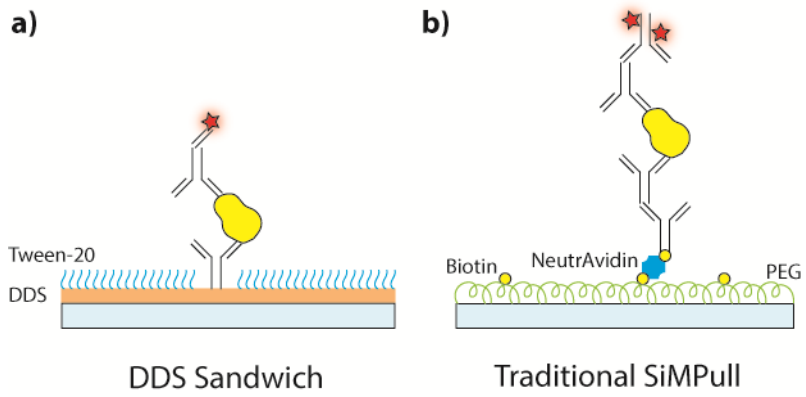

Figure 22. Illustrations comparing the (a) DDS sandwich SiMPull and (b) traditional PEG SiMPull assays**.**

5.1. Methods

5.1.1. Glass Preparation Protocol

Glass coverslips and slides were treated with DDS following previously published protocols[96]. Six holes were drilled along both long edges of glass microscope slides, then the slides and coverslips were sonicated with 1% w/v Alconox, acetone, and methanol sequentially for 20 minutes each and washed thoroughly with MilliQ water between each step. After cleaning, the slides and coverslips were sonicated for 1 hour in 1 M potassium hydroxide to etch away surface roughness. The slides and coverslips were rinsed and briefly sonicated with MilliQ water, dried using a stream of air, and placed in a polyethylene slide holder filled with hexane (H303-4, Fisher Chemical). The hexane in the slide holder was replaced 3 times to remove residual water and contaminants, then roughly 50 µL of DDS (440272, Sigma-Aldrich) was injected into the slide holder. The needle tip was submerged below the hexane prior to injection to prevent the DDS from reacting with moisture in the air. The DDS hexane solution was incubated for 1 hour before it was removed, and the glass was sonicated for two rounds in methanol and one round in hexane for one minute each. The slides and coverslips were rinsed in MilliQ, dried under an air stream, then

vacuum sealed and stored at −20°C until use. PEG coated coverslips and slides were prepared as described in past literature[69] and previously in this report.

5.1.2. SiMPull Protocol

The DDS-treated slides and coverslips were assembled into flow chambers[69] and wet with 1x PBS before introducing a sample. For DDS SiMPull experiments, primary mouse antibody was diluted to a concentration of 10 μg/mL in bPBS and adhered to the DDS surface by incubation in the flow chamber for 10 minutes, after which the flow chamber was thoroughly washed out with PBS. The capture antibodies used were anti-α-tubulin (T6074, Sigma-Aldrich), anti-α-synuclein (610787, BD BioSciences) and biotinylated anti-GFP (600-106-215, Rockland). For direct adhesion experiments, the protein (EGFP, TP790050, OriGene; tubulin-TMR, TL590M, Cytoskeleton; α-SYN, S-001-1, rPeptide) was diluted to the desired concentration in bPBS and incubated in the wetted DDS flow chamber for 10 minutes. After the capture antibody or protein had been adhered to the DDS surface, Tween-20 (P7949, Sigma-Aldrich) was diluted to a concentration of 0.2% in T50 buffer (10 mM Tris, 50 mM NaCl) and incubated for 5 minutes to passivate the flow chamber, after which it was thoroughly washed out with PBS. For sandwich-style experiments, the target protein was diluted to the desired concentration in bPBS and incubated for 20 minutes, where protein concentration was dependent on the binding affinity of the capture and detection antibodies. The flow chamber was thoroughly washed with PBS after adding the protein of interest, and 1 μg/mL of the appropriate rabbit primary detection antibody (ab52866, ab51252, ab183734 from abcam) and 300 ng/mL F(*ab*) (711-007-003, Jackson ImmunoResearch) labelled with A647 (Alexa Fluor 647; A20006, Invitrogen) were diluted in

bPBS and sequentially incubated for 20 minutes each, washing with PBS between each step. Imaging buffer composed of 2 mM Trolox (Santa Cruz) and an oxygen scavenger (1% w/v dextrose, 1 mg/mL glucose oxidase, 0.04 mg/mL catalase) in 20 mM Tris pH 8.0 and 50 mM NaCl was added to the flow chamber before imaging to minimize fluorophore photobleaching and blinking.

For SiMPull experiments using PEG-passivated glass, the flow chamber was assembled as before, wet with PBS, incubated with 20 μg/mL Neutravidin (31000, Thermo Scientific) for 5 minutes, and washed out with PBS. 5 μg/mL of goat biotinylated anti-mouse antibodies (ab97033, abcam) were incubated for 5 minutes and washed out with PBS. Then, 2.5 μg/mL primary mouse antibody, the protein of interest, 1 μg/mL primary rabbit antibody, and 300 ng/mL F(ab')$_2$ (711-006-152, Jackson ImmunoResearch) labelled with A647 were incubated sequentially for 20 minutes each, washing thoroughly with PBS between each step.

5.1.3. Pre-incubation of SiMPull Assay Components

For SiMPull experiments using pre-incubated detection antibodies, primary antibodies were incubated with F(*ab*) fragments at respective concentrations of 200 nM and 675 nM at 4°C, diluted to a primary antibody concentration of 8 nM in bPBS, and incubated for 20 minutes in the flow chamber to label the target protein. For experiments where the protein, primary detection antibody, and F(*ab*) fragments were all pre-incubated together, the samples were incubated at respective concentrations of 110 nM, 250 nM, and 500 nM at 4°C. The mixture was diluted in bPBS to the final concentration dependent upon the binding affinity of the capture antibody and

incubated for 20 minutes. All samples were thoroughly washed out and imaging buffer was added before analysis in the microscope.

5.1.4. Imaging and Analysis Parameters

We used the refractive beam shaping device described in Chapter 3 (TopShape, asphericon GmbH) with 561 nm and 638 nm diode lasers (Cobolt) to build an objective-TIRF microscope equipped with flat-field illumination[101], and used excitation intensities of 10 W/cm^2. For EGFP experiments, a 488 nm diode laser (Cobolt) was used at an excitation intensity of 20 W/cm^2. Each image was acquired by averaging 10 frames at a 50 ms exposure time into a single frame. Intensity distributions were generated from twenty FOVs (82 x 82 μm^2) for each sample, where custom MATLAB scripts[101] were used to localize single-molecule spots and extract the intensity data, as described previously.

To minimize photobleaching in colocalization experiments using tubulin-TMR and F(*ab*)-A647, each FOV was first imaged using 638 nm excitation before capturing the image using the 561 nm laser. To calculate the colocalization percentage between the two color channels, the single-molecule spots in the image captured using 638 nm excitation were first localized and compared with the locations of molecules in the 561 nm image of the same FOV. Molecules that were detected within adjacent pixels (160 nm pixel-size) were considered colocalized. The colocalization percentage was calculated according to Equation 5:

$$Colocalization\ \% = \frac{2N_C}{N_F+N_T+N_C} \times 100 \quad (5)$$

where N_C, N_F, and N_T are the number of colocalized spots, individual F(*ab*)-A647 and tubulin-TMR spots, respectively.

5.1.5. Measuring Aggregation Induced by Pre-incubation

Biotinylated primary rabbit anti-α-SYN antibodies (LS-C370648, LSBio) were diluted to a concentration of 200 nM and incubated at 4°C with 400 nM of either A647-labeled IgG antibodies (A31573, Invitrogen) or antibody fragments. The pre-incubated mixture was diluted to a biotinylated antibody concentration of 50 pM, incubated for 5 minutes in a Neutravidin-coated PEG flow chamber, and thoroughly washed out with PBS. Then, imaging buffer was added, and the sample was imaged. A similar sample was created using the standard method of sequential incubation, which was used as a comparison to determine a cut-off intensity value below which 99% of the molecules were contained in the intensity distribution. For pre-incubated samples, any antibodies detected at intensities above the cut-off value were considered to be aggregated. The laser power and imaging conditions were maintained when imaging samples at different stages of pre-incubation, which enabled direct comparison of the intensity distributions.

5.1.6. DDS SiMPull Assay Using Crude Cell Lysates

U2OS cells (HTB-96, ATCC) were grown in McCoy's 5A medium (SH30270.01, GE Healthcare) supplemented with 10% fetal bovine serum (F2442, Sigma) and 1% Pen-Strep (15140122, ThermoFisher). The cells were collected and lysed via three cycles of freezing and thawing in liquid nitrogen[69]. The lysate was centrifuged at 1,000 g for 10 minutes at 4°C, and the supernatant was collected for use in SiMPull assays. The overall protein concentration was measured via the absorbance at 280 nm. All samples were kept on ice, and experiments were performed within 6 hours of lysis to minimize protein degradation due to protease activity.

The cell lysate was diluted 10-fold to an overall protein concentration of 60 μg/mL before use in a typical α-tubulin DDS SiMPull assay, whereas the lysate was undiluted in α-SYN SiMPull assays. For expedited SiMPull assays, the undiluted lysate was pre-incubated with 250 nM rabbit anti-α-tubulin antibody and 500 nM F(*ab*)-A647. The mixture was incubated for 1 hour at 4°C and diluted to 10 times the initial lysate concentration before injection to the flow chamber.

5.2. Results and Discussion

5.2.1. Assessing DT20 Passivation

The first set of experiments were aimed at determining if DT20 passivation provides sufficient prevention of nonspecific binding when used in SiMPull assays. To this end, we measured the amount of nonspecific binding for a variety of conditions, as shown in Figure 23a, using antibodies against α-SYN, α-tubulin, and EGFP. Figure 23b shows the average number of molecules per FOV using α-SYN and the associated antibodies for each case depicted, and a representative image of the SiMPull experiment in case 8 is shown as an inset in Figure 23b. Besides cases 4 and 8, there was a negligible degree of observable nonspecific binding, indicating that DT20 passivation was suitable for SiMPull assays and there was minimal crosstalk between antibodies. Case 4 shows that despite the Tween-20 passivation layer, a small percentage of α-SYN molecules were able to adhere to the DDS surface, but this was less than 5% of the single-molecule spots observed from the 10 nM α-SYN SiMPull assay in case 8 and was considered acceptable.

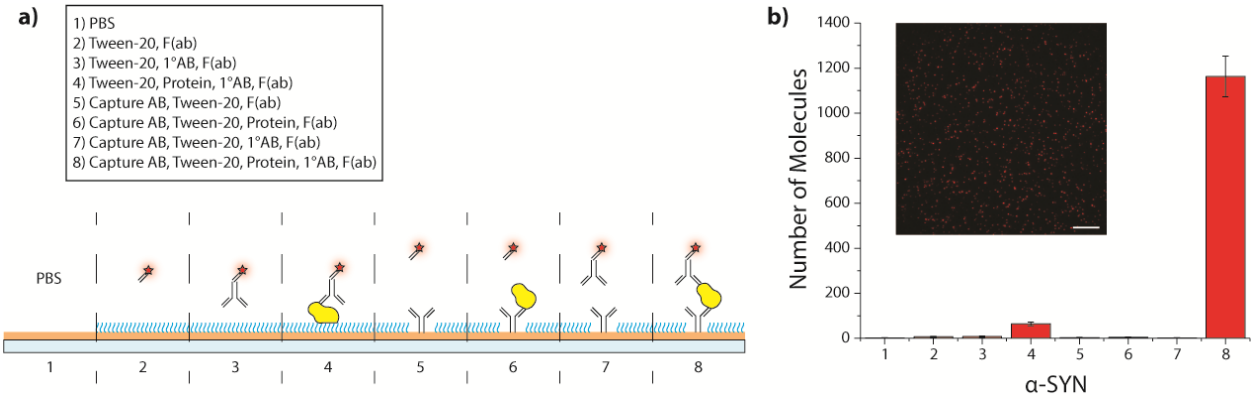

Figure 23. Assessing DT20 passivation. (a) Illustrations and descriptions of each nonspecific binding experiment. (b) Average number of spots detected per FOV for each case in a) for α-SYN and the associated antibodies. Inset, a representative SiMPull image from case 8. Error bars denote the standard deviation from the mean. Scale bar, 10 μm.

Similar tests were conducted using 3 nM of tubulin-TMR and its associated antibodies, which are presented in Figure 24a. Again, a negligible amount of nonspecific binding was observed, and roughly 5% of the number of tubulin-TMR molecules detected in case 8 were non-specifically bound to DT20 surface in case 4. However, in these experiments very few of the protein molecules were detected by F(*ab*)-A647. Two possible explanations are that the tubulin-TMR molecules become denatured after adhering to the DDS surface, or that the binding epitope of the primary detection antibody preferentially interacts with the hydrophobic DDS surface, either of which would prevent proper labeling and detection in the microscope. Figure 24a shows that in cases 5-7 there was a small amount of crosstalk between the F(*ab*)-A647 fragments and the primary capture antibody for α-tubulin, contrary to the results from α-SYN experiments presented in Figure 23. The amount of antibody crosstalk was measured to be roughly 7% or less than the number of spots detected in SiMPull experiments. The F(*ab*) fragments were not pre-adsorbed to assess cross-reactivity with antibodies from other species, so it is reasonable to expect that they may interact with mouse IgG antibodies. Colocalization experiments between α-tubulin-TMR and the F(*ab*)-

A647 fragments were performed and are shown in Figure 3b. The degree of colocalization in the SiMPull assay was measured to consistently range between 50-60% using Equation 5.

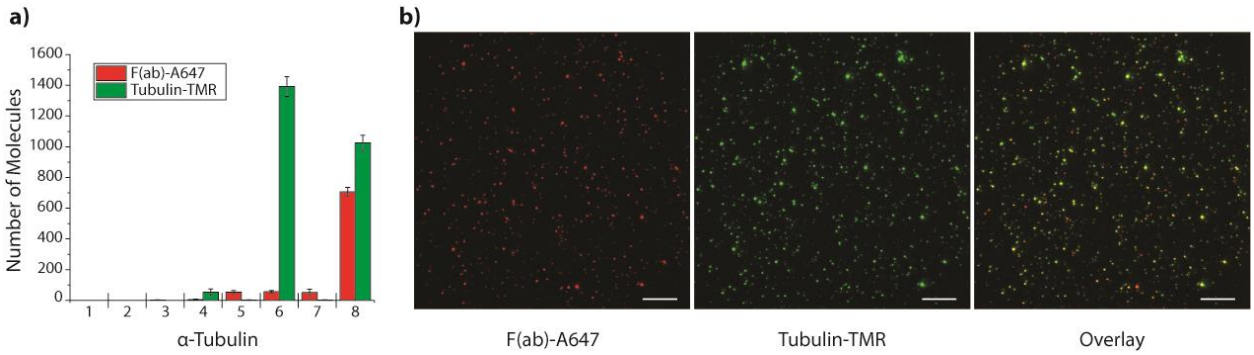

Figure 24. Tubulin-TMR DT20 experiments. (a) Characterizing the non-specific binding of tubulin-TMR and its associated antibodies. Error bars show the standard deviation from the mean. (b) SiMPull images and an overlay of the same FOV with F(*ab*)-A647 shown in red and tubulin-TMR shown in green. Scale bars, 10 μm.

We also performed similar experiments using 1 nM EGFP, where while we observed minimal nonspecific binding, but were unable to label EGFP with F(*ab*)-A647. The inability of the detection antibodies to bind to the immobilized EGFP could be caused by low valency or the primary capture and detection antibodies attempting to bind to the same epitope on EGFP. This is discussed further in Section 5.2.3. Direct Adhesion of Proteins to DDS Coverslips.

5.2.2. Comparing DT20 Performance to PEG

After confirming that DT20 passivation was compatible with our SiMPull assays, we performed experiments comparing the assay results to ones performed using a PEG-passivated flow chamber to assess if the DT20 passivation altered the results in any way. For this, we first compared the number of detected molecules and the amount of nonspecific binding on 10 nM α-SYN and 3 nM α-tubulin SiMPull assays, where nonspecific binding was measured as in case 7 in Figures 23 and 24 where only the target protein was omitted from the assay. Because Tween-20 is

a detergent and is known to remove some proteins from the DDS surface[96], the primary capture antibody concentration in the DT20 SiMPull assays was 4-fold higher than the assays performed in PEG flow chambers. The results of the spot counting and nonspecific binding comparisons using α-SYN and α-tubulin are presented in Figure 25a and 25b, respectively. There was an observed 0.7-fold and 0.9-fold difference in the number of molecules from the α-SYN and tubulin-TMR SiMPull assays performed on DT20 compared to PEG. While statistically significant, these differences were within the range of fluctuations caused by dilution errors and differences in flow chamber sizes. However, it is possible that the binding affinity of the primary capture antibodies to their target protein may be reduced after DT20 passivation, and the significance of this effect may be different for each antibody. The amount of observed nonspecific binding for both α-SYN and α-tubulin was slightly lower when using DT20 passivation than PEG. There was significant binding of the F(*ab*)-A647 fragments to the biotinylated antibodies used in these experiments, so F(*ab'*)$_2$-A647 was used instead.

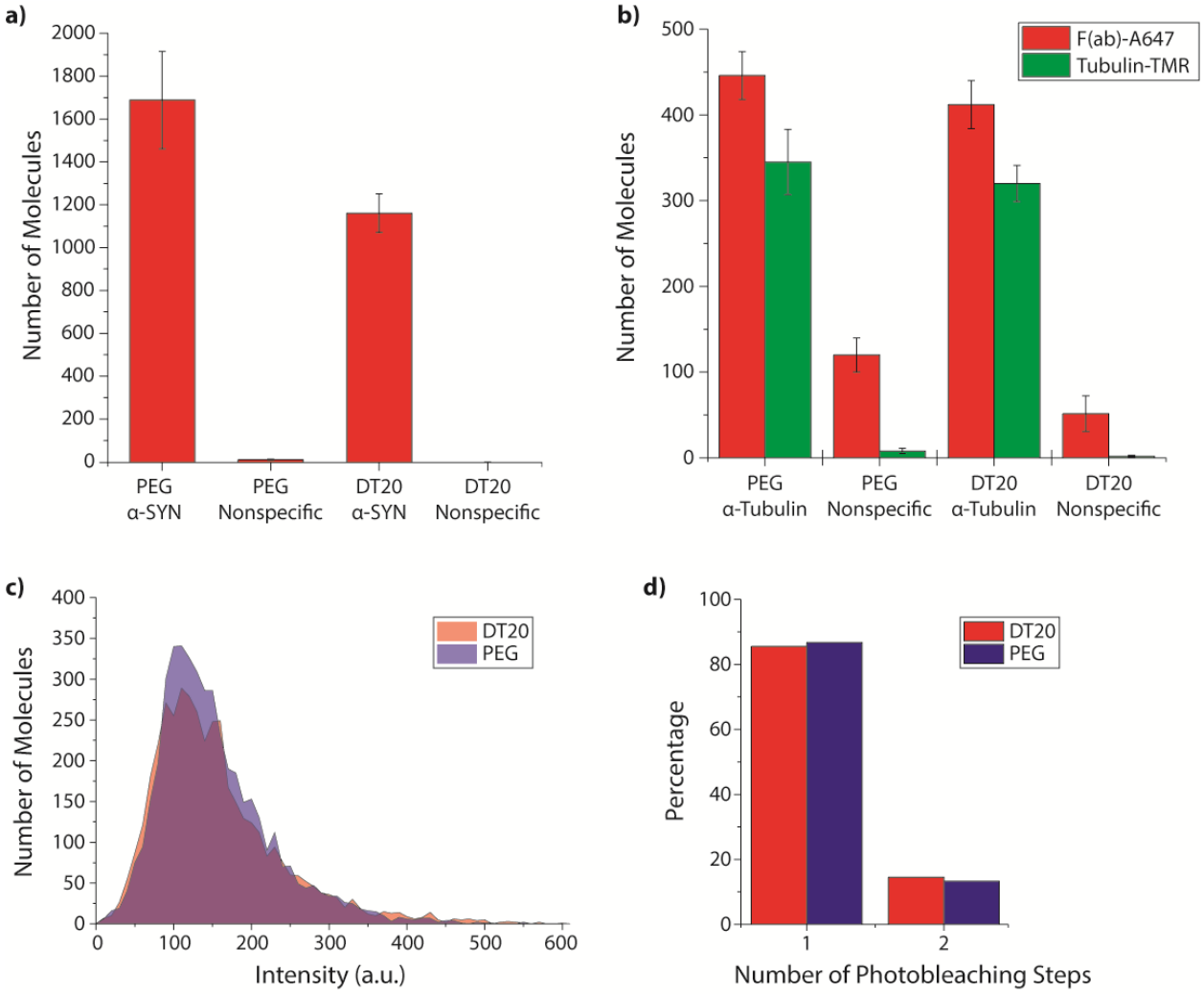

Figure 25. Comparing DT20 performance to PEG. The average number of spots observed and nonspecific binding per field-of-view when using PEG and DT20 surfaces for (a) α-SYN and (b) tubulin-TMR. Error bars show the standard deviation from the mean. (c) EGFP intensity distributions on PEG and DT20 surfaces. (d) EGFP photobleaching steps on PEG and DT20 surfaces.

Next, we analyzed if DT20 affects the fluorescence intensity by comparing EGFP immobilized on PEG and DT20 surfaces, where no change was observed in the intensity distribution (Figure 25c) nor the number of photobleaching steps (Figure 25d). Experiments using tubulin-TMR similarly showed no changes to the measured fluorescence intensities or colocalization percentages, which were 57.8 ± 3.2% and 56.0 ± 2.5% for PEG and DT20,

respectively. Thus, it was determined that the DT20 passivation does not significantly affect the results of SiMPull experiments in terms of the number of detected molecules, the detected fluorescence intensity, nor the photophysics.

5.2.3. Direct Adhesion of Proteins to DDS Coverslips

Next, we tested if the SiMPull assay protocol could be shortened by directly adhering proteins to the hydrophobic DDS surface, as depicted in Figure 26a and similar to indirect ELISA. The concentration of tubulin-TMR was increased to 10 nM compared to the 3 nM used for sandwich DDS SiMPull due to the removal of protein caused by Tween-20. Figure 26b shows that tubulin-TMR was successfully labelled by F(*ab*)-A647, and the number of single-molecule spots observed in both color channels was comparable to that of sandwich SiMPull. Additionally, direct adhesion gave a colocalization percentage of 57.2 ± 1.9%, which was very similar to that of sandwich SiMPull where the colocalization percentage was 55.5 ± 2.6%.

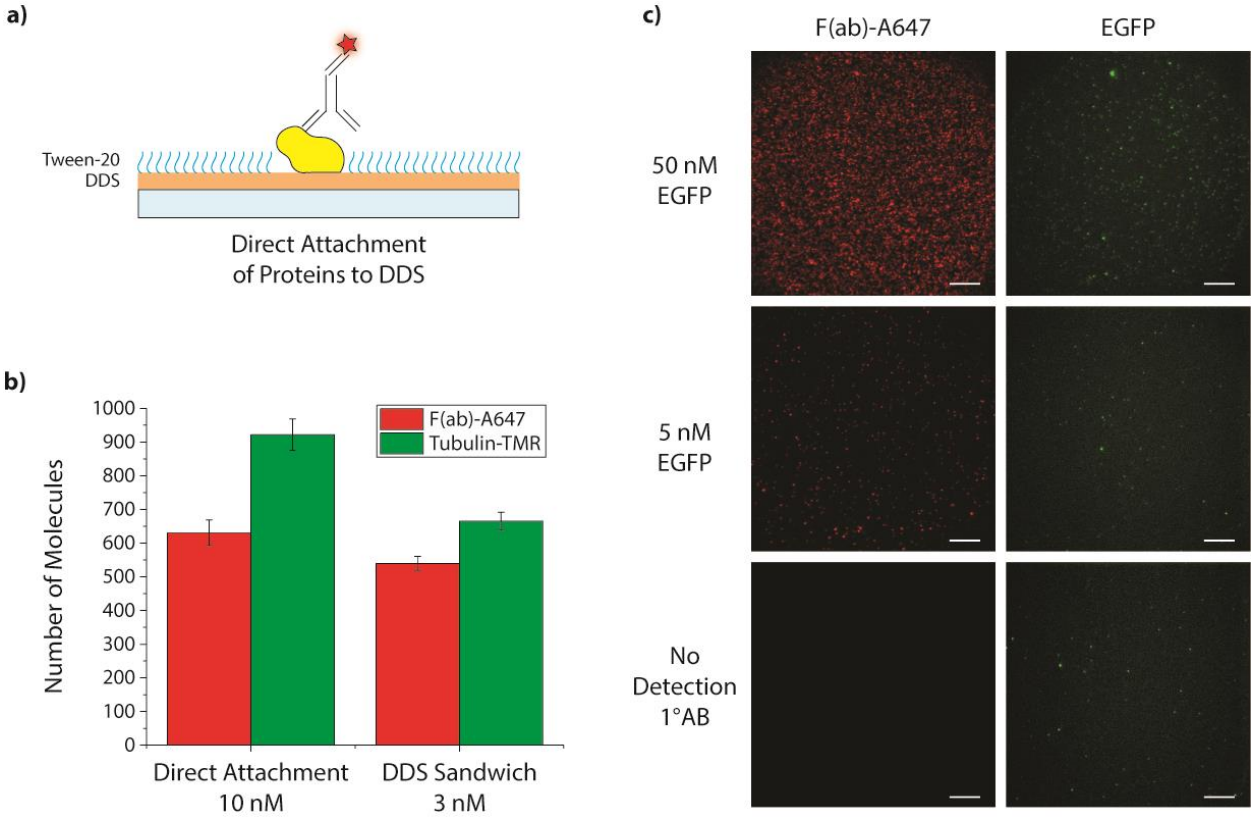

Figure 26. Adhering proteins directly to DDS coverslips. (a) Illustration of the experiment. (b) Comparison of the average number of molecules per field-of-view in direct attachment and sandwich SiMPull experiments with tubulin-TMR. (c) Images from direct adhesion EGFP experiments demonstrating the reduction in EGFP fluorescence where EGFP is shown in green and *F*(*ab*)-A647 shown in red. Scale bars, 10 μm.

While it is possible to directly immobilize proteins to the coverslip surface using DT20 SiMPull assays, similar experiments using EGFP showed that the DDS surface may alter the target protein. When EGFP was immobilized directly to the DDS surface we observed a significant reduction in the number of detected EGFP spots (Figure 26c), but the number of F(*ab*)-A647 spots scaled with the concentration of EGFP used in the assay. When the primary detection antibody was excluded from the experiment no F(*ab*)-A647 was observed, indicating that the F(*ab*) fragments were not nonspecifically bound to the DDS surface. To test if Tween-20 caused the loss of fluorescence, EGFP was diluted in PBS and Tween-20 but absorption measurements at 280 nm

and 488 nm showed no change in the observed spectrum. From these experiments, it was deduced that the EGFP molecule likely deformed after interacting with the DDS surface which affected the excitable dipole of EGFP such that the molecule no longer fluoresced. It was assumed that the binding epitope for primary detection antibody was unaffected and still accessible after EGFP was immobilized on the DDS surface. It is likely that the effects of the protein interacting with the DDS surface are more prominent with EGFP because the overall protein structure creates the excitable dipole for fluorescence, compared to α-tubulin-TMR where a fluorophore is covalently bound to the protein. These experiments indicated that it is possible to adhere proteins directly to the DDS surface for SiMPull experiments, but this method is not recommended due to the potential of altering the protein structure, which has been observed in similar ELISA experiments[102]. Note that EGFP was successfully labeled with F(*ab*)-A647 in these indirect SiMPull experiments, contrary to the sandwich SiMPull experiments in Section 5.2.1. This demonstrates that the primary capture and detection antibodies used in the sandwich experiments were targeting the same epitope on EGFP, which prevented the observation of F(*ab*)-A647 signal.

5.2.4. Expedited SiMPull Assay Using Pre-Incubated F(*ab*)*-A647*

Experiments were conducted to test if the sample preparation time for a SiMPull assay can be reduced by pre-incubating the detection antibodies when monovalent F(*ab*) fragments are used. Initial experiments were performed using biotinylated rabbit anti-α-SYN antibodies which were mixed separately with F(*ab*), F(*ab'*)$_2$, and IgG that were labeled with A647 to assess if monovalency prevents the aggregation behavior. After incubation, the samples were diluted and immobilized on Neutravidin-coated flow chambers, and Figure 27a shows intensity distributions

from each taken after 6 hours of incubation. The percentage of aggregated molecules was determined from the cut-off intensity described in Section 5.1.5 and plotted at various timepoints in Figure 27b. It was observed that roughly 25% of the detected molecules in the F(*ab'*)$_2$ and IgG samples were aggregated after just 1 hour of pre-incubation, whereas the F(*ab*) sample had essentially no aggregated molecules even after pre-incubation for 10 days. The IgG sample showed a reduction in the percentage of aggregated molecules after 24 hours of incubation, which may be attributed to large, aggregated complexes adhering to the walls of the sample vial via enhanced electrostatic interactions. Overall, these results indicate that F(*ab*) fragments can be pre-incubated with primary antibodies without causing aggregation due to their monovalent binding characteristics[100, 103]. Additionally, experiments using standard, sequential incubation were conducted and a similar average number of molecules per FOV were observed for F(*ab*), F(*ab'*)$_2$, and IgG, which indicates they have a comparable binding affinity.

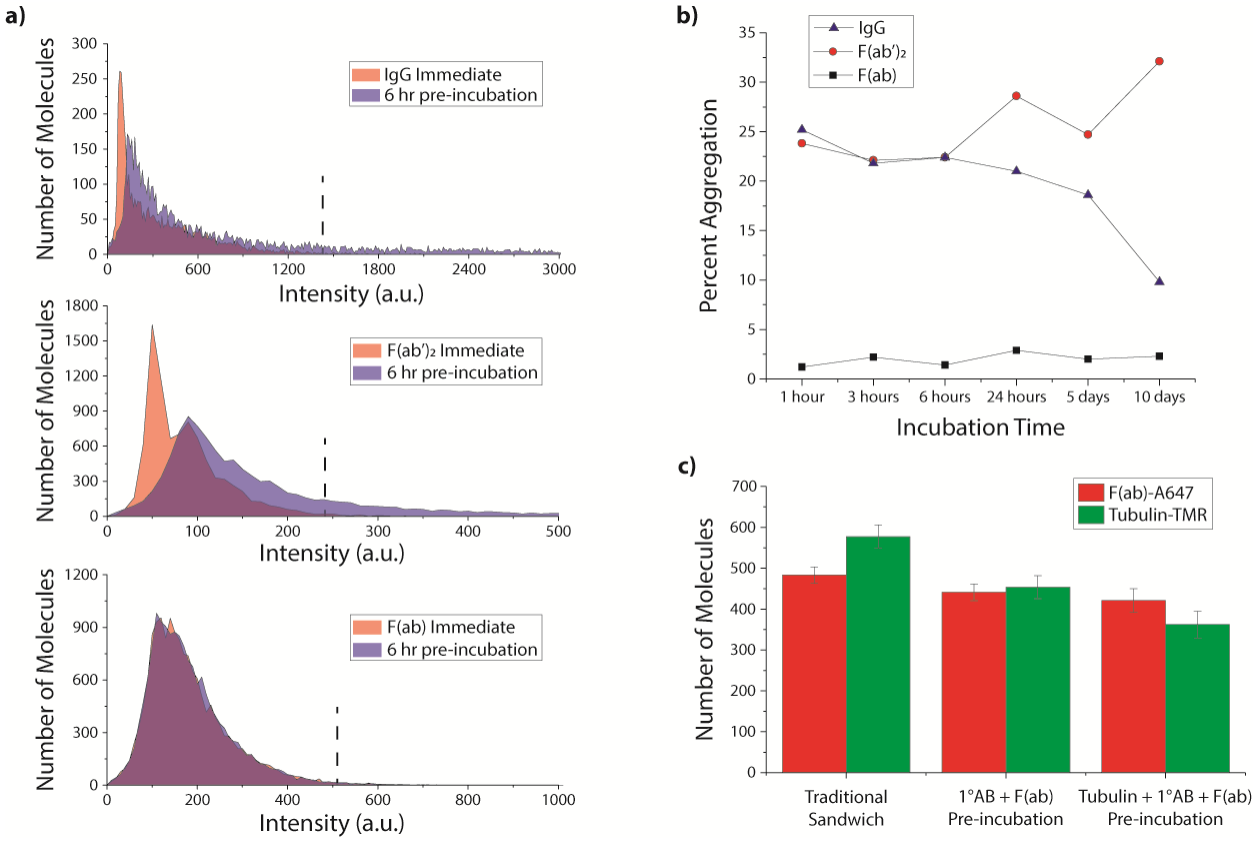

Figure 27. Pre-incubation of SiMPull detection antibodies. (a) Intensity distributions comparing sequential incubation in the flow chamber and samples pre-incubated for 6 hours using (top) whole IgG, (middle) *F*(*ab'*)$_2$, and (bottom) *F*(*ab*). Dashed lines show the cut-off intensity used to determine the aggregation percentage. (b) Plots showing the percentage of aggregated molecules throughout pre-incubation. (c) The number of observed *F*(*ab*)-A647 and tubulin-TMR molecules for traditional sandwich SiMPull, pre-incubation of 1°AB and *F*(*ab*)-A647, and pre-incubation of tubulin-TMR, 1°AB, and *F*(*ab*)-A647. Errorbars show standard deviation from the mean.

After confirming that the F(*ab*) fragments could be pre-incubated without inducing aggregation, we performed experiments to see if the pre-incubated antibody solutions could be used in SiMPull assays without altering the intensity analysis. In addition to incubation of the F(*ab*)-A647 with the primary detection antibody, samples where the F(*ab*)-A647, primary detection antibody, and tubulin-TMR were pre-incubated together were also tested in the SiMPull assays and compared with the standard protocol of sequential incubation in the flow chamber. Figure 27c shows that in each experiment, the average number of observed molecules for each

color channel was comparable. Sequential incubation and pre-incubation of the primary and secondary antibodies both yielded similar colocalization percentages of 52.8 ± 2.9% and 53.5 ± 4.1%, respectively. By contrast, the degree of colocalization increased to 72.8 ± 2.6% for the case where the protein, primary antibody, and F(*ab*) were all pre-incubated. The colocalization increase was attributed to the lengthened incubation time with the target protein and increased mobility of the molecules in solution compared to when immobilized on the coverslip. These results demonstrate that pre-incubation of the components of a SiMPull assay can be used to significantly shorten the sample preparation time while also increasing the assay sensitivity.

5.2.5. DDS SiMPull Using Cell Lysates

Finally, we tested if DT20 passivation was suitable when crude cell lysates were used with the SiMPull assay. U2OS cells were grown, lysed, and the soluble proteins were collected and diluted 10-fold for use in an α-tubulin pull-down assay. Similar to the experiments using recombinant protein, the number of detected spots and the fluorescence intensity distributions were compared between endogenous SiMPull assays performed using PEG and DT20 passivation, and it was observed that similar to the experiments with recombinant protein, the DT20 surface does not affect endogenous SiMPull experiments. After confirming the DT20 passivation scheme was compatible with endogenous protein analysis and F(*ab*) pre-incubation, we performed SiMPull using the standard protocol of sequential incubation in the flow chamber and compared the results with samples pre-incubated for one hour. We tested pre-incubation of the anti-α-tubulin primary detection antibody and F(*ab*)-A647, as well as samples where the lysate, primary detection antibody, and F(*ab*)- A647 were all incubated together.

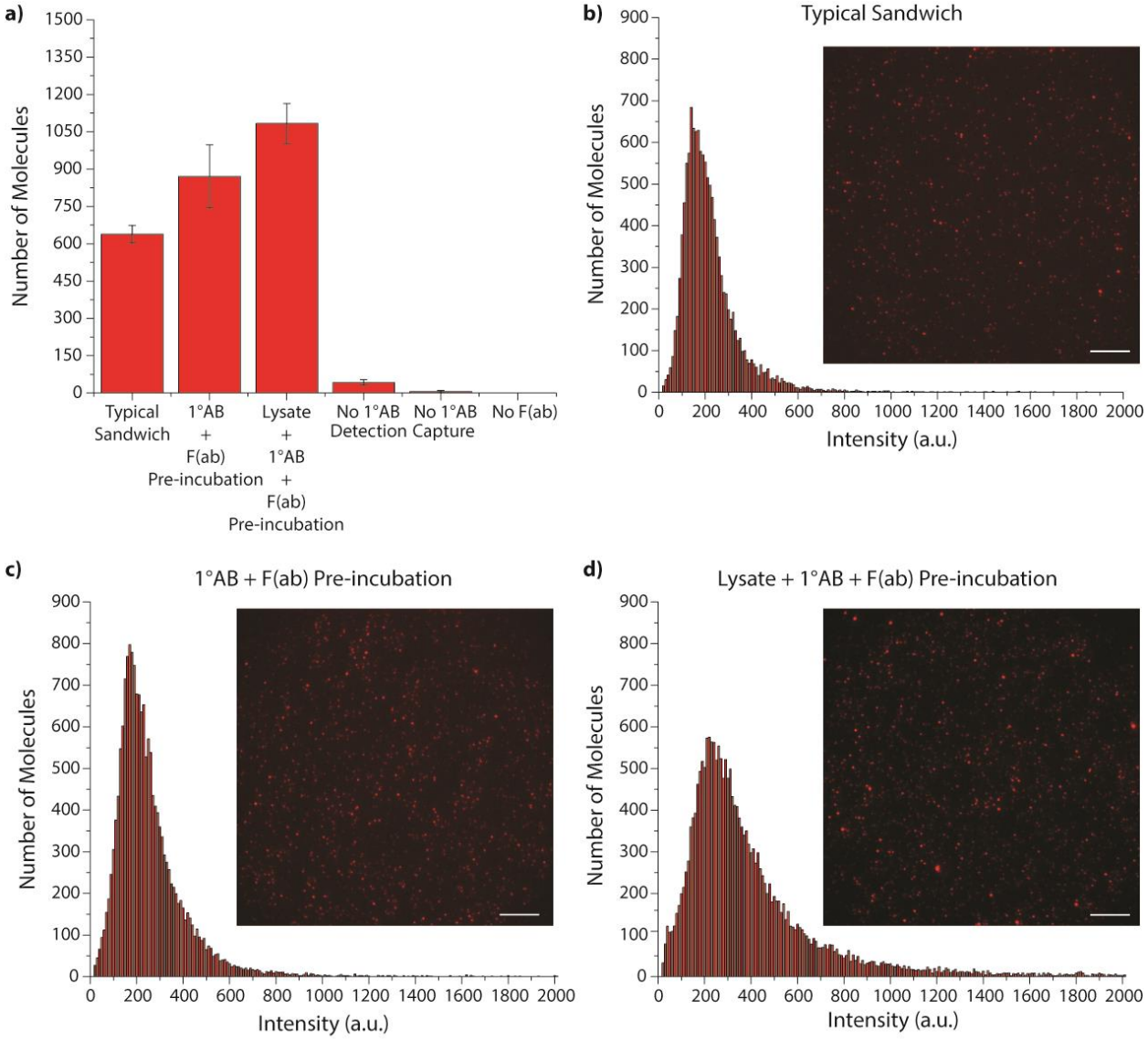

Figure 28. DDS SiMPull using endogenous α-tubulin from crude cell lysates. (a) The average number of detected spots per field-of-view for sequential SiMPull, pre-incubated samples, and nonspecific binding experiments. Error bars show the standard deviation from the mean. Intensity distributions and representative images for (b) DDS sandwich SiMPull, (c) pre-incubation of the primary antibody and *F*(*ab*)-A647, and (d) pre-incubation of lysate, primary antibody, and *F*(*ab*)-A647. Scale bars, 10 μm.

Figure 28a shows that the number of detected spots increased as more components of the assay were pre-incubated. This is somewhat contradictory to the results with recombinant α-tubulin where there was little change in the number of detected spots, and while the difference in

number of molecules was within the range of experiment-to-experiment fluctuations, the trend was consistent across several experiments. Similar to results obtained with recombinant protein, low levels of non-specific binding were maintained, which indicated that DT20 passivation is robust and suitable for use with unpurified samples.

Intensity distributions and images from each SiMPull protocol are shown in Figures 28b-d. The intensity distribution from the sample where the lysate, primary antibody, and F(*ab*)-A647 were all pre-incubated is broadened and contains more high-intensity molecules compared to the intensity distributions obtained by sequential incubation and pre-incubation of only the primary antibody and F(*ab*)-A647, which were comparable. The experiments performed with pre-incubated recombinant α-tubulin in Section 5.2.4 did not cause a notable increase in the number of spots detected at higher intensities. We expect that the difference between the results of recombinant and endogenous protein is due to the stabilization of weakly-interacting proteins, thus maintaining the native stoichiometry of the endogenous protein complexes. For example, it is possible that the endogenous α-tubulin was interacting with β-tubulin in the lysate to form oligomeric protein complexes, which became stabilized by the detection antibodies when they were pre-incubated together in solution. An alternative analysis is through the dynamics of tubulin protofilament formation via the binding and unbinding of tubulin proteins. The tubulin polymerization may be hindered in the flow chamber where the tubulin concentration is lower than that of the lysate, meaning that pre-incubation of the lysate with the antibodies may slow the rate of polymerized tubulin disassociation.

5.3. Conclusion

This chapter has shown that the SiMPull assay can be greatly simplified with the combination of DT20 passivation and the use of F(*ab*) antibody fragments as the secondary detection antibody. The DT20 passivation protocol greatly shortens the sample preparation by reducing the time needed for glass treatment, and by reducing the number of incubation steps required by eliminating the need for linkage molecules such as biotin, Neutravidin, and secondary capture antibodies. The use of monovalent F(*ab*) fragments avoids aggregation issues associated with the incubation of primary and secondary antibodies in solution, which facilitated a two-step SiMPull assay using pre-mixed sample solutions for vastly improved assay throughput. In addition to making the assay more user-friendly, it was observed that pre-incubation of the sample with the detection antibodies and fragments increases the percentage of labelled and detected target molecules. Thus, the method described in this chapter improves the SiMPull assay not only in terms of the ease of conducting the assay, but also improves the sensitivity of the assay.

CHAPTER 6: CONTROLLED FLUORESCENT LABELLING VIA ENGINEERED SECONDARY NANOBODIES

Chapters 3 and 4 demonstrated that the difference in fluorescence intensity of individual fluorophores can be detected if an excitation beam with sufficient uniformity is used in single-molecule studies. The final step to achieving a quantitative intensity-based SiMPull assay is then controlling the fluorescent labeling of the detection antibodies, so that the single-molecule intensity can be correlated to the number of pulled-down proteins. The ideal labeling for the quantitative SiMPull assay would be one fluorophore per detection antibody, so that each captured protein would be labeled one-to-one with a fluorophore and could be counted directly from the measured intensity. However, it is challenging to label antibodies or antibody fragments in a controlled manner, as the most common labeling approaches rely upon non-targeted binding to common reactive residues, for example the binding between N-hydroxysuccinimide (NHS) esters with amine residues on antibodies[104].

Non-specific labeling approaches are appealing due to compatibility with a wide variety of samples, ability to achieve high labeling densities, and straightforward protocols. These uncontrolled labeling approaches yield a distribution of labelled species, commonly measured by the degree of labeling (DoL), which is a molar ratio of the amount of dye to antibody and represents the average number of fluorophores per antibody. Achieving a DoL of one with non-targeted labeling methods will result in most of antibodies having a single fluorophore, but there will also be a significant portion of unlabeled antibodies, as well as populations of antibodies labeled with two or more fluorophores. This is unsuitable for the quantitative SiMPull assay because unlabeled antibodies will not produce signal in the SiMPull assay, thus skewing the intensity distribution

towards low intensity populations and altering the measured stoichiometry of the protein complexes. Similarly, antibodies with more fluorophores will have the same effect but in the opposite direction, shifting the intensity distribution towards higher intensity populations.

While controlled labeling of antibodies is difficult, it is much more readily achieved using oligonucleotide sequences. A variety of chemical and enzymatic methods exist to conjugate fluorophores to either the 3' or 5' end of DNA and RNA samples, which results in a single fluorophore per oligonucleotide strand. For example, 1-Ethyl-3-[3-dimethylaminopropyl] carbodiimide hydrochloride is a common chemical approach that is used to conjugate fluorophores with NHS ester groups to the 5' end of DNA or RNA strands, whereas the use of DNA polymerase is an enzymatic approach to label DNA or RNA at either the 5' or 3' ends or even random points along the oligonucleotide sequence[105]. The labeled oligonucleotide strands can be used as fluorescent probes to complementary oligonucleotide sequences or conjugated to other biomolecules. Conjugation of DNA or RNA to antibodies can be readily achieved, but approaches typical utilize linkage molecules bound via non-targeted labeling approaches similar to direct fluorophore conjugation and thus suffer from the same issues[106] or require extensive purification[107]. Rather than binding oligonucleotides to antibodies, it is possible to use DNA or RNA aptamers in place of antibodies altogether[108]. Aptamers are large oligonucleotide sequences that fold into a geometry that facilitates binding to a target molecule with high affinity. Aptamers can be designed to directly target a protein of interest[109] similar to the primary antibodies used in SiMPull assays, or to bind to antibodies similar to secondary antibodies[110]. Aptamers maintain the ease of controlled labeling of other oligonucleotide sequences and show promise for use in intensity-based single-molecule assays; however, we have not been able to successfully utilize

primary or secondary aptamers in our SiMPull assays. This is potentially due to issues during the aptamer folding process, differences in the structure of the target molecule due to preparation protocols, or competition between components in the SiMPull assay attempting to bind to the same epitope of the target molecule.

Another common approach to achieve controlled labelling is by fusing a fluorescent protein such as those in the GFP family to the target protein via genetic engineering[41, 111]. This method is appealing in that it removes the need for detection antibodies in the SiMPull assay, avoiding complications due to captured but unlabeled proteins, binding ratios of the detection antibodies, etc.; however, it is not suitable for studying native proteins and thus not compatible with our goal of utilizing the SiMPull assay as a diagnostic tool in clinical settings.

In this chapter I will describe our investigation into the use of engineered nanobodies[103] as the secondary detection antibody in our SiMPull assays. Nanobodies are derived from camelids and are similar to F(*ab*) fragments in structure, although they are smaller and essentially only consist of the binding epitope. The nanobodies we employed are specific to the Fc region of rabbit IgG antibodies and were designed such that they have a single cysteine labeling site for a fluorophore through maleimide conjugation[112]. Due to the similarity in structure with F(*ab*) fragments, it is expected that the nanobodies are monovalent and thus could utilize the pre-incubation techniques described in the previous chapter to shorten the SiMPull assay protocol. Ideally, these nanobodies would achieve a quantitative, intensity-based SiMPull assay with a straightforward protocol capable of probing the stoichiometry of protein complexes. This chapter describes studies on the binding characteristics of the nanobodies and their compatibility with SiMPull assays for characterizing the stoichiometry of oligomeric proteins.

6.1. Methods

6.1.1. Nanobody Growth, Purification, and Labeling

Nanobodies were grown roughly according to the protocol published by Pleiner *et. al*[103], and a detailed protocol is provided in Appendix A. In brief, *E. Coli* expressing the Anti-Rabbit 1x Cys nanobody plasmid (104163, Addgene) and NEDD8-specific protease for -His tag cleavage (104131, Addgene) were each grown in 2x-YT medium (ThermoFisher) supplemented with 50 μg/mL kanamycin (Sigma), and overexpression of the nanobody protein and protease was induced by adding 0.2 mM Isopropyl β- d-1-thiogalactopyranoside (Sigma). The reaction was quenched by the addition of 1 mM phenylmethylsulfonyl fluoride (Sigma). The bacteria were pelleted via centrifugation at 1800 g for 20 minutes and the supernatant was discarded.

The bacteria were resuspended and lysed in lysis buffers tailored to each protein before lysis via ultrasonication. The lysed bacteria were centrifuged at 18,000 g, the supernatant was collected, and loaded into nickel-NTA columns (ThermoFisher) for purification. The purified nanobodies and protease proteins were buffer exchanged to a cleavage buffer before mixing to cleave the -His tag from the nanobodies. The cleavage reaction was loaded into nickel-NTA columns and the cleaved nanobodies were washed out before eluting the protease and bound -His tags. The cleaved nanobodies were then buffer exchanged to a maleimide labeling buffer.

The concentration of the cleaved nanobodies was measured using a NanoDrop spectrophotometer and were labeled with a 4-fold molar excess of A647-maleimide dye (ThermoFisher) overnight. Excess dye was removed via two rounds of buffer exchange, and the degree of labeling was measured to be 1.1 using the NanoDrop. Samples from each step of purification were analyzed via a ~12.5% gel using SDS-PAGE.

6.1.2. Single-Molecule Labeling Analysis

All single-molecule experiments were conducted using the refractive beam shaping microscope design detailed in Section 3.1.1 and DT20 passivated flow chambers described in Section 5.1.1. A 491 nm laser was used as an expanded and clipped Gaussian excitation beam (300 mm focal length collimating lens) to excite EGFP samples. For comparison with the nanobodies, IgG antibodies and monovalent F(*ab*) fragments were labeled with A647 at a DoL of 1.1 as described in Section 2.1.3. 40 pM of each sample was diluted in bPBS buffer described in 5.1.2 and adhered directly to a DDS flow chamber by incubation for 10 minutes. The samples were washed out using PBS and the imaging buffer described in each of the previous chapters was added before analyzing in the microscope. The samples were imaged using ~1.5 mW of 638 nm excitation and 20 FOVs were imaged to generate intensity distributions. For comparison with photobleaching analysis, the excitation power was increased to ~5 mW and 60 second timetraces were recorded for analysis.

6.1.3. Characterizing Nanobody Affinity

0.2 μg/mL of primary rabbit antibody diluted in bPBS was adhered to the DDS flow chamber surface before passivation with 0.2% Tween-20 diluted in T50 buffer as described in Section 5.1.2. The flow chambers were then incubated with either 2.5, 5, 10, or 20 nM of the nanobodies labeled with A647 (NB-A647) for 20 minutes. The flow chambers were washed out with PBS and imaging buffer was added before analysis in the microscope. Images from 20 FOVs in each sample were acquired and the average number of detected spots in each was plotted as a

function of the nanobody concentration. The equilibrium dissociation constant of the nanobody was determined by fitting the curve to Equation 6:

$$y = \frac{abx^{1-c}}{1+bx^{1-c}} \quad (6)$$

where a, b, and c are fitting parameters and x is the nanobody concentration. The equilibrium dissociation constant was calculated as where Equation 6 was equal to 0.5*a.

6.1.4. Characterizing Nanobody Valency

~50 pM of primary rabbit antibody used as the detection in the SiMPull assays (ab51252, ab6556; Abcam) were adhered to the DDS flow chamber and labeled with 10 nM NB-A647, as described in the previous section. Images from 20 FOVs were acquired and used to generate intensity distributions. Similar experiments were conducted using the 1.1 DoL F(*ab*) and IgG samples with the anti-α-SYN rabbit antibody for comparison.

6.1.5. Attempts to Remove Secondary Binding Population

Two cases were considered to remove the secondary population in the nanobody intensity distribution: two nanobodies were binding to a single antibody or two antibodies are aggregated together and needed to be separated. In light of the first case, we treated rabbit antibodies with reducing agents in an attempt to cleave them along the disulfide bonds in the Fc hinge region that bind the two heavy chains[113]. IgG molecules split along their two heavy chains will be referred to as reduced IgG (rIgG). It his reported that acidic conditions[114] or a low concentration of ionic detergent[115, 116] can favor the formation of rIgG, so each case was tested. The reducing agents tested were sodium sulfite[115], beta-mercaptoethanol (BME)[115], dithiothritol (DTT)[113], and 2-

mercaptoethylamine (2-MEA)[113, 117]. All chemicals were purchased from Sigma Aldrich. Each reducing reaction was 50 μL in volume and consisted of 0.1 mg/mL rabbit antibody, 1 mM athylenediaminetetraacetic acid, 100 mM sodium chloride, 10 mM 5,5′-dithiobis-(2-nitrobenzoic acid), and the reducing agent. All reactions were performed in PBS except in the case of sodium sulfite where 25 mM Tris buffer was used instead. For reactions performed in acid conditions the buffer was adjusted to a pH of 4.0, and reactions performed with the addition of detergent included 0.1% SDS. After mixing, samples were heated at 37°C for 90 minutes after which the reaction was quenched on ice. The reactions were analyzed using SDS-PAGE where ~20 μL of the reaction was used per well.

Conversely, considering that the secondary population in the nanobody intensity distribution was caused by antibody aggregation, size exclusion chromatography was performed. A HiLoad Superdex 16/600 200 pg column was used with an Ätka Start Cytiva Protein Purification System. A buffer consisting of 150 mM disodium phosphate and 4 mM potassium chloride was adjusted to a pH of 7.6 and passed through a 0.22 μm filter. The column was equilibrated with 2 column volumes of buffer before injecting the antibody samples. Rabbit IgG antibodies were diluted to concentrations of 100 μg/mL or 50 μg/mL in PBS buffer before ~300 uL of the antibody sample was injected to the column and ran at a flow rate of 0.5 mL/min for a total run volume of 250 mL. 9 mL fractions were collected, and fractions of interest were analyzed via SDS-PAGE and single-molecule experiments as described in Section 6.1.4.

6.1.6. Nanobody SiMPull

The nanobody SiMPull assay was performed using DT20 passivation similar to experiments described in Section 5.1.2. Primary antibodies used in SiMPull assays with α-SYN, the rabbit (610787, BD BioSciences; ab51252, Abcam) and for GFP-related proteins (ab1213, ab6556; Abcam) were selected based on affinity and minimized non-specific binding and crosstalk. Note that the GFP antibody pair used here alleviated issues related to antibody-based detection of GFP seen in Chapter 5. In short, 10 μg/mL primary mouse antibody was adhered to the DDS surface, the flow chamber was passivated with 0.2% Tween-20, then the protein of interest, 1 μg/mL primary rabbit, and 10 nM NB-A647 were sequentially incubated for 20 minutes each, washing with PBS between each step. All samples were diluted in bPBS. Note that for α-SYN the primary mouse antibody was diluted to a concentration of 5 μg/mL. Recombinant α-SYN SiMPull assays were conducted using the 1.1 DoL F(*ab*)-A647 and IgG-A647 samples as a comparison with the NB-A647 experiments. Images from 20 different FOVs were acquired to generate intensity distributions.

6.1.7. Preparation of Oligomeric Proteins for Nanobody SiMPull

U2OS cells were grown in McCoy's 5A medium supplemented with 10% fetal bovine serum to a confluency of ~50% before transient expression of a 2x-EGFP plasmid (122489, Addgene) using a lipofectamine treatment (Lipofectamine 3000, ThermoFisher). Cells were grown to a final confluency of ~80% before lysis via incubation in a buffer containing 25 mM Tris-Cl (pH 7.5), 150 mM NaCl, 1 mM EDTA, 1 mM EGTA, 1% NP40, 1% sodium deoxycholate, and 0.1% SDS supplemented with protease inhibitor cocktail (Sigma) on ice for 15 min, as described

in Section 2.1.6. The lysate was centrifuged at 16,000 g for 15 minutes at 4°C and the supernatant was collected for use in SiMPull assays. The overall protein concentration was measured using the NanoDrop spectrophotometer. The lysate was diluted ~3000-fold for use in the SiMPull assays.

Recombinant α-SYN protein was aggregated as described in Section 2.1.4. The aggregated sample was diluted to an appropriate spot density in the SiMPull assay and examined at several timepoints after initial incubation in the heated shaker.

6.2. Results

6.2.1. Characterizing the Anti-Rabbit Nanobody Labeling

After the nanobodies were purified and labeled with A647, samples from various stages of the purification process and the final labeled nanobodies were characterized using SDS-PAGE. An image of the gel is shown in Figure 29, where well-defined bands are observed at the expected molecular weights, indicating the nanobodies were successfully isolated and labeled.

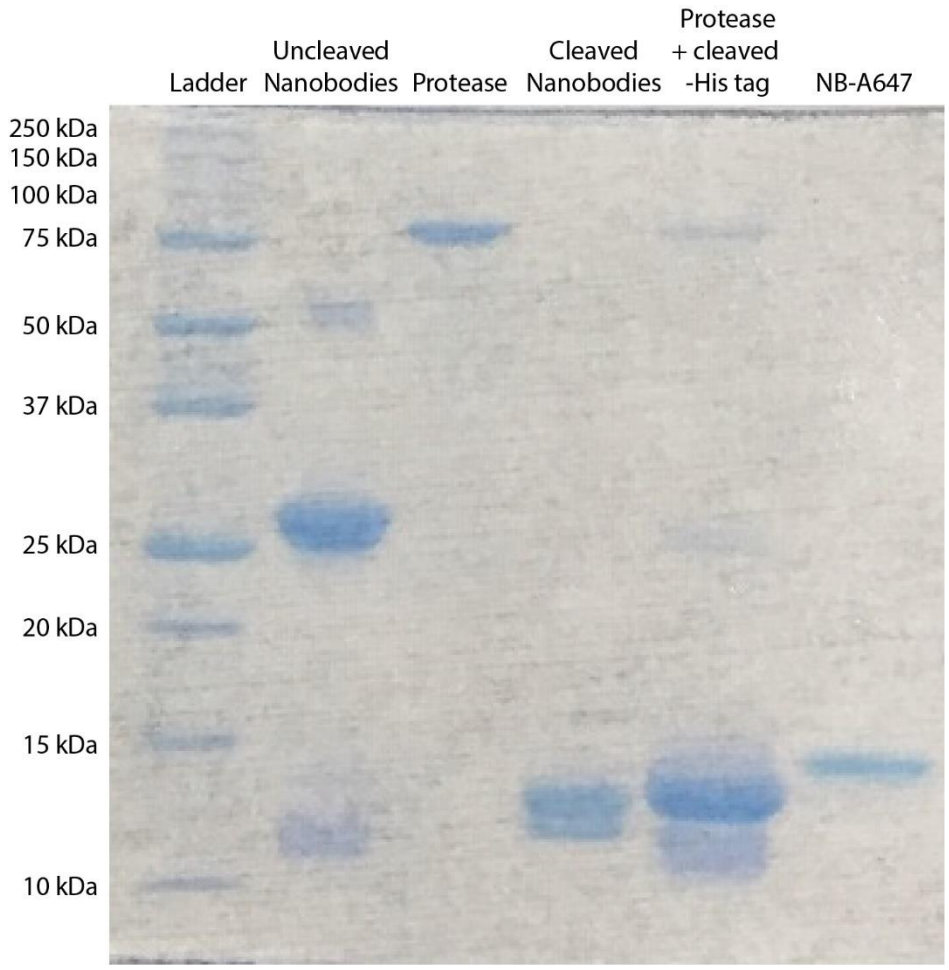

Figure 29. SDS-PAGE result from the purification and labeling of the anti-rabbit nanobodies.

Next, the fluorescence intensity of the NB-A647, F(*ab*), and IgG samples labeled at a DoL of 1.1 were compared using single-molecule imaging. Figure 30 shows a comparison between the intensity distributions and observed photobleaching steps for each sample. It is clear that while the samples have the same DoL, the observed fluorescence is markedly different. The controlled labeling of the nanobody sample results in a single, well-defined peak in the intensity distribution, which is supported by the photobleaching steps where 97% of the nanobodies bleached in a single step. Conversely, the non-targeted labeling of the F(*ab*) and IgG samples result in secondary and small tertiary peaks in the intensity distributions, which are again supported by the photobleaching

analysis. The peaks in the intensity distributions were fit to Gaussian curves, and the relative size of each peak agreed within 5% of the percentage of photobleaching steps for each sample. These results indicate that the nanobodies were successfully labeled with a single fluorophore, and that direct measurement of the fluorescence intensity yielded the same information as photobleaching analysis but in a fraction of the observation time.

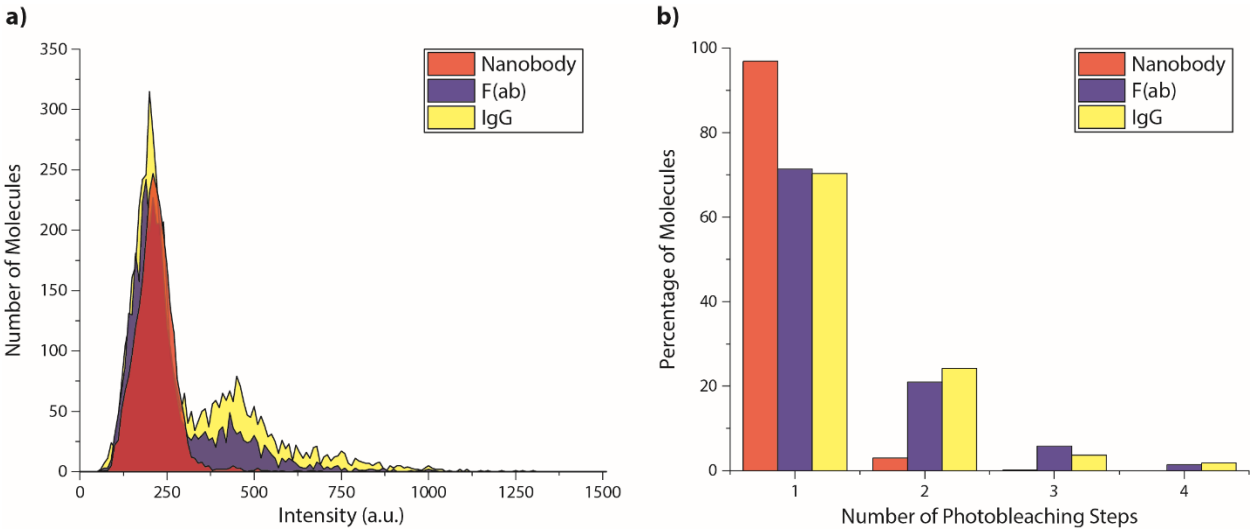

Figure 30. Single-molecule intensity analysis of nanobody, F(*ab*), and IgG samples. Comparisons between the (a) intensity distributions and (b) photobleaching steps are presented for each sample.

6.2.2. Analysis of Anti-Rabbit Nanobody Binding

Next, the binding affinity of the nanobodies was characterized to determine what concentration should be used in the SiMPull assay. Rabbit antibodies were adhered to a DDS surface at a single-molecule density and labeled with various concentrations of NB-A647. Figure 31 shows a plot of the average number of observed single-molecule spots as a function of the nanobody concentration and fit to Equation 6. The result of the fit was used to calculate the equilibrium dissociation constant to be 4.79 nM, so a concentration of 10 nM NB-A647 was used

in all subsequent experiments to ensure proper labeling of the single-molecule samples while avoiding excess nonspecific binding.

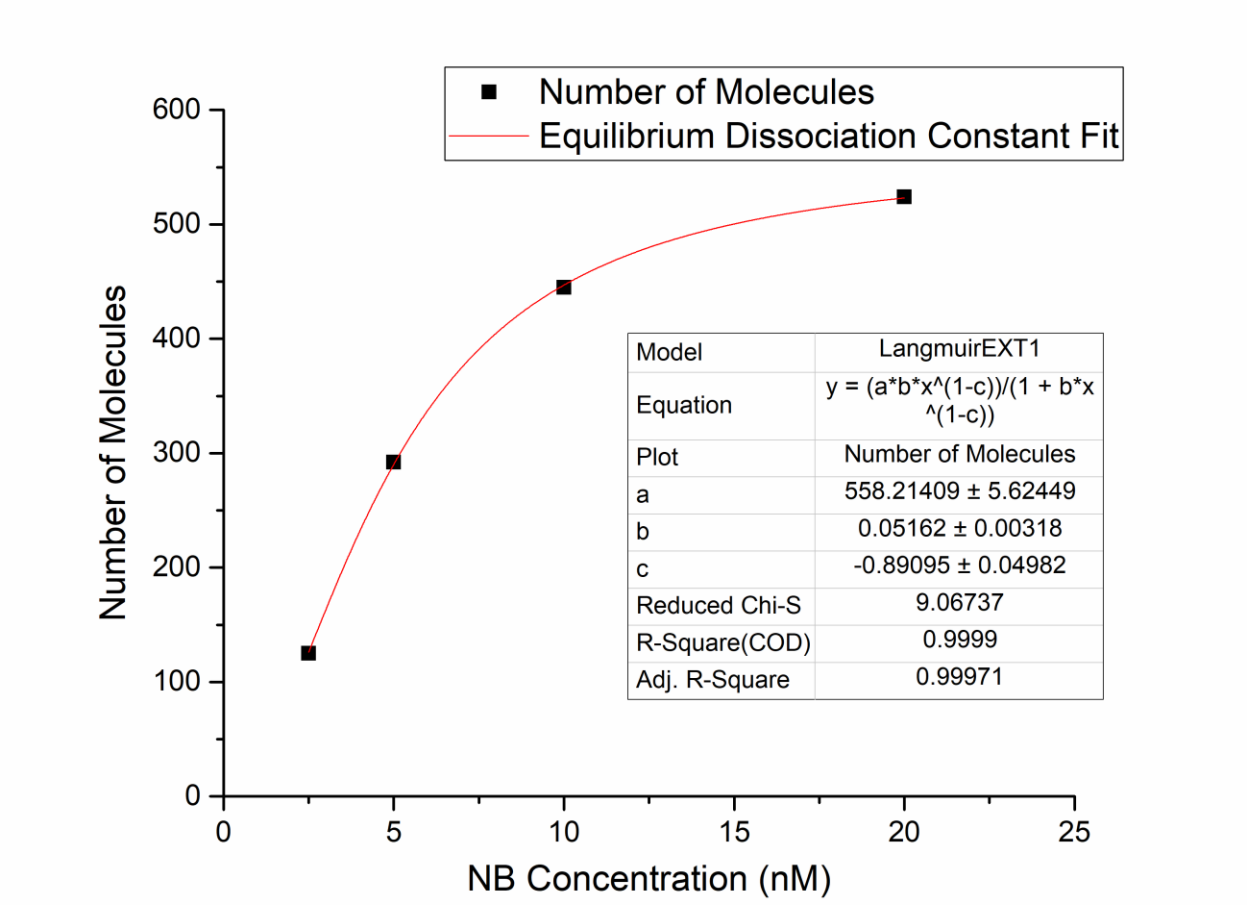

Figure 31. Calculating the nanobody equilibrium dissociation constant. The number of observed single-molecules (black squares) was plotted against the NB-A647 concentration and fit (red line).

Next, the binding of the nanobodies was compared to that of the F(*ab*) and IgG samples with the same DoL. Again, a single-molecule density of primary anti-α-SYN rabbit antibody was adhered to the DDS flow chamber and labeled with either NB-A647, F(*ab*)-A647, or IgG-A647. Intensity distributions were generated for each sample and are compared in Figure 32.

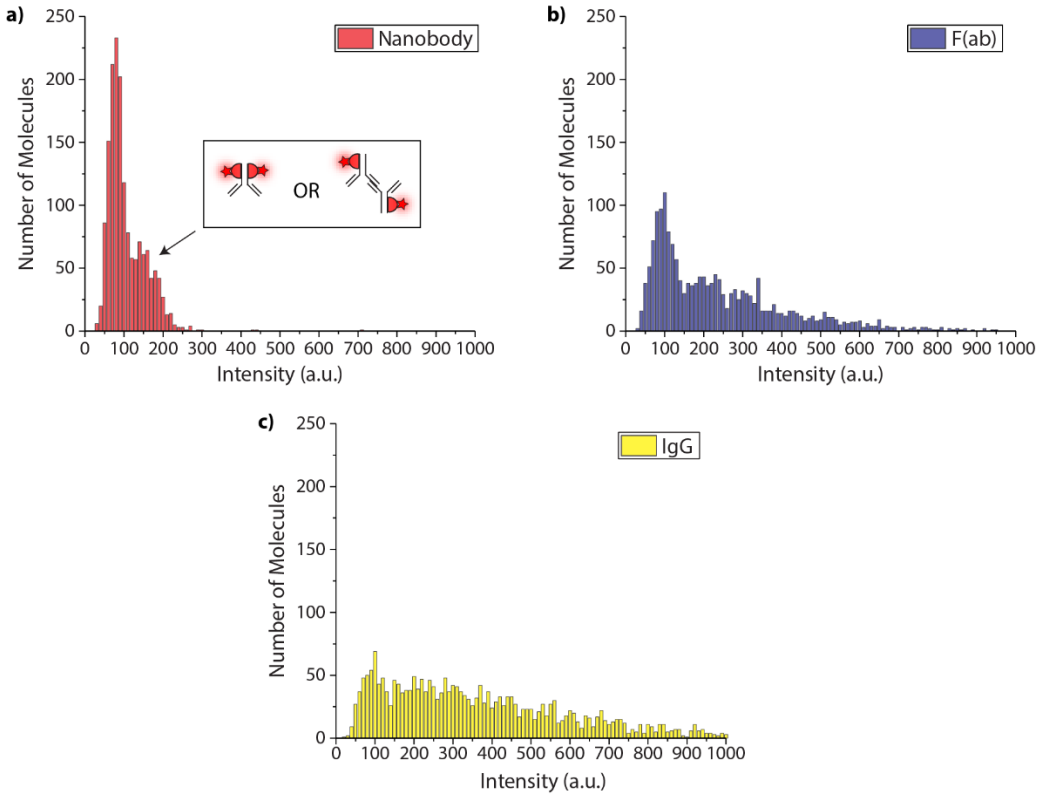

Figure 32. Valency comparison. Intensity distributions for (a) NB-A647, (b) F(*ab*)-A647, and (c) IgG-A647 with the same degree of labeling bound to primary rabbit antibody.

Similar single-molecule spot densities were achieved with each sample, but Figure 32b and 32c show that the intensity distributions for the F(*ab*) and IgG samples are extended out to significantly higher intensities than that of the nanobody distribution presented in Figure 32a. However, there is a clear secondary population in the nanobody intensity distribution at roughly twice that of the primary peak that was not present in the distribution shown in Figure 30 where the nanobodies were adhered directly to the DDS coverslip. The boxed inset in Figure 32a shows the two interpretations for the secondary population, where it could be caused by two nanobodies binding to a single antibody or by the aggregation of the primary antibody where one nanobody is bound to each antibody. Similar secondary populations were observed with the primary anti-GFP rabbit antibodies, where the size of the secondary population was roughly 25-50% of that of the

primary peak in day-to-day fluctuations. This was an undesirable result, as we were aiming to achieve direct one-to-one labeling of detection antibodies and thus the target protein with the nanobodies labelled with a single fluorophore.

6.2.3. Attempts to Suppress the Secondary Population

Considering the two cases presented in the boxed inset of Figure 32a, we first attempted to cleave antibodies and separate them into rIgG which consist of a single heavy and light chain. The idea was that the Fc-specific nanobodies may be able to bind to each of the heavy chains in the Fc region of a full IgG molecule, so the secondary population may be suppressed if rIgG were used instead of full primary IgG molecules. Rabbit antibodies were incubated with reducing agents (sodium sulfite, BME, DTT, and 2-MEA) under acidic conditions or with the addition of mild ionic detergent to facilitate cleavage along the heavy chain backbone. The concentration of the reducing agent was varied over a roughly two order of magnitude range, and the samples were analyzed via SDS-PAGE. For the sake of space, the gel results are not presented, but none of the reducing conditions preferentially generated rIgG molecules. Each reaction resulted in a mixture of uncleaved IgG, some rIgG, and fully separated heavy and light chains. The relative amounts of each depended on the reaction conditions, but we were unable to preferentially form the desired rIgG.

Size exclusion chromatography was performed on rabbit antibodies in consideration to the second case presented in Figure 32a, where a single nanobody binds to each antibody but the rabbit antibodies are aggregated into dimers. Here, the goal was to isolate purely monomeric rabbit antibodies and use them with the nanobodies to achieve one-to-one binding. The results of two

size exclusion separations of rabbit antibodies are shown in Figure 33, where 100 and 50 μg/mL rabbit antibody samples were run through the column and the UV absorbance was used to measure the elution of the antibodies from the column. Both samples resulted in a clear spike at the same point in the absorption timetrace, where the height of the spike in the 100 μg/mL sample was twice that of the 50 μg/mL sample. Elution fractions containing the spike as well as fractions adjacent to the spike were collected for analysis via SDS-PAGE and single-molecule imaging. SDS-PAGE results did not show a population of aggregated antibodies in any fraction. Intensity distributions from each fraction where spots were observed in single-molecule imaging all had a secondary population. These results were somewhat inconclusive. It was not clear if aggregated, dimeric antibodies were collected in the same fraction as the main spike, as this population could have been too low a concentration to be visible after staining the results from SDS-PAGE. Alternatively, it is possible that the antibodies show no aggregation and two nanobodies are capable of binding to each antibody. Further analysis is needed to clarify this behavior, which is discussed in the following chapter.

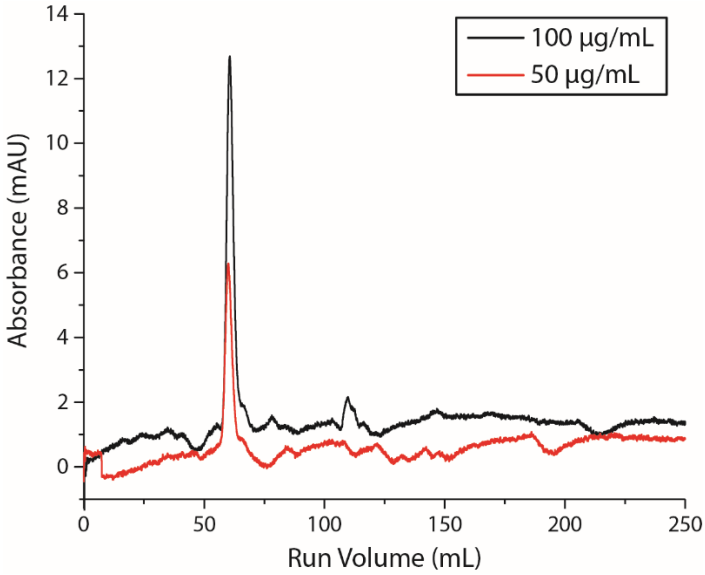

Figure 33. Size exclusion chromatography absorbance timetraces of two rabbit antibody samples of 100 and 50 µg/mL concentration.

6.2.4. Comparing Nanobody SiMPull

After being unable to remove the secondary binding population in nanobody intensity distributions, we moved forward with SiMPull experiments with the intention of numerically calculating the size of monomeric and oligomeric populations similar to the results in Sections 2.2.3 and 2.2.4. SiMPull assays using recombinant α-SYN protein were performed using the NB-A647, F(*ab*)-A647, and IgG-A647 samples labeled at a DoL of 1.1 for comparison. Intensity distributions were generated from each sample and are presented in Figure 34, where results similar to those of the valency comparison in Figure 32 are apparent. The nanobody intensity distribution shows two well defined peaks, whereas the F(*ab*) and IgG distributions are extended out to much higher intensities. The similarity between the nanobody SiMPull result and the valency distribution is indicative that the recombinant α-SYN protein was primarily monomeric, and

demonstrates the benefits of controlled labeling in intensity-based analysis compared to the F(*ab*) and IgG samples where the intensity distributions are less well-defined.

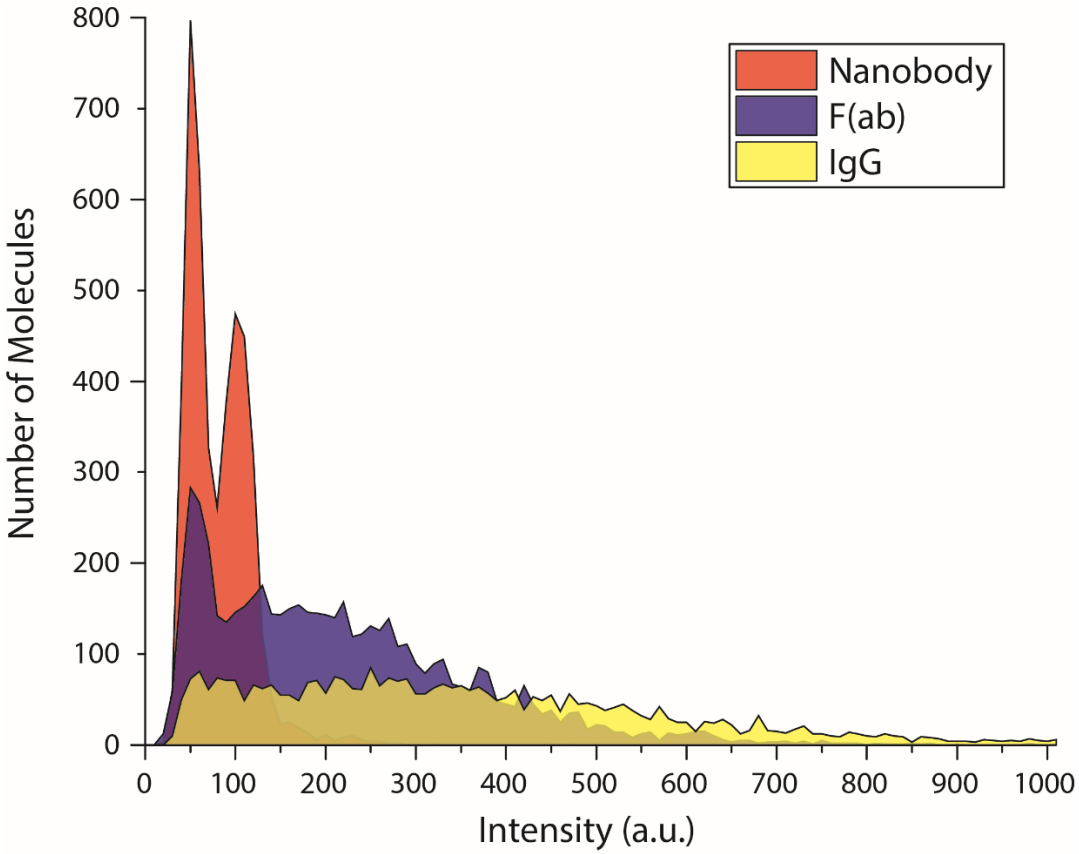

Figure 34. SiMPull comparison. Intensity distributions from SiMPull performed using 5 nM recombinant α-SYN comparing the fluorescent intensity from nanobodies, F(*ab*), and IgG at the same degree of labeling.

6.2.5. Nanobody SiMPull Assays Using Oligomeric Protein

To test if the nanobody SiMPull assay could be used to analyze the stoichiometry of oligomeric protein complexes, we first tested the assay using α-SYN that was heated and shaken to induce aggregation and filamentation. The α-SYN sample was analyzed using the nanobody SiMPull assay at various timepoints to test if multimeric populations developed in the intensity distribution, and after 45 days of incubation the sample had undergone nearly complete

filamentation where minimal amounts of single-molecule α-SYN was observed. Representative intensity distributions and images obtained over the first 30 days of incubation are presented in Figure 35. The intensity distributions shown in Figure 35a show that there is a shift in the relative size of the peaks in the distribution leading up to 3 days of aggregation, when the first filaments were observed as seen by the large, bright spots in the corresponding image in Figure 35b. There are also some smaller bright spots in the day 3 image, which may be protofilaments that seed the growth of larger filaments. After the third day of aggregation, the relative number of filaments observed continuously increased; however, the relative size of the peaks in the intensity distributions returned to a similar ratio observed in the unaggregated sample and no higher order oligomeric populations were observed. This may indicate that the filamentation process begins with small, potentially dimeric seeds evidenced by the shift in the day 3 intensity distribution, which then rapidly form filaments without forming stoichiometric protein complexes. However, these results were unclear, so we investigated other samples to clarify if this was an issue with the SiMPull assay being unable to capture oligomeric proteins. Note that the 30 day image in Figure 35b was captured using camera settings optimized for the fibrils rather than single-molecules, as in the other images, so single-molecule spots are less visible.

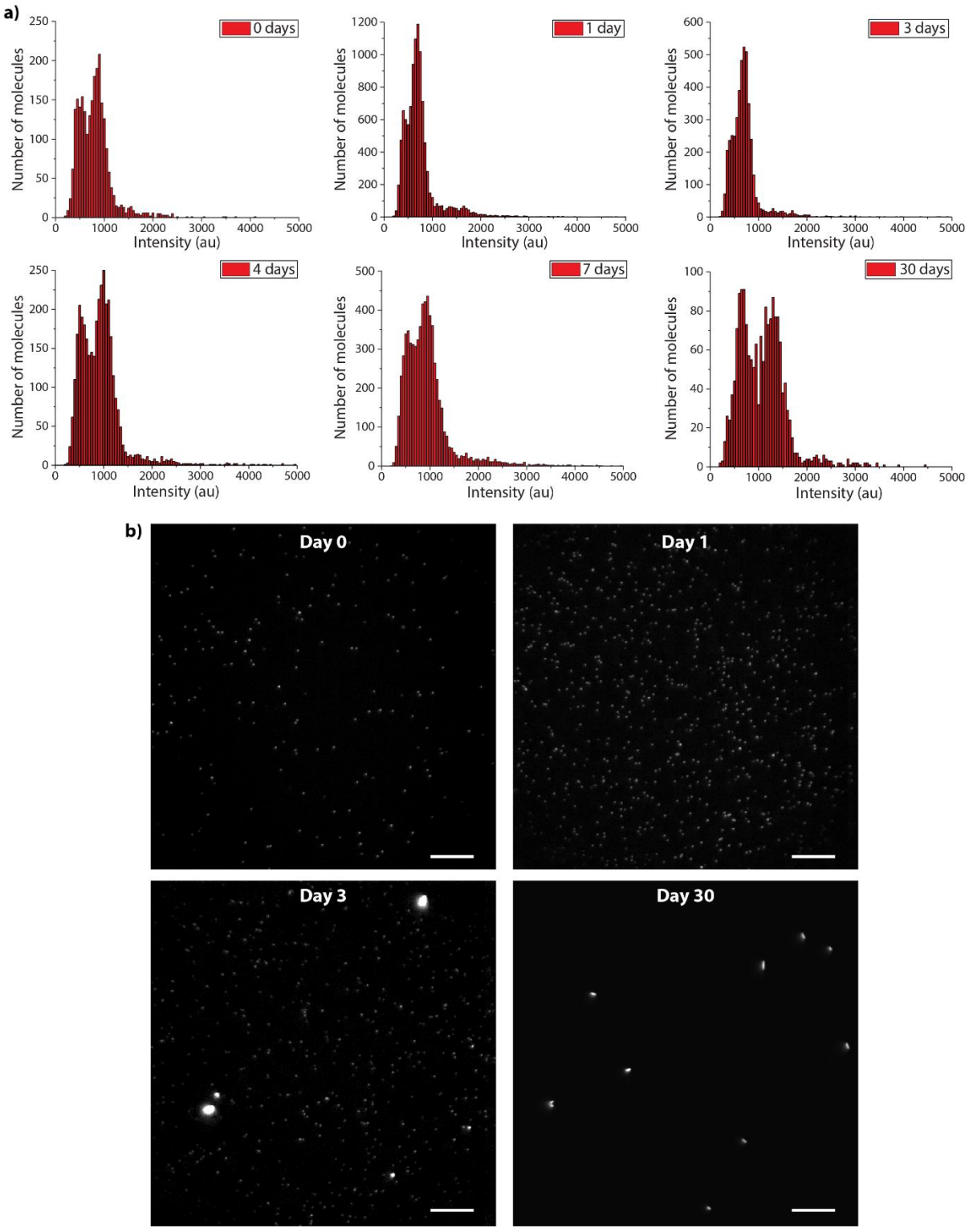

Figure 35. Nanobody SiMPull analysis of aggregated α-SYN. (a) Intensity distributions from samples after various aggregation times. (b) Corresponding images from selected timepoints presented in a). Scalebars 10 μm.

The next sample investigated using the nanobody SiMPull assay was a 2x-EGFP dimeric protein complex, which is two individual EGFP molecules covalently bound to one another. These were transiently expressed in mammalian cells, and the crude cell lysate was used in the SiMPull assay. The results from the nanobody SiMPull assays using the 2x-EGFP samples were compared with standard EGFP, and intensity distributions from each are presented in Figure 36.

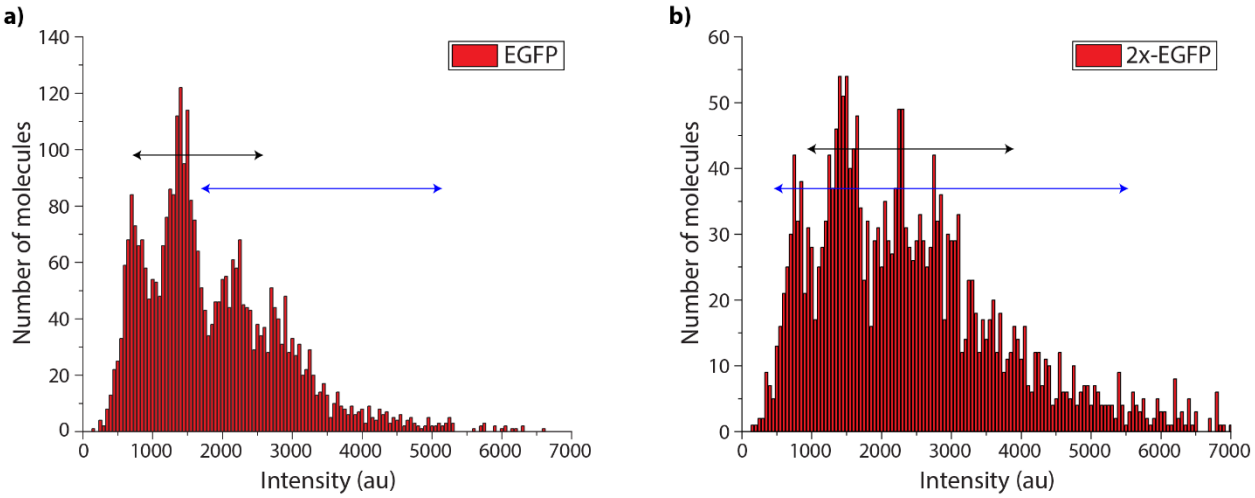

Figure 36. Monomeric and dimeric EGFP intensity analysis. Intensity distributions from nanobody SiMPull assays using (a) EGFP and (b) 2x- EGFP protein samples from crude cell lysates. Intensity regions associated with single GFP photobleaching are denoted with black arrows and two-step photobleaching with blue arrows.

The intensity distribution from the EGFP protein sample shown in Figure 36a has a well-defined third, and somewhat defined fourth peak. This was somewhat unexpected, but EGFP has been known to self-dimerize to some extent, which could explain these features. For example, in the EGFP analysis in Figure 25d of Section 5.2.2 roughly 10% of the EGFP molecules showed two-step photobleaching, consistent with results observed with yellow fluorescent protein[41]. However, the relative size of the third and fourth peaks in the distribution are larger than 10%, which indicates the possibility of the divalent capture antibodies pulling down two EGFP molecules. This has not been observed in any previous SiMPull assays, which could be related to

the size of the target proteins, relative positions of the binding epitope, and less sensitive intensity analysis. Figure 36b shows a broadening out towards higher intensities and a relative increase of the size of the higher intensity populations compared to the EGFP distribution. This indicates that there is a difference in the detected single-molecule fluorescence intensity, although it is not as pronounced as expected. We performed analysis with modified MATLAB codes to correlate the detected NB-A647 fluorescence intensity with the number of detected photobleaching steps of the EGFP and 2x-EGFP molecules. In the EGFP samples, there was a reasonable offset in the NB-A647 intensity of EGFP molecules that photobleached with one or two steps, which are respectively denoted by black and blue double-ended arrows in Figure 36, where the arrows mark the average ± the standard deviation of the NB-A647 intensity. However, the 2x-EGFP showed a very large variation in the NB-A647 fluorescence intensity for single-molecule spots where two step GFP photobleaching was observed, such that the NB-A647 intensity range for 2-step photobleaching covered the entire region for 1-step photobleaching and extended to higher and lower intensities. This can potentially be explained by unexpected photophysics, such as the fact that roughly only 75% of GFP molecules produce fluorescence[118], and there may be unexpected effects similar to the intersystem crossing observed in FRET experiments when fluorophores are brought in close proximity to one another due to the covalent linkage of the 2x-EGFP molecules. Again, these results were inconclusive and did not yield definitive stoichiometric analysis.

Alternative samples such as α-SYN protein produced by cell lines that recreate biologically relevant stress conditions that favor α-SYN aggregation, or cell lines that were chemically treated to induce aggregation were also tested. Unfortunately, no significant difference was observed in the intensity distributions compared to recombinant protein, and Western Blot analysis was

inconclusive. Additionally, nanobody SiMPull assays with all the samples discussed in this section were performed with pre-incubated detection antibodies and nanobodies, as well as pre-incubated protein, detection antibody, and nanobodies; however, this was not found to show an oligomeric species in any of the intensity distributions. For the sake of brevity, these results have been omitted from this report.

6.3. Conclusion

This chapter demonstrated that controlled fluorescent labeling of engineered antibodies or antibody substitutes, in this case secondary nanobodies, can yield more quantitative intensity information for protein analysis. Unfortunately, we were unable to successfully apply these nanobodies to an intensity-based SiMPull assay to determine the stoichiometry of protein complexes. This was partly due to uncertainties in the binding of the nanobodies to the primary rabbit antibodies, where it was unclear if two nanobodies were bound to a single antibody or if aggregation of the antibodies was the cause for a secondary population in the measured intensity distributions. This secondary population hindered quantitative intensity analysis. It was also unclear if the protein samples used for oligomeric analysis were appropriate for the quantitative SiMPull assay. However, the nanobody-based assay did provide insight into potential pitfalls of the current SiMPull assay, and possible methods to mitigate these issues are described in the following chapter.

CHAPTER 7: OUTLOOK AND FUTURE STUDIES

7.1. Improvements to the Nanobody-Based SiMPull Assay

We were unable to ascertain if two nanobodies were bound to the Fc region of each primary rabbit IgG antibody in the previous chapter. The Fc region is made up of two heavy chains linked by disulfide bonds, and as such it is likely that the two chains are similar in structure and may each contain the epitope to which the nanobodies bind. Additionally, the intensity distribution for the EGFP samples presented in Figure 36 indicated that there may be two target proteins captured by the primary mouse antibody. This is reasonable to expect due to the divalent nature of the antibody, although it had not been observed previously in our SiMPull studies, likely due to the less quantitative nature of the intensity analysis. It is possible that both issues discussed above could be mitigated by the use of F(*ab*) fragments in place of the primary capture and detection antibodies, and nanobodies that target the F(*ab*) region of IgG antibodies[103].

The F(*ab*) domain consists of a single heavy chain and light chain, meaning that it is less likely to have multiple binding domains for the nanobodies specific to this region of an IgG molecule. If the secondary population in the nanobody intensity distributions was caused due to one nanobody binding to each of the heavy chains that make up the Fc region, the use of F(*ab*) fragments would likely prevent this and achieve one-to-one binding of nanobody to F(*ab*). Meanwhile, if aggregation of the primary antibodies was the cause of the secondary population, the use of F(*ab*) fragments is likely to mitigate this effect as well. Both the Fc region and F(*ab*) region of IgG antibodies are implicated as potential sites that enable the aggregation of IgG molecules[119], so the separation of F(*ab*) fragments from the Fc region may hinder the process of aggregation. Additionally, F(*ab*) fragments are readily prepared via papain digestion[120], which is

a more widely-studied protocol than the preparation of rIgG fragments attempted in the previous chapter. However, the affinity of F(*ab*) fragments to the target protein may be more sensitive to effects from a bound nanobody than with Fc-specific nanobodies, as the increased proximity of the nanobody to the binding site may induce steric hinderance or conformational changes to the F(*ab*) fragment that hinder binding to the target protein. Additionally, each F(*ab*) fragment produced would need to be thoroughly characterized in terms of nonspecific binding, crosstalk with other components of the assay, and potential for aggregation after production and purification. However, the monovalent nature of F(*ab*) fragments would alleviate any potential issues of a single capture antibody immobilizing multiple proteins, and would likely ensure one-to-one binding of protein, antibody, and nanobody.

7.2. Label-free SiMPull Assay with Structural Information

Thus far, this report has focused solely on fluorescence-based single-molecule techniques and assays. While fluorescence microscopy has a number of strengths and offers exceptional signal contrast, there are disadvantages to using fluorescent labels. The fluorescent tags are often on a similar scale to the size of the proteins of interest, and fluorescent labeling can perturb the native behavior of the protein or biomolecule that it is attached to[121]. As such, label-free techniques are highly desirable in that the true native dynamics, kinetics, and interactions of the target biomolecule can be observed.

One particularly powerful approach is to measure the amount of light scattered by individual biomolecules. When this type of microscope is operated in transmission mode it is referred to as coherent brightfield microscopy (COBRI)[122] whereas reflection mode is referred to

as interferometric scattering microscopy (iSCAT)[123]. Both of these operate under the same principles such that the signal is detected in a common-path interferometer setup, where in COBRI or iSCAT the reference signal is the either the transmitted or reflected light, respectively. The common-path interferometer setup inherent to this microscope configuration provides the stability required to detect the miniscule scattered signal from the individual biomolecules. The signal takes the form of a basic interferometer:

$$I_{det} = |E_i|^2\{r^2 + |s|^2 - 2r|s| \sin \varphi\} \quad (7)$$

which can be simplified because the pure scattering term is substantially smaller than any other term and rewritten as the signal-to-background ratio:

$$\frac{I_{particle}}{I_{background}} = 1 - \frac{2r|s| \sin \varphi}{r^2} \quad (8)$$

where I_{det} is the detected intensity, E_i is the incident field, r is the reference strength (either reflectivity at the glass/water interface or transmittivity of the sample), s is the scattering contribution, and φ is the phase difference between the reference and scattered fields. The sinusoidal phase dependence makes these techniques exceptionally sensitive along the optical axis especially when operated in reflection mode, where iSCAT can provide nanometer axial precision[124].

In order to detect the extremely weak scattered signal from single-molecules, it is necessary to remove the sample background computationally to achieve as close to shot-noise limited signal as possible. The background removal is typically done in several stages[125], the first being done by recording an exposure while translating the sample. This records an averaged image of the illumination beam, which is then divided out from the image to reveal the coverslip roughness. At this point another exposure is recorded while the sample is stationary to capture the sample

roughness, which is then divided out from the image to yield a flat, essentially background-free image. At this point the sample can be introduced and the scattered signal from individual biomolecules can be visualized. To further improve the signal contrast, the reflected or transmitted reference field can be attenuated via numerical-aperture shaping[126]. This technique exploits the fact that light scattered from the sample enters the objective preferentially at large angles, whereas the illumination light is confined to smaller angles and thus the center of the objective and back focal plane. A partially reflective mirror is inserted into the detection path, where the center of the mirror diverts the reference beam while the rest of the mirror is uncoated and passes the scattered signal. This technique can reduce the background signal to the point that the coverslip roughness can be visualized without any image processing.

An interesting application of scattering microscopy is as a nondestructive alternative to mass spectrometry. This was originally referred to as interferometric scattering mass spectrometry (iSCAMS)[127] but is now referred to as mass photometry[128]. In mass photometry, iSCAT is exploited for the fact that the signal scales linearly with the molecular weight of the biomolecule, with a sensitivity of roughly 19 kDa and precision of 1 kDa. In this way, biomolecules can be identified if there is prior knowledge about the sample, but a more powerful application is that the stoichiometry of oligomeric complexes can be directly probed[127]. This is essentially a nonspecific but label-free method to probe the stoichiometry information we are interested in with the quantitative intensity-based SiMPull assay. However, iSCAT and thus mass photometry has been made specific in past literature by coating the coverslip with antibodies to detect carcinoembryonic antigen[125], which occurs in very low levels in adult blood where elevated levels may be an indicator of certain types of cancer. This technique offers the specificity and sensitivity to probe the mass

of the protein complexes in a way that would achieve the goal of utilizing the quantitative intensity-based SiMPull assay for diagnostic purposes, at the expense of a less user-friendly experimental setup and imaging procedure. While the ability to directly probe the mass and thus the stoichiometry of a protein complex or other biomolecule offers great promise as a clinical tool, it may be possible to improve the mass photometry technique to also probe the overall protein structure. Protein structure can be more relevant than mass or stoichiometry in disease pathology, as protein misfolding is often highly correlated with the onset or progression of a disease[129-131].

A common method of probing the secondary and tertiary structure of proteins and biomolecules is via circular dichroism spectroscopy (CD)[132]. CD probes this information via the chiral response of biomolecules to left and right-handed circularly polarized light (LCP, RCP), and the CD response of biomolecules is strongest in the ultraviolet (UV) spectrum. Through Beer's law the difference in the absorption of LCP and RCP light can be converted to the molar ellipticity or molar circular dichroism, which are the common forms for reporting the CD response of a sample. Proteins exhibit a CD response at far-UV wavelengths between 190-280 nm that yields information about their secondary structure, which describes the folding of the protein as an α-helix, β-sheet, or random coil configuration[133]. Proteins also have a CD response in the near-UV at wavelengths of 250-320 nm that is sensitive to the tertiary structure of the proteins, which describes the overall 3D shape of the protein[133]. CD is mostly used as an ensemble technique, but it has been applied at the single-molecule level[134] and even combined with smFRET microscopy[135].

As such, there is promise that it is possible to probe the mass, stoichiometry, and structural information of protein complexes by combining mass photometry and single-molecule CD

spectroscopy. To perform these experiments, a supercontinuum source could be used to sweep the illumination wavelength to probe the CD response over the portion of the UV spectrum relevant to CD spectroscopy for protein complexes. To generate LCP and RCP while tuning the wavelength, a linear polarizer could be combined with a photoelastic modulator which functions as a tunable waveplate and is common to CD spectroscopy. However, a potential issue is that the CD response of biomolecules occurs in the UV region, where the quantum efficiency of EMCCD cameras commonly used for single-molecule imaging falls to roughly 10%. However, alternative detectors specially designed for UV detection may make these studies possible, such as the BU2 CCD sensor from Andor, which achieves a quantum efficiency of roughly 60% in the 200 – 350 nm spectral region and is compatible with their iDus 420 camera.

CHAPTER 8: CONCLUSION

This dissertation has outlined the strengths and versatility of fluorescence microscopy and its widespread applications. Single-molecule fluorescence microscopy techniques have unique advantages over more traditional bulk assays, which stem from their gentle sample treatments and highly sensitive detection methods. This combination enables the target biomolecule to be studied in its native state, and previously inaccessible features to be probed by analyzing the sample molecule by molecule. In this report, I detailed my work within the field of fluorescence microscopy, which focuses on developing new single-molecule techniques.

The bulk of my research focused on making the SiMPull assay more quantitative. I have demonstrated that refractive beam shaping can be used to generate uniform excitation beams from laser sources that are compatible with traditional microscope bodies and objective TIRF. Additionally, I demonstrated that incoherent sources can be used with an annular fiber bundle that reshapes the beam to achieve artifact-free TIRF imaging with a uniform excitation profile. Both methods of beam shaping achieved the key metric of distinguishing the difference in intensity of individual fluorophores, which enabled quantitative intensity-based analysis of single-molecule samples. However, tradeoffs exist between both techniques in that the refractive beam shaping approach requires a specific input beam profile and is designed for use with a certain spectral bandwidth, whereas the fiber bundle is designed custom to a certain imaging objective.

Additionally, I demonstrated a method to reduce the sample preparation time for SiMPull assays through an alternative passivation protocol and the use of monovalent antibody fragments. In addition to making the assay more user-friendly, this approach also made the assay more sensitive due to the ability to pre-incubate multiple components of the assay, which significantly

increased the colocalization observed in multicolor SiMPull assays. As such, this work makes the SiMPull assay more appealing in its simplicity and effectiveness.

My work using engineered nanobodies was also able to utilize pre-incubation to shorten the SiMPull assay protocol; however, the main appeal of this research was the ability to precisely label the nanobodies with a single fluorophore. This one-to-one labeling between the nanobodies and fluorophores was confirmed, and intensity distributions from SiMPull experiments were much more well-defined compared to IgG antibodies or antibody fragments that were labelled with traditional non-targeted methods. Unfortunately, issues with either multiple nanobodies binding to the detection antibody or potential aggregation of the detection antibodies prevented the main goal of this work in applying quantitative intensity SiMPull assays to the analysis of protein stoichiometry. However, alternative approaches are possible, for example the use of F(*ab*) fragments as the primary capture and detection antibodies, combined with nanobodies that target the F(*ab*) domain rather than the Fc region of IgG molecules would likely achieve one-to-one labeling of proteins and fluorophores.

Alternatively, another approach could be to use label-free microscopy techniques rather than fluorescence microscopy. I outlined a method that could extend mass photometry to also probe protein structure by combining the technique with single-molecule CD spectroscopy. This could be a powerful approach that could clarify relationships between protein misfolding and disease pathology and be used as a diagnostic tool. In short, there exist a variety of methods to implement quantitative intensity-based single-molecule analysis. Each offers benefits in terms of ease of use and the information that can be extracted from the sample, but the most widely adopted techniques will be those that balance both data-rich analysis and approachability.

APPENDIX A: DETAILED NANOBODY PROTOCOLS

Day 1: Preculture Growth

1. In the morning: Prepare 2x-YT Growth medium (~200 mL) and autoclave with the lid slightly loosened along with three small flasks (2x 125 mL and 250 mL) with foil caps loosely attached.
    a. 6.2 g 2x-YT medium in 200 mL MilliQ
2. In the afternoon: Allow the autoclave to cool to roughly room temperature, keep broth and flasks in the autoclave until ready to use.
3. Set the incubator to 28°C and ~185 rpm.
4. Add 60 mL medium to each flask, and 60 μg/mL kanamycin to each flask (50 μL of 50 mg/mL stock). Use tape to label the 125 mL flasks for nanobodies and 250 mL flask for protease.
    a. Kanamycin should be used at a 50 μg/mL concentration.
5. Retrieve the frozen bacteria stocks from the -80°C freezer. Quickly add roughly a pea-sized chunk of the stock to the flask using a sterilized toothpick or autoclaved pipette tip, and swirl the flask to dissolve. Do not allow the frozen bacteria stocks to thaw. Return the stocks to the -80°C freezer as soon as you are done with this step.
    a. Anti-Rabbit 1x Cys Nanobody, 104163
    b. NEPP8 Protease, 104131
6. Place the flasks in the incubator using the magnetic mounts and incubate overnight.
7. Dispose of excess 2x-YT medium using 10% bleach, spray the bottle with 70% ethanol, and thoroughly rinse with water.
8. Make two 400 mL bottles of 2x-YT medium.
    a. 12.4 g 2x-YT medium in 400 mL MilliQ
9. Autoclave the rinsed bottle and the fresh medium along with a 1L flask and 500 mL flask, each with foil lids. Leave these in the autoclave overnight.

Day 2: Culture Growth and Induction

Note: Make the buffers at the end of this section while the cultures grow.

1. If the bacteria cultures are turbid, proceed with the growth process.
    a. The protease culture may have grown slowly overnight. As long as it shows any sign of turbidity or color change from 2x-YT medium you can proceed. See later notes.
2. Reduce incubator temperature to 25°C. Maintain an rpm of ~185.
3. Retrieve flasks and growth medium from autoclave. Place the cleaned bottle from yesterday on a rack to dry.
4. Add 400 mL medium to the 1 L flask and label with tape as nanobodies. Add 300 mL medium to the 500 mL flask and label with tape as protease.
5. Add 500 uL kanamycin to the 1 L nanobody flask, add 330 μL kanamycin to the 500 mL protease flask.
    a. Note: If protease grew slowly add 360 μL kanamycin (maintain 50 μg/mL concentration), and add more of the frozen stock to the final culture flask.

6. Add 50 mL of each nanobody culture to the 1 L flask and swirl for a total volume of 500 mL.
7. Add 30 mL of the protease culture to the 500 mL flask and swirl for a total volume of 330 mL.
    a. Note: Add full 60 mL culture if it grew slowly for a total volume of 360 mL.
8. Place flasks in incubator and grow for ~1/2 – 1 hr depending on turbidity.
9. Once the cultures reach an OD_{600} of ~0.75, induce protein overexpression by adding 0.2 mM IPTG to the culture and swirl.
10. Grow for ~3-5 hours until an OD_{600} of ~2.5 is obtained. Add 1 mM PMSF to inhibit protease activity.

    Note: If the protease culture has not grown much, once the nanobody culture is removed you can increase the temperature to 32°C. Did not test higher temperatures.
11. Pellet the cultures in 50 mL Falcon tubes by centrifuging at the max speed (1800 g) for 20 min. Discard supernatant in 10% bleach. Vacuum seal the pellets and freeze overnight at -20°C.
12. Clean all bottles and flasks by spraying with 70% ethanol, thoroughly rinsing, and autoclave them overnight.

Nanobody Lysis Buffer: Make one 50 mL vial

- 50 mM Tris/HCl pH=7.5, 300 mM NaCl, 10 mM imidazole, 5 mM DTT

Protease Lysis Buffer: Make one 50 mL vial

- 50 mM Tris pH=8.0, 300 mM NaCl, 25 mM imidazole, 10 mM DTT, 250 mM sucrose

Maleimide Labeling Buffer: Make two 40 mL vials

- 100 mM potassium phosphate pH=7.5, 150 mM NaCl, 250 mM sucrose

Protease Cleavage Buffer: Make one 25 mL vial

- 50 mM Tris/HCl pH=7.5, 300 mM NaCl, 10 mM DTT, 250 mM sucrose

Day 3: Lysis, Purification, and Labeling

1. Remove pellets from freezer to thaw at room temperature.
2. Remove glassware from autoclave to dry.
3. Attach microtip to the ultrasonifer using the wrench.
4. Fill a stryofoam cooler with ice.
5. Once thawed, re-suspend the pellets by pipetting 10x per pellet with 5 mL of the appropriate lysis buffer.
    a. Use 5 mL buffer to resuspend 1 pellet, transferring the liquid from the first pellet to the next. Repeat for four pellets in total. After re-suspending 4 pellets, place the liquid in a clean 50 mL Falcon tube and store on ice. Repeat until all pellets are re-suspended.
6. Add the appropriate lysis buffer to the re-suspended bacteria so that the total volume for each tube is ~35 mL.

    a. Note: Do not use less than 30 mL. Too small a volume will result in a viscous lysate which clogs the Ni-NTA column, increasing purification time and decreasing protein collection.
7. Set the ultrasonifier to a 25% amplitude and 50% duty cycle. Sterilize the tip by spraying and wiping with 70% ethanol. Place the cooler so that the first vial of bacteria is directly underneath the ultrasonifier tip. Carefully lower the tip into the bacteria solution so that the tip is centered and does not touch the walls of the container. Make sure the vial is in good contact with the ice.
8. With a timer, turn the sonifier on to the "Stay on" position for 10 seconds. Turn off and wait 1 minute. Repeat this process two more times for a total lysing time of 30 seconds.
9. Remove the tip, cap the bacteria lysate, and wipe the ultasonifier tip with ethanol to sterilize.
10. Repeat the lysis procedure for the second vial of bacteria. Sterilize the ultrasonifier tip when done and put away.
11. Turn on the ultracentrifuge and set the temperature to 4°C.
12. Transfer the lysate to 1.5 mL vials. Be sure to mark the vials as either nanobody or protease. Centrifuge at 4°C for 1 hour at 18,000 g.
13. Carefully collect the supernatant without disturbing the pellet and transfer to a clean 50 mL tube. Store the collected supernatant on ice.
14. Purify the nanobodies and protease with in two separate Ni-NTA columns:
    a. Wash the column with 10 mL MilliQ. Place the yellow stopper on the column.
    b. Invert the Ni-Aragose multiple times to mix. Pipette 1 mL back and forth to mix. Gently pipette 1 mL into the column avoiding bubbles. Tap the column to move any bubbles in the gel to the surface. Remove the stopper and allow the liquid to flow through. Be careful to not disturb the gel bed or let it dry out after this point.
    c. Equilibrate each column with 5 mL of the appropriate lysis buffer.
    d. Add the supernatant to the column and let it flow through. This will require multiple refills of the column and will usually take a couple hours.
        i. During this time make 6 mL each of the elution buffers (3 mL of the appropriate lysis buffer, 3 mL of 1 M imidazole) and washing buffers (2.7 mL appropriate lysis buffer, 0.3 mL of 200 mM imidazole pH=7.5)
    e. In 1 mL increments, wash with 3 mL of the appropriate lysis buffer then 2 mL of the appropriate washing buffer, allowing the liquid to fully flow through the column for each step. Collect each mL in a labelled 1.5 mL vial.
    f. In 1 mL increments, elute the protein using 4 mL of the appropriate elution buffer. Collect each mL in a labelled 1.5 mL vial.
    g. Add ~4 mL of 20% ethanol to the column. After ~2mL has flowed through, add the stopper and cap and store in the 4°C fridge until recharging the Ni-NTA resin.
15. Check the A_{280} of the washout and elutes.
    a. Nanobody: ε_{280} = 25,500 M/cm, Protease: ε_{280} = 28,000 M/cm
16. Using a PD Miditrap G25 column, buffer exchange the first elutes of the protease sample to protease cleavage buffer and the nanobody sample to maleimide labeling buffer. Add 10 mM imidazole to the nanobodies.

17. Check the A_{280} of the buffer exchanged proteins. Get two 1.5 mL vials and add ~700 µL of nanobody to each. If nanobody concentration is < 100 µM, add ~2 µM protease so the volume of each vial is less than 800 µL. If that is not possible, try to keep the volume of each cleavage reaction to less than 1 mL to minimize loss of cleaved nanobodies in later steps. If the concentration of the nanobodies is > 100 µM, you will likely need a higher concentration of protease. Adjust volumes accordingly.
18. Incubate the cleavage reactions in the 4°C fridge for 2 hours.
    a. Make the elution buffer (5 mL maleimide labeling buffer, 5 mL 1 M imidazole).
    b. Make the snap-freezing buffer (50% maleimide labeling buffer, 50% glycerol, 10 mM DTT).
19. Prepare two Ni-NTA columns:
    a. Wash the column with 10 mL MilliQ. Place the yellow stopper on the column.
    b. Invert the Ni-Aragose multiple times to mix. Pipette 1 mL back and forth to mix. Gently pipette 1 mL into the column avoiding bubbles. Tap the column to move any bubbles in the gel to the surface. Remove the stopper and allow the liquid to flow through. Be careful to not disturb the gel bed or let it dry out after this point.
    c. Equilibrate each column with 5 mL of maleimide labeling buffer.
    d. Place a 1.5 mL vial under the column. Add one cleavage reaction to each column and collect the flow through.
    e. Place new 1.5 mL vials under the column. Add 4 mL of maleimide labeling buffer in 1 mL increments, collecting each mL in a new vial.
    f. In 1 mL increments, elute the protease+cleaved portion of the nanobody using 4 mL of elution buffer. Collect each mL in a labelled 1.5 mL vial.
    g. Add ~4 mL of 20% ethanol to the column. After ~2mL has flowed through, add the stopper and cap and store in the 4°C fridge until recharging the Ni-NTA resin.
20. Measure the concentration of the cleaved nanobodies (should only need the first mL from step 19d). Use the higher concentration sample for labeling. The other sample will be snap frozen.
21. Using a PD MidiTrap G25 column, buffer exchange the higher concentration sample to maleimide labeling buffer. Measure the concentration.
22. Split the buffer exchanged nanobodies into two vials of equal volume, ~750 µL. Add a 4x molar excess of maleimide-conjugated dye. (AlexaFluor647 maleimide is 20 nmoles per 5 µL tube). Mix well by gentle pipetting back and forth. Incubate overnight in the 4°C fridge.
23. Aliquot the lower concentration sample from Step 20 at an appropriate concentration and volume. Reasonable: ~200 µL total volume; 100 µL of ~45 µM cleaved nanobodies, 100 µL of snap-freezing buffer. Do not go much below 25% glycerol for snap freezing.
24. Pour some liquid nitrogen into a Styrofoam cooler or lid, place aliquots in liquid nitrogen and move them around until completely frozen. Quickly place the frozen aliquots in a box and store in the -80°C freezer.
25. Clean up and sterilize workstation.

Day 4: Buffer exchange

1. Buffer exchange each labeling reaction in two separate PD MidiTrap G25 columns to maleimide labeling buffer or PBS to remove excess dye.
2. Measure the degree of labeling using the A_{280} and peak absorption of the dye (A647 is A_{650}). I found that one buffer exchange left a significant amount of dye and a second exchange was necessary (went from a degree of labeling of ~1.6 to 1.09). If this is the case, snap freeze one of the buffer exchanged samples in the snap freezing buffer from Step 18 of Day 3. After a second buffer exchange, determine the degree of labeling.
3. Ideal storage conditions of the labeled nanobodies is uncertain. Store some in 4°C, some in -20°C, and aliquot some in -80°C if necessary. Samples stored in 4°C seemed stable for more than a year.
4. Check samples via SDS-PAGE (nanobodies in maleimide labeling buffer, protease in cleavage buffer, cleaved nanobodies, protease+cleaved portion of nanobody, labeled nanobody).
5. Check monovalent labeling and nonspecific binding via single-molecule experiments.

APPENDIX B: SINGLE-MOLECULE LOCALIZATION CODES

```
function simpull(first_file_num,num_of_file_to_read,std_set)

    close all;
    fclose('all');

    counts = zeros(num_of_file_to_read,1);
    hist_data = zeros(1,1002);
    xtrace=[];
    allspots=[];
    Imax_all=[];
    for i=1:num_of_file_to_read
       [counts(i,1), counts_hist, center_ave, ~, spots, ~] = FindSpots100x_16bit(i + first_file_num -
   1,std_set); %count all molecules
       hist_data = hist_data + counts_hist;
       allspots=[allspots; spots];
       xtrace=[xtrace; center_ave];
    end
    counts(counts==0)=[];

    %Readout Useful Parameters
    mean_SBR=mean(allspots(:,5));
    stdev_SBR=std(allspots(:,5));
    mean_intensity=mean(allspots(:,3));
    stdev_intensity=std(allspots(:,3));
    sigma=stdev_intensity/mean_intensity;

    %Raw 1D Intensity
    xtrace=sortrows(xtrace);

     %Averaged 1D Intensity info
     %Average any spots at the same x_coordinate
     [C,ia,idx] = unique(xtrace(:,1),'stable');
     val = accumarray(idx,xtrace(:,2),[],@mean);
     ave_1D = [C val];
    figure()
    plot(C,val)

    a=num2str(first_file_num);
    b=num2str(first_file_num + num_of_file_to_read - 1);

    average_count = mean(double(counts))
```

```
    std_count = std(double(counts))

    dlmwrite(['Counts_' a 'to' b '.txt'], counts,'delimiter','\t');
    dlmwrite(['hel' a 'to' b '1D Trace.txt'],xtrace,'delimiter','\t');
    dlmwrite(['hel' a 'to' b 'Ave_1D Trace.txt'],ave_1D,'delimiter','\t');
    dlmwrite(['histogram_' a 'to' b '.txt'], hist_data','delimiter','\t');
    dlmwrite(['spots' a 'to' b '.txt'], allspots,'delimiter','\t');
end
```

```
function [N_Good, counts_hist, center_ave, film_x, spots, Imax] =
FindSpots100x_16bit(file_num,std_set)

circle=zeros(11,11);
circle(1,:) = [ 0,0,0,0,0,0,0,0,0,0,0];
circle(2,:) = [ 0,0,0,0,0,0,0,0,0,0,0];
circle(3,:) = [ 0,0,0,0,0,1,0,0,0,0,0];
circle(4,:) = [ 0,0,0,0,1,0,1,0,0,0,0];
circle(5,:) = [ 0,0,0,1,0,0,0,1,0,0,0];
circle(6,:) = [ 0,0,1,0,0,0,0,0,1,0,0];
circle(7,:) = [ 0,0,0,1,0,0,0,1,0,0,0];
circle(8,:) = [ 0,0,0,0,1,0,1,0,0,0,0];
circle(9,:) = [ 0,0,0,0,0,1,0,0,0,0,0];
circle(10,:) = [ 0,0,0,0,0,0,0,0,0,0,0];
circle(11,:) = [ 0,0,0,0,0,0,0,0,0,0,0];

circle1=zeros(11,11);
circle1(1,:) = [ 0,0,0,0,0,0,0,0,0,0,0];
circle1(2,:) = [ 0,0,0,0,0,1,0,0,0,0,0];
circle1(3,:) = [ 0,0,0,0,1,1,1,0,0,0,0];
circle1(4,:) = [ 0,0,0,1,1,1,1,1,0,0,0];
circle1(5,:) = [ 0,0,1,1,1,1,1,1,1,0,0];
circle1(6,:) = [ 0,1,1,1,1,1,1,1,1,1,0];
circle1(7,:) = [ 0,0,1,1,1,1,1,1,1,0,0];
circle1(8,:) = [ 0,0,0,1,1,1,1,1,0,0,0];
circle1(9,:) = [ 0,0,0,0,1,1,1,0,0,0,0];
circle1(10,:) = [ 0,0,0,0,0,1,0,0,0,0,0];
circle1(11,:) = [ 0,0,0,0,0,0,0,0,0,0,0];

bgcheck=zeros(11,11);
bgcheck(1,:) = [ 0,0,0,0,0,0,0,0,0,0,0];
bgcheck(2,:) = [ 0,1,1,1,1,1,1,1,1,1,0];
bgcheck(3,:) = [ 0,1,0,0,0,0,0,0,0,1,0];
bgcheck(4,:) = [ 0,1,0,0,0,0,0,0,0,1,0];
bgcheck(5,:) = [ 0,1,0,0,0,0,0,0,0,1,0];
bgcheck(6,:) = [ 0,1,0,0,0,0,0,0,0,1,0];
bgcheck(7,:) = [ 0,1,0,0,0,0,0,0,0,1,0];
bgcheck(8,:) = [ 0,1,0,0,0,0,0,0,0,1,0];
bgcheck(9,:) = [ 0,1,0,0,0,0,0,0,0,1,0];
bgcheck(10,:) = [ 0,1,1,1,1,1,1,1,1,1,0];
bgcheck(11,:) = [ 0,0,0,0,0,0,0,0,0,0,0];
```

```
%Set initial values
numskipped=0;

%Read in file
%8 bit .pma
fname=num2str(file_num);
fid=fopen(['hel' fname '.pma']);
film_x=fread(fid, 1, 'uint16');
film_y=fread(fid, 1, 'uint16');
fileinfo = dir(['hel' fname '.pma']);
film_l = (fileinfo.bytes-4)/(film_x*film_y);
fprintf(['hel' fname '.pma','\n']);
fprintf(['film_x=',num2str(film_x),'\n']);
fprintf(['film_y=',num2str(film_y),'\n']);
fprintf(['film_l=',num2str(film_l),'\n']);

% %16 bit smm file
% fname=num2str(file_num);
% fname=['film' fname '.smm'];
% disp(fname)
%
% fid=fopen(fname,'r');
% FileInfo = dir(fname);
% FileSize = FileInfo.bytes;
%
% film_x = fread(fid,1,'int16');
% film_y = fread(fid,1,'int16');
% frame = zeros(film_x,film_y,'uint16');
%
% film_l = (int32(FileSize)-17)/(film_x*film_y)/2;
% bpp = fread( fid, 1, 'uint8');
% background = fread( fid, 1, 'uint32');
% data_scaler = fread( fid, 1, 'uint32');
% framecycle = fread( fid, 1, 'float32');

ffilm_l=10;
aver=zeros(film_x,film_y);

for i=1:ffilm_l
```

```
   column_data=fread(fid,film_x*film_y,'uint8');  %8 bit pma
%    column_data=fread(fid,film_x*film_y,'uint16'); %16 bit smm
   frame=transpose(reshape(column_data,film_x,film_y));
   aver=aver+frame;
end
aver=aver/ffilm_l;
frame=aver;
framemed=median(frame(:));

figure(1), imshow(frame,[]); axis image

%Subtract background local background
% temp1=smooth2a(frame,2,2);
%    bin_back=zeros(film_x/16,film_y/16);
%    for i=8:16:film_x
%       for j=8:16:film_y
%          bin_back((i+8)/16,(j+8)/16)=min(min(temp1(i-7:i+8, j-7:j+8)));
%       end
%    end
%    temp2=ones(16);
%    backg_aver=kron(bin_back, temp2);%back to 512*512
%    backg_aver=smooth2a(backg_aver,10,10);
% %    temp1=temp1-backg_aver+10;
%    temp1=temp1-0.75*backg_aver;
%    temp_ns=frame-0.75*backg_aver;
%    temp_ns(temp_ns < 0 ) = 0;

%%
%Threshold the image for peak finding
temp1=frame;
temp1(temp1<framemed*1.015)=0; %1.015
temp=temp1;
% temp_ns=frame;
med=median(temp(:));

%Subtract global background and find initial peaks
temp(temp < med+std_set ) = 0;
% temp_ns(temp_ns < med+std_set+5) = 0;
% temp_norm=temp/max(temp(:));
findpeaks=imregionalmax(temp);
```

```
%Binarize and segment (for 16 bit analysis of fibrils, not needed for single molecule)
tempb=imbinarize(temp1,'global');
bwoutline=bwperim(tempb,4);
overlay=temp;
overlay(bwoutline)=5000;
%Create a structure that assigns one matrix to each spot/cluster
% spotmat=bwconncomp(bwoutline);
spotmat=bwconncomp(tempb);
spotstruct=cell([1 length(spotmat.PixelIdxList)]);
regionint=zeros(1,length(spotstruct)); regionbg=regionint; badreg=logical(regionint);
for list = 1:length(spotmat.PixelIdxList)
   [y,x] = ind2sub(size(frame),spotmat.PixelIdxList{list});
   Spotstruct{list} = [x,y];
%    %use findpeak info to threshold cluster
   minx=min(x); maxx=max(x);
   miny=min(y); maxy=max(y);
   region=frame(miny:maxy,minx:maxx);
%    %check for multiple peaks within one region, keep brightest
%    if sum(sum(findpeaks(miny:maxy,minx:maxx)))>1
%       [maxregion, maxind] = max(region(:));
%       [regmaxy, regmaxx] = ind2sub(size(region),maxind);
%       findpeaks(miny:maxy,minx:maxx)=0;
%       findpeaks(miny+regmaxy-1,minx+regmaxx-1)=1;
%    end
   %If region is 3 pixels or less set to 0
   if length(spotstruct{list})<=3
      temp(miny:maxy,minx:maxx)=0;
      findpeaks(miny:maxy,minx:maxx)=0;
      badreg(list)=1;
   else
      %take the top 70% of intensity
      if minx==1 || maxx==512 || miny==1 || maxy==512
         intregion=region;
      else
         intregion=frame(miny-1:maxy+1,minx-1:maxx+1);
      end
      regionmax=max(region(:)); regionmin=framemed+floor(0.3*(regionmax-framemed));
      regionint(list)=sum(intregion(intregion>regionmin));
      numpix=numel(intregion(intregion>regionmin));
      regionbg(list)=numpix*framemed;
   end
```

```
end
spotstruct(badreg)=[];
regionint(regionint==0)=[];
regionbg(regionbg==0)=[];
regioncorrected=regionint-regionbg;
% regionint(regionint==0)=[];
%Store pixel information
% pixel_int=reshape(temp,[film_x*film_y,1]);
% pixel_int(pixel_int==0)=[];
% pixel_int=sort(pixel_int);

%find the peaks
temp3=frame;

%List of spot centers and amplitudes
spots=zeros(5000,6);
N_Good=0;
N_All=0;

%For standard single molecule spotfinding
% overlay(findpeaks)=5000;
% figure(2), imagesc(overlay), axis image;
% pixel_int=temp(findpeaks);
% pixel_int=sort(pixel_int);
% findpeaks=imregionalmax(temp_ns);
checkempty=sum(findpeaks(:));

%    figure()
%    imagesc(findpeaks)
%    axis image

dense=0;
sharp=0;
if checkempty ~= film_x*film_y
   for i= 10:film_x-10
      for j=10:film_y-10
         if findpeaks(j,i)>0
            x=i; y=j;
            Isum=0; Ibg=0; yup=0;
            %check if good spot
            if yup==0
```

```
            % roundness check for the single molecule spots
%               std_x = std(temp_ns(y, -4+x:4+x));
%               std_y = std(temp_ns(y-4:y+4, x));
%               Var = std_x/std_y;
%               if Var > 1.3 || Var < 0.7
%                   yup = 1;
%               end
            %check surrounding area
            if yup==0
               for k=-5:5
                  for l=-5:5
%                       if circle(k+6,l+6)>0
%                          if temp1(j+k,i+l)>0.8*temp1(y,x)
% %                             fprintf('not sharp')
%                             sharp=sharp+1;
%                             yup=1;
%                          end
%                       end
%                       if bgcheck(k+6,l+6)>0
%                          if temp1(j+k,i+l)>med+0.2*temp_ns(y,x)
%                             fprintf('too dense')
%                             dense=dense+1
%                             yup=1;
%                          end
%                       end
                     %Sum intensity of spot
                     if yup==0 && circle1(k+6,l+6)>0
                        Isum=Isum+temp1(j+k,i+l); %was temp, frame
                     end
                  end
               end
            end
            %check if we have it already (or adjacent pixel) and keep brighter spot
            for k=1:N_All
               if abs(x-spots(k,1))<=1 && abs(y-spots(k,2))<=1
                  yup=1;
                  if Isum-41/32*Ibg > spots(k,3)
                     temp3(spots(k,1),spots(k,2))=spots(k,6); %replace original intensity
                     spots(k,1)=x;
                     spots(k,2)=y;
                     %Remove scaled and averaged bg from spot intensity
```

```
                    spots(k,3)=Isum-41/32*Ibg; %Standard
%                     spots(k,3)=Isum; %No bg correction
%                    spots(k,3)=temp(y,x); %Peak intensity
%                    spots(k,4)=6/40*Ibg;
                   spots(k,4)=6/32*Ibg;
                   spots(k,5)=spots(N_Good,3)/spots(N_Good,4);
                   spots(k,6)=temp1(y,x);
                   temp(j,i)=10000; %Mark the new spot
                 end
               end
             end
             %Check SBR
              if (Isum-41/32*Ibg)/(6/32*Ibg)<1
                 yup=1;
              end
             %Store the peak positions
             if yup==0
               N_All=N_All+1;
               N_Good=N_Good+1;
               spots(N_Good,1)=x;
               spots(N_Good,2)=y;
               %Remove scaled and averaged bg from spot intensity
                spots(N_Good,3)=Isum-41/32*Ibg; %Standard
%                  spots(N_Good,3)=Isum; % No bg correction
%                 spots(N_Good,3)=temp(y,x); %Peak intensity
%                 spots(N_Good,4)=6/40*Ibg;
               spots(N_Good,4)=6/32*Ibg;
               spots(N_Good,5)=spots(N_Good,3)/spots(N_Good,4);
               spots(N_Good,6)=temp1(y,x);
               temp(j,i)=10000;
             end
          end
        end
      end
   end
end

figure(2); imagesc(overlay); axis image;

figure(3);
imagesc(temp);
```

```
axis image;

assignin('base','spots_glob',spots)
fprintf(['The number of detected spots was ' num2str(N_Good) '\n']);

%% Create 1D Intensity Distribution
spots=sortrows(spots,1);
spots(all(spots==0,2),:)=[];
[rows columns]=size(spots);
counter=1;
center=[];
center_ave=[];
%Find spots in center region of image
if isempty(spots)==0
   for i=1:rows
      if spots(i,2) > 0.25*film_y && spots(i,2) < 0.75*film_y
         center(counter,1) = spots(i,1); center(counter,2)=spots(i,3);
         counter=counter+1;
      end
   end
   if isempty(center)==0
      %Average any spots at the same x_coordinate
      [C,ia,idx] = unique(center(:,1),'stable');
       val = accumarray(idx,center(:,2),[],@mean);
       center_ave = [C val];

       figure(4)
       plot(C,val)
   end
else
   center_ave = [];
end

%Find is the maximum spot intensity
Imax=max(spots(:,3));

%% Generate Histogram Data
% I=spots(:,3); %standard
% I=regionint;
% I=pixel_int;
I=regioncorrected; %fibril
```

```
bin_size=1;
I(I<0)=[];
figure(5);
%edges = [0 0:30:2400 2401];
edges = [0 0:bin_size:1000 10001];
h=histogram(I,edges);
counts_hist = h.Values;
% dim=[.7 .4 .4 .5];
% filename=['hel' num2str(file_num)];
% thresh=['threshold=' num2str(std_set)];
% plotdet=(filename,thresh);
% a=annotation('textbox',dim, 'String', plotdet, 'FitBoxToText','on');
fclose(fid);

end
```

LIST OF REFERENCES

1. Dobell C, Leeuwenhoek Av. *Antony van Leeuwenhoek and his "Little animals"; being some account of the father of protozoology and bacteriology and his multifarious discoveries in these disciplines*. New York: Harcourt, Brace and company; 1932.

2. Murata K, Wolf M. Cryo-electron microscopy for structural analysis of dynamic biological macromolecules. *Biochimica et Biophysica Acta (BBA) - General Subjects* 2018, 1862:324-334.

3. Petsko GA, Ringe D. *Protein Structure and Function*. Massachusetts, USA: New Science Press; 2004.

4. Lichtman JW, Conchello J-A. Fluorescence microscopy. *Nature Methods* 2005, 2:910-919.

5. Minsky M. Confocal scanning microscope. *Rapport technique, Patent* 1955, 3:14.

6. Wilson T. Resolution and optical sectioning in the confocal microscope. *Journal of Microscopy* 2011, 244:113-121.

7. Petráň M, Hadravský M, Egger MD, Galambos R. Tandem-Scanning Reflected-Light Microscope*. *Journal of the Optical Society of America* 1968, 58:661-664.

8. Sheppard CJR, Mao XQ. Confocal Microscopes with Slit Apertures. *Journal of Modern Optics* 1988, 35:1169-1185.

9. Brakenhoff GJ, Visscher K. Confocal imaging with bilateral scanning and array detectors. *Journal of Microscopy* 1992, 165:139-146.

10. Jialei T, Jinhan R, Kyu Young H. Fluorescence imaging with tailored light. *Nanophotonics* 2019, 8:2111-2128.

11. Tokunaga M, Imamoto N, Sakata-Sogawa K. Highly inclined thin illumination enables clear single-molecule imaging in cells. *Nature Methods* 2008, 5:159-161.

12. Tang J, Han KY. Extended field-of-view single-molecule imaging by highly inclined swept illumination. *Optica* 2018, 5:1063-1069.

13. Voie AH, Burns DH, Spelman FA. Orthogonal-plane fluorescence optical sectioning: Three-dimensional imaging of macroscopic biological specimens. *Journal of Microscopy* 1993, 170:229-236.

14. Huisken J, Swoger J, Del Bene F, Wittbrodt J, Stelzer EHK. Optical Sectioning Deep Inside Live Embryos by Selective Plane Illumination Microscopy. *Science* 2004, 305:1007-1009.

15. Keller PJ, Schmidt AD, Wittbrodt J, Stelzer EHK. Reconstruction of Zebrafish Early Embryonic Development by Scanned Light Sheet Microscopy. *Science* 2008, 322:1065-1069.

16. Fahrbach FO, Simon P, Rohrbach A. Microscopy with self-reconstructing beams. *Nature Photonics* 2010, 4:780-785.

17. Betzig E. Sparse and composite coherent lattices. *Physical Review A* 2005, 71:063406.

18. Chang B-J, Kittisopikul M, Dean KM, Roudot P, Welf ES, Fiolka R. Universal light-sheet generation with field synthesis. *Nature Methods* 2019, 16:235-238.

19. Forero-Shelton M. Peering into cells at high resolution just got easier. *Nature methods* 2019, 16:293-294.

20. Axelrod D. Total internal reflection fluorescence microscopy in cell biology. *Traffic* 2001, 2:764-774.

21. Axelrod D, Burghardt TP, Thompson NL. Total internal reflection fluorescence. *Annual review of biophysics and bioengineering* 1984, 13:247-268.

22. Stout AL, Axelrod D. Evanescent field excitation of fluorescence by epi-illumination microscopy. *Applied Optics* 1989, 28:5237-5242.

23. Kolb HC, Finn MG, Sharpless KB. Click Chemistry: Diverse Chemical Function from a Few Good Reactions. *Angewandte Chemie International Edition* 2001, 40:2004-2021.

24. Funatsu T, Harada Y, Tokunaga M, Saito K, Yanagida T. Imaging of single fluorescent molecules and individual ATP turnovers by single myosin molecules in aqueous solution. *Nature* 1995, 374:555-559.

25. Macklin JJ, Trautman JK, Harris TD, Brus LE. Imaging and Time-Resolved Spectroscopy of Single Molecules at an Interface. *Science* 1996, 272:255-258.

26. Laemmli UK. Cleavage of Structural Proteins during the Assembly of the Head of Bacteriophage T4. *Nature* 1970, 227:680-685.

27. Moerner WE. A Dozen Years of Single-Molecule Spectroscopy in Physics, Chemistry, and Biophysics. *The Journal of Physical Chemistry B* 2002, 106:910-927.

28. Hell SW. Toward fluorescence nanoscopy. *Nature Biotechnology* 2003, 21:1347.

29. Yildiz A, Selvin PR. Fluorescence imaging with one nanometer accuracy (FIONA): Application to molecular motors. *European Biophysics Journal with Biophysics Letters* 2005, 34:580-580.

30. Yildiz A, Forkey JN, McKinney SA, Ha T, Goldman YE, Selvin PR. Myosin V Walks Hand-Over-Hand: Single Fluorophore Imaging with 1.5-nm Localization. *Science* 2003, 300:2061-2065.

31. Hell SW, Wichmann J. Breaking the diffraction resolution limit by stimulated emission: stimulated-emission-depletion fluorescence microscopy. *Optics Letters* 1994, 19:780-782.

32. Klar TA, Jakobs S, Dyba M, Egner A, Hell SW. Fluorescence microscopy with diffraction resolution barrier broken by stimulated emission. *Proceedings of the National Academy of Sciences of the United States of America* 2000, 97:8206-8210.

33. Hess ST, Girirajan TPK, Mason MD. Ultra-high resolution imaging by fluorescence photoactivation localization microscopy. *Biophysical Journal* 2006, 91:4258-4272.

34. Rust MJ, Bates M, Zhuang X. Sub-diffraction-limit imaging by stochastic optical reconstruction microscopy (STORM). *Nature Methods* 2006, 3:793-796.

35. Heilemann M, van de Linde S, Schüttpelz M, Kasper R, Seefeldt B, Mukherjee A, Tinnefeld P, Sauer M. Subdiffraction-Resolution Fluorescence Imaging with Conventional Fluorescent Probes. *Angewandte Chemie International Edition* 2008, 47:6172-6176.

36. Roy R, Hohng S, Ha T. A practical guide to single-molecule FRET. *Nature Methods* 2008, 5:507-516.

37. Joo C, McKinney SA, Nakamura M, Rasnik I, Myong S, Ha T. Real-Time Observation of RecA Filament Dynamics with Single Monomer Resolution. *Cell* 2006, 126:515-527.

38. Sternberg SH, LaFrance B, Kaplan M, Doucina JA. Conformational control of DNA target cleavage by CRISPR-Cas9. *Nature* 2015, 527:110-113.

39. Farooq S, Hohlbein J. Camera-based single-molecule FRET detection with improved time resolution. *Physical Chemistry Chemical Physics* 2015, 17:27862-27872.

40. Tang J, Sun Y, Pang S, Han KY. Spatially encoded fast single-molecule fluorescence spectroscopy with full field-of-view. *Scientific Reports* 2017, 7:10945.

41. Jain A, Liu RJ, Ramani B, Arauz E, Ishitsuka Y, Ragunathan K, Park J, Chen J, Xiang YK, Ha T. Probing cellular protein complexes using single-molecule pull-down. *Nature* 2011, 473:484-U322.

42. Wang X, Yu S, Li F, Feng T. Detection of α-synuclein oligomers in red blood cells as a potential biomarker of Parkinson's disease. *Neuroscience Letters* 2015, 599:115-119.

43. Hartl FU. Protein Misfolding Diseases. *Annual Review of Biochemistry* 2017, 86:21-26.

44. Spillantini MG, Schmidt ML, Lee VMY, Trojanowski JQ, Jakes R, Goedert M. α-Synuclein in Lewy bodies. *Nature* 1997, 388:839-840.

45. Dijkstra AA, Voorn P, Berendse HW, Groenewegen HJ, Netherlands Brain B, Rozemuller AJM, van de Berg WDJ. Stage-dependent nigral neuronal loss in incidental Lewy body and Parkinson's disease. *Movement Disorders* 2014, 29:1244-1251.

46. Damier P, Hirsch EC, Agid Y, Graybiel AM. The substantia nigra of the human brain: II. Patterns of loss of dopamine-containing neurons in Parkinson's disease. *Brain* 1999, 122:1437-1448.

47. Tuttle MD, Comellas G, Nieuwkoop AJ, Covell DJ, Berthold DA, Kloepper KD, Courtney JM, Kim JK, Barclay AM, Kendall A, et al. Solid-state NMR structure of a pathogenic fibril of full-length human α-synuclein. *Nature Structural & Molecular Biology* 2016, 23:409-415.

48. Tosatto L, Horrocks MH, Dear AJ, Knowles TPJ, Dalla Serra M, Cremades N, Dobson CM, Klenerman D. Single-molecule FRET studies on alpha-synuclein oligomerization of Parkinson's disease genetically related mutants. *Scientific Reports* 2015, 5:16696.

49. Chen SW, Drakulic S, Deas E, Ouberai M, Aprile FA, Arranz R, Ness S, Roodveldt C, Guilliams T, De-Genst EJ, et al. Structural characterization of toxic oligomers that are kinetically trapped during α-synuclein fibril formation. *Proceedings of the National Academy of Sciences* 2015, 112:E1994-E2003.

50. Gallea JI, Celej MS. Structural insights into amyloid oligomers of the Parkinson disease-related protein α-synuclein. *The Journal of biological chemistry* 2014, 289:26733-26742.

51. Weinreb PH, Zhen W, Poon AW, Conway KA, Lansbury PT. NACP, A Protein Implicated in Alzheimer's Disease and Learning, Is Natively Unfolded. *Biochemistry* 1996, 35:13709-13715.

52. Jain A, Arauz E, Aggarwal V, Ikon N, Chen J, Ha T. Stoichiometry and assembly of mTOR complexes revealed by single-molecule pulldown. *Proceedings of the National Academy of Sciences* 2014, 111:17833-17838.

53. Jain A, Liu R, Xiang YK, Ha T. Single-molecule pull-down for studying protein interactions. *Nature Protocols* 2012, 7:445-452.

54. Volles MJ, Lansbury PT. Relationships between the Sequence of α-Synuclein and its Membrane Affinity, Fibrillization Propensity, and Yeast Toxicity. *Journal of Molecular Biology* 2007, 366:1510-1522.

55. Outeiro TF, Putcha P, Tetzlaff JE, Spoelgen R, Koker M, Carvalho F, Hyman BT, McLean PJ. Formation of Toxic Oligomeric α-Synuclein Species in Living Cells. *PLOS ONE* 2008, 3:e1867.

56. Danzer KM, Haasen D, Karow AR, Moussaud S, Habeck M, Giese A, Kretzschmar H, Hengerer B, Kostka M. Different Species of α-Synuclein Oligomers Induce Calcium Influx and Seeding. *The Journal of Neuroscience* 2007, 27:9220-9232.

57. Jiang P, Gan M, Yen S-H, Moussaud S, McLean PJ, Dickson DW. Proaggregant nuclear factor(s) trigger rapid formation of α-synuclein aggregates in apoptotic neurons. *Acta neuropathologica* 2016, 132:77-91.

58. Hasegawa T, Matsuzaki M, Takeda A, Kikuchi A, Akita H, Perry G, Smith MA, Itoyama Y. Accelerated α-synuclein aggregation after differentiation of SH-SY5Y neuroblastoma cells. *Brain Research* 2004, 1013:51-59.

59. Ostrerova-Golts N, Petrucelli L, Hardy J, Lee JM, Farer M, Wolozin B. The A53T α-Synuclein Mutation Increases Iron-Dependent Aggregation and Toxicity. *The Journal of Neuroscience* 2000, 20:6048-6054.

60. Dettmer U, Newman AJ, Luth ES, Bartels T, Selkoe D. In Vivo Cross-linking Reveals Principally Oligomeric Forms of α-Synuclein and β-Synuclein in Neurons and Non-neural Cells. *Journal of Biological Chemistry* 2013, 288:6371-6385.

61. Betzig E, Patterson GH, Sougrat R, Lindwasser OW, Olenych S, Bonifacino JS, Davidson MW, Lippincott-Schwartz J, Hess HF. Imaging Intracellular Fluorescent Proteins at Nanometer Resolution. *Science* 2006, 313:1642-1645.

62. Fölling J, Bossi M, Bock H, Medda R, Wurm CA, Hein B, Jakobs S, Eggeling C, Hell SW. Fluorescence nanoscopy by ground-state depletion and single-molecule return. *Nature Methods* 2008, 5:943-945.

63. Jungmann R, Steinhauer C, Scheible M, Kuzyk A, Tinnefeld P, Simmel FC. Single-Molecule Kinetics and Super-Resolution Microscopy by Fluorescence Imaging of Transient Binding on DNA Origami. *Nano Letters* 2010, 10:4756-4761.

64. Bergermann F, Alber L, Sahl SJ, Engelhardt J, Hell SW. 2000-fold parallelized dual-color STED fluorescence nanoscopy. *Optics Express* 2015, 23:211-223.

65. Douglass KM, Sieben C, Archetti A, Lambert A, Manley S. Super-resolution imaging of multiple cells by optimized flat-field epi-illumination. *Nature Photonics* 2016, 10:705-708.

66. Harke B, Keller J, Ullal CK, Westphal V, Schönle A, Hell SW. Resolution scaling in STED microscopy. *Optics Express* 2008, 16:4154-4162.

67. Caicedo JC, Cooper S, Heigwer F, Warchal S, Qiu P, Molnar C, Vasilevich AS, Barry JD, Bansal HS, Kraus O, et al. Data-analysis strategies for image-based cell profiling. *Nature Methods* 2017, 14:849-863.

68. Smith K, Li Y, Piccinini F, Csucs G, Balazs C, Bevilacqua A, Horvath P. CIDRE: an illumination-correction method for optical microscopy. *Nature Methods* 2015, 12:404-406.

69. Je G, Croop B, Basu S, Tang JL, Han KY, Kim YS. Endogenous Alpha-Synuclein Protein Analysis from Human Brain Tissues Using Single-Molecule Pull-Down Assay. *Analytical Chemistry* 2017, 89:13044-13048.

70. Scholtens TM, Schreuder F, Ligthart ST, Swennenhuis JF, Tibbe AGJ, Greve J, Terstappen LWMM. CellTracks TDI: An image cytometer for cell characterization. *Cytometry Part A* 2011, 79A:203-213.

71. Kwakwa K, Savell A, Davies T, Munro I, Parrinello S, Purbhoo MA, Dunsby C, Neil MAA, French PMW. easySTORM: a robust, lower-cost approach to localisation and TIRF microscopy. *Journal of Biophotonics* 2016, 9:948-957.

72. Deschamps J, Rowald A, Ries J. Efficient homogeneous illumination and optical sectioning for quantitative single-molecule localization microscopy. *Optics Express* 2016, 24:28080-28090.

73. Frieden BR. Lossless Conversion of a Plane Laser Wave to a Plane Wave of Uniform Irradiance. *Applied Optics* 1965, 4:1400-1403.

74. Hoffnagle JA, Jefferson CM. Design and performance of a refractive optical system that converts a Gaussian to a flattop beam. *Applied Optics* 2000, 39:5488-5499.

75. Anna M, Ulrike F. Exploring the unlimited possibilities of modular aspheric Gauss to top-hat beam shaping. *Advanced Optical Technologies* 2016, 5:201-210.

76. Edelstein A, Amodaj N, Hoover K, Vale R, Stuurman N. Computer control of microscopes using μManager. *Current protocols in molecular biology* 2010, Chapter 14:Unit14.20-Unit14.20.

77. Schneider CA, Rasband WS, Eliceiri KW. NIH Image to ImageJ: 25 years of image analysis. *Nature Methods* 2012, 9:671-675.

78. Schindelin J, Arganda-Carreras I, Frise E, Kaynig V, Longair M, Pietzsch T, Preibisch S, Rueden C, Saalfeld S, Schmid B, et al. Fiji: an open-source platform for biological-image analysis. *Nature Methods* 2012, 9:676-682.

79. Celli JP, Rizvi I, Blanden AR, Massodi I, Glidden MD, Pogue BW, Hasan T. An imaging-based platform for high-content, quantitative evaluation of therapeutic response in 3D tumour models. *Scientific Reports* 2014, 4:3751.

80. Ren J, Han KY. 2.5D Microscopy: Fast, High-Throughput Imaging via Volumetric Projection for Quantitative Subcellular Analysis. *ACS Photonics* 2021, 8:933-942.

81. Brunstein M, Teremetz M, Hérault K, Tourain C, Oheim M. Eliminating Unwanted Far-Field Excitation in Objective-Type TIRF. Part I. Identifying Sources of Nonevanescent Excitation Light. *Biophysical Journal* 2014, 106:1020-1032.

82. Mattheyses AL, Shaw K, Axelrod D. Effective elimination of laser interference fringing in fluorescence microscopy by spinning azimuthal incidence angle. *Microscopy Research and Technique* 2006, 69:642-647.

83. Fiolka R, Belyaev Y, Ewers H, Stemmer A. Even illumination in total internal reflection fluorescence microscopy using laser light. *Microsc Res Tech* 2008, 71:45-50.

84. Lin J, Hoppe AD. Uniform total internal reflection fluorescence illumination enables live cell fluorescence resonance energy transfer microscopy. *Microsc Microanal* 2013, 19:350-359.

85. Ellefsen KL, Dynes JL, Parker I. Spinning-Spot Shadowless TIRF Microscopy. *PLoS ONE* 2015, 10:e0136055.

86. Zong W, Huang X, Zhang C, Yuan T, Zhu L-l, Fan M, Chen L. Shadowless-illuminated variable-angle TIRF (siva-TIRF) microscopy for the observation of spatial-temporal dynamics in live cells. *Biomedical Optics Express* 2014, 5:1530-1540.

87. van't Hoff M, de Sars V, Oheim M. A programmable light engine for quantitative single molecule TIRF and HILO imaging. *Optics Express* 2008, 16:18495-18504.

88. Steyer JA, Almers W. Tracking Single Secretory Granules in Live Chromaffin Cells by Evanescent-Field Fluorescence Microscopy. *Biophysical Journal* 1999, 76:2262-2271.

89. Kogel A, Kalwa H, Urban N, Schaefer M. Artifact-free objective-type multicolor total internal reflection fluorescence microscopy with light-emitting diode light sources—Part I. *Journal of Biophotonics* 2019, 12:e201900033.

90. Lei M, Zumbusch A. Total-internal-reflection fluorescence microscopy with W-shaped axicon mirrors. *Opt Lett* 2010, 35:4057-4059.

91. Schreiber B, Elsayad K, Heinze KG. Axicon-based Bessel beams for flat-field illumination in total internal reflection fluorescence microscopy. *Optics Letters* 2017, 42:3880-3883.

92. Keyel PA, Watkins SC, Traub LM. Endocytic Adaptor Molecules Reveal an Endosomal Population of Clathrin by Total Internal Reflection Fluorescence Microscopy. *Journal of Biological Chemistry* 2004, 279:13190-13204.

93. Sofia SJ, Premnath V, Merrill EW. Poly(ethylene oxide) Grafted to Silicon Surfaces: Grafting Density and Protein Adsorption. *Macromolecules* 1998, 31:5059-5070.

94. Ha T, Rasnik I, Cheng W, Babcock HP, Gauss GH, Lohman TM, Chu S. Initiation and re-initiation of DNA unwinding by the Escherichia coli Rep helicase. *Nature* 2002, 419:638-641.

95. Shen L, Guo A, Zhu X. Tween surfactants: Adsorption, self-organization, and protein resistance. *Surface Science* 2011, 605:494-499.

96. Hua B, Han KY, Zhou R, Kim H, Shi X, Abeysirigunawardena SC, Jain A, Singh D, Aggarwal V, Woodson SA, et al. An improved surface passivation method for single-molecule studies. *Nature Methods* 2014, 11:1233-1236.

97. Pan J, Cha T-G, Li F, Chen H, Bragg NA, Choi JH. Visible/near-infrared subdiffraction imaging reveals the stochastic nature of DNA walkers. *Science Advances* 2017, 3:e1601600.

98. Panja S, Hua B, Zegarra D, Ha T, Woodson SA. Metals induce transient folding and activation of the twister ribozyme. *Nature Chemical Biology* 2017, 13:1109-1114.

99. Kirkness MWH, Forde NR. Single-Molecule Assay for Proteolytic Susceptibility: Force-Induced Collagen Destabilization. *Biophysical Journal* 2018, 114:570-576.

100. Loos CMvd, Göbel H. The Animal Research Kit (ARK) Can Be Used in a Multistep Double Staining Method for Human Tissue Specimens. *Journal of Histochemistry & Cytochemistry* 2000, 48:1431-1437.

101. Khaw I, Croop B, Tang J, Möhl A, Fuchs U, Han KY. Flat-field illumination for quantitative fluorescence imaging. *Optics Express* 2018, 26:15276-15288.

102. Crowther JR. *The ELISA Guidebook: Second Edition*. 2 ed. New York City: Humana Press; 2009.

103. Pleiner T, Bates M, Gorlich D. A toolbox of anti-mouse and anti-rabbit IgG secondary nanobodies. *Journal of Cell Biology* 2018, 217:1143-1154.

104. Mattson G, Conklin E, Desai S, Nielander G, Savage MD, Morgensen S. A practical approach to crosslinking. *Mol Biol Rep* 1993, 17:167-183.

105. Hermanson GT. *Bioconjugate techniques*: Academic press; 2013.

106. Sano T, Smith C, Cantor C. Immuno-PCR: very sensitive antigen detection by means of specific antibody-DNA conjugates. *Science* 1992, 258:120-122.

107. Wiener J, Kokotek D, Rosowski S, Lickert H, Meier M. Preparation of single- and double-oligonucleotide antibody conjugates and their application for protein analytics. *Scientific Reports* 2020, 10:1457.

108. Keefe AD, Pai S, Ellington A. Aptamers as therapeutics. *Nature Reviews Drug Discovery* 2010, 9:537-550.

109. Zheng Y, Qu J, Xue F, Zheng Y, Yang B, Chang Y, Yang H, Zhang J. Novel DNA Aptamers for Parkinson's Disease Treatment Inhibit α-Synuclein Aggregation and Facilitate its Degradation. *Molecular Therapy - Nucleic Acids* 2018, 11:228-242.

110. Yoshida Y, Sakai N, Masuda H, Furuichi M, Nishikawa F, Nishikawa S, Mizuno H, Waga I. Rabbit antibody detection with RNA aptamers. *Analytical Biochemistry* 2008, 375:217-222.

111. Ratz M, Testa I, Hell SW, Jakobs S. CRISPR/Cas9-mediated endogenous protein tagging for RESOLFT super-resolution microscopy of living human cells. *Scientific Reports* 2015, 5:9592.

112. Pleiner T, Bates M, Trakhanov S, Lee CT, Schliep JE, Chug H, Bohning M, Stark H, Urlaub H, Gorlich D. Nanobodies: site-specific labeling for super-resolution imaging, rapid epitope-mapping and native protein complex isolation. *Elife* 2015, 4.

113. Makaraviciute A, Jackson CD, Millner PA, Ramanaviciene A. Considerations in producing preferentially reduced half-antibody fragments. *Journal of Immunological Methods* 2016, 429:50-56.

114. Gupta J, Hoque M, Ahmad MF, Khan RH, Saleemuddin M. Acid pH promotes bispecific antibody formation by the redox procedure. *International Journal of Biological Macromolecules* 2019, 125:469-477.

115. Gupta J, Hoque M, Zaman M, Khan RH, Saleemuddin M. A detergent-based procedure for the preparation of IgG-like bispecific antibodies in high yield. *Scientific Reports* 2016, 6:39198.

116. Crumpton MJ, Parkhouse RME. Comparison of the effects of various detergents on antigen-antibody interaction. *FEBS Letters* 1972, 22:210-212.

117. Labrijn AF, Meesters JI, de Goeij BECG, van den Bremer ETJ, Neijssen J, van Kampen MD, Strumane K, Verploegen S, Kundu A, Gramer MJ, et al. Efficient generation of stable bispecific IgG1 by controlled Fab-arm exchange. *Proceedings of the National Academy of Sciences* 2013, 110:5145.

118. Ulbrich MH, Isacoff EY. Subunit counting in membrane-bound proteins. *Nature Methods* 2007, 4:319-321.

119. Wu H, Kroe-Barrett R, Singh S, Robinson AS, Roberts CJ. Competing aggregation pathways for monoclonal antibodies. *FEBS Letters* 2014, 588:936-941.

120. Porter RR. The hydrolysis of rabbit y-globulin and antibodies with crystalline papain. *The Biochemical journal* 1959, 73:119-126.

121. Ortega Arroyo J, Cole D, Kukura P. Interferometric scattering microscopy and its combination with single-molecule fluorescence imaging. *Nature Protocols* 2016, 11:617-633.

122. Huang Y-F, Zhuo G-Y, Chou C-Y, Lin C-H, Chang W, Hsieh C-L. Coherent Brightfield Microscopy Provides the Spatiotemporal Resolution To Study Early Stage Viral Infection in Live Cells. *ACS Nano* 2017, 11:2575-2585.

123. Ortega-Arroyo J, Kukura P. Interferometric scattering microscopy (iSCAT): new frontiers in ultrafast and ultrasensitive optical microscopy. *Physical Chemistry Chemical Physics* 2012, 14:15625-15636.

124. Kukura P, Ewers H, Müller C, Renn A, Helenius A, Sandoghdar V. High-speed nanoscopic tracking of the position and orientation of a single virus. *Nature methods* 2009, 6:923.

125. Piliarik M, Sandoghdar V. Direct optical sensing of single unlabelled proteins and super-resolution imaging of their binding sites. *Nature Communications* 2014, 5:4495.

126. Cole D, Young G, Weigel A, Sebesta A, Kukura P. Label-Free Single-Molecule Imaging with Numerical-Aperture-Shaped Interferometric Scattering Microscopy. *ACS Photonics* 2017, 4:211-216.

127. Young G, Hundt N, Cole D, Fineberg A, Andrecka J, Tyler A, Olerinyova A, Ansari A, Marklund EG, Collier MP, et al. Quantitative mass imaging of single biological macromolecules. *Science* 2018, 360:423-427.

128. Soltermann F, Foley EDB, Pagnoni V, Galpin M, Benesch JLP, Kukura P, Struwe WB. Quantifying Protein–Protein Interactions by Molecular Counting with Mass Photometry. *Angewandte Chemie International Edition*, n/a.

129. Breydo L, Wu JW, Uversky VN. α-Synuclein misfolding and Parkinson's disease. *Biochimica et Biophysica Acta (BBA) - Molecular Basis of Disease* 2012, 1822:261-285.

130. Uversky VN. α-Synuclein Misfolding and Neurodegenerative Diseases. *Current Protein and Peptide Science* 2008, 9:507-540.

131. Yu J, Lyubchenko YL. Early Stages for Parkinson's Development: α-Synuclein Misfolding and Aggregation. *Journal of Neuroimmune Pharmacology* 2008, 4:10.

132. Fasman GD. *Circular dichroism and the conformational analysis of biomolecules*: Springer Science & Business Media; 2013.

133. Ranjbar B, Gill P. Circular Dichroism Techniques: Biomolecular and Nanostructural Analyses- A Review. *Chemical Biology & Drug Design* 2009, 74:101-120.

134. Hassey R, Swain EJ, Hammer NI, Venkataraman D, Barnes MD. Probing the Chiroptical Response of a Single Molecule. *Science* 2006, 314:1437-1439.

135. Hoffmann A, Kane A, Nettels D, Hertzog DE, Baumgärtel P, Lengefeld J, Reichardt G, Horsley DA, Seckler R, Bakajin O, et al. Mapping protein collapse with single-molecule fluorescence and kinetic synchrotron radiation circular dichroism spectroscopy. *Proceedings of the National Academy of Sciences* 2007, 104:105-110.